UNIVERSIDADE DE SÃO PAULO
INSTITUTO DE FÍSICA DE SÃO CARLOS

NATHÁLIA BERETTA TOMAZIO

Direct laser writing of high-Q polymeric microresonators for Photonics

São Carlos
2020

NATHÁLIA BERETTA TOMAZIO

Direct laser writing of high-Q polymeric microresonators for Photonics

Thesis presented to the Graduate Program in Physics at the Instituto de Física de São Carlos, Universidade de São Paulo to obtain the degree of Doctor of Science.

Concentration area: Basic Physics

Advisor:
Prof. Dr. Cleber Renato Mendonça

Corrected Version
(Original version available on the Program Unit)

São Carlos
2020

Tomazio, Nathália Beretta
Direct laser writing of high-Q polymeric microresonators for Photonics / Nathália Beretta Tomazio; advisor Cleber Renato Mendonça - corrected version -- São Carlos 2020.
122 p.

Thesis (Doctorate - Graduate Program in Basic Physics) -- Instituto de Física de São Carlos, Universidade de São Paulo - Brasil , 2020.

1. Optical microresonators. 2. Two-photon polymerization. 3. Whispering gallery modes. 4. Rhodamine B. 5. Graphene oxide. I. Mendonça, Cleber Renato, advisor. II. Title.

In memory of my Mom, Lucineide, and my Aunt Flora,
for all their love.

ACKNOWLEDGEMENTS

I wish to express my sincere gratitude to all the people who supported me over the course of this work. It was a long run with challenges on every corner, but I was quite fortunate to have had a lot of people and institutions to ease my way through it and make it one of the most enjoyable and rewarding experiences of my life.

First of all I would like to thank my advisor and mentor Prof. Dr. Cleber Renato Mendonça for opening the door to this big scientific adventure and his constant efforts to make me achieve my goals. His dedication, passion and leadership make him a role model for my career and his invaluable lessons, which I was fortunate to get from our time spent together in a daily basis, have pushed me forward both professionally and personally. I am deeply grateful for his support, kindness and opportunities.

I also thank the professors from the Photonics Group, specially Prof. Dr. Leonardo de Boni and Prof. Dr. Lino Misoguti, for willingly sharing their knowledge, for their interest and trust in my work and for our fruitful discussions.

My sincere thanks to all the great friends I have met in the Photonics Group, from the former generation all the way to the undergrad students, including the mates from office 48 and the members of the OSA Student Chapter. All the (scientific) discussions and sharing of (failed) experiences were essential for me to get this far. Their day-to-day company has created an upbeat atmosphere and lightened the burden during difficult times.

Thanks to the Photonics Group staff, Daniel Foschini, André Romero and Marcos Cardoso, for holding everything in the lab and for their constant support.

I really appreciate the opportunity to have worked at Columbia University and University of Valencia, through the partnership with Prof. Michal Lipson and Prof. Miguel V. Andrés, respectively. It surely enriched my career by giving me the chance to extend my knowledge in microresonators and integrated photonics in general. In addition, it allowed me to set strong friendship bonds that I want to hold for life. I had

a really great time in their groups and could not thank their enough for all the support and inspiration.

I am deeply grateful to have my boyfriend Gustavo Foresto Brito de Almeida by my side. He provided the support and encouragement to help me reach my full potential and made my way through PhD brighter with his delightful company. I am proud to have such a good-hearted, hard-working and strong person as my companion.

I would like to express my profound gratitude to my parents, Antonio and Rosa Maria, for providing me with endless love, support and encouragement. I appreciate their efforts to keep me on the right track. They would do whatever is on their reach to help me accomplish my goals and have a fulfilling life.

My gratitude to The Optical Society (OSA) and The International Society for optics and photonics (SPIE) for helping me to connect with fellow scientists and leaders of my field, to keep up with my research field and to build exposure to my work.

Many thanks to the University of Sao Paulo through the Sao Carlos Institute of Physics that has held my education since 2009. Aiming high and beating obstacles have a complete new meaning to me after my long-term experience at USP. Additionally, I would like to thank all the graduation office, library, printing services office and optical and mechanical shop personnel at Sao Carlos Institute of Physics for their kind support.

I would like to gratefully acknowledge the funding agencies CAPES, CNPq, FAPESP and the U.S. Air Force for their financial support. This study was financed in part by the Coordenação de Aperfeiçoamento de Pessoal de Nível Superior - Brasil (CAPES) - Finance Code 88882.328716/2018-01.

Finally, but not least, I wish to express my deep gratitude to everybody who does not have a clear connection to this work, but made a huge difference by supporting me with genuine friendship, trust and hope.

“None of us is as smart as all of us.”

Kenneth H. Blanchard

ABSTRACT

TOMAZIO, N. B. **Direct laser writing of high-Q polymeric microresonators for Photonics**. 2020. 122 p. Thesis (Doctor in Science) - Instituto de Física de São Carlos, Universidade de São Paulo, São Carlos, 2020.

Optical microresonators have been driving considerable advances in science due to their ability to strongly confine light within small dielectric volumes and their unique features, such as frequency selectivity, high sensitivity and ease of integration into a range of photonic systems. In particular, polymers are attractive as a resonator material owing to their structural flexibility, ease of processing/functionalization and low cost. However, the fabrication of high quality factor polymeric microresonators by means of simple fabrication methodologies that afford fine tuning of the structure dimensions and its integration into different platforms/substrates is still on great demand. In this work, we demonstrated the potential of femtosecond laser writing via two-photon polymerization to fabricate high quality factor polymeric whispering gallery mode microresonators, which were doped with active compounds aiming at photonic applications. Our microresonators were fabricated from an acrylic-based photoresist. They are 50 μm diameter hollow microcylinders featuring sidewall roughness of 1.5 nm, which makes them suitable for photonic applications at visible and infrared wavelengths. They exhibit a quality factor of 1×10^5 at 1550 nm, a high performance achieved in a single step of femtosecond laser writing. In order to enable laser operation, we doped the microresonators with rhodamine B. The great power enhancement achieved within the microresonators, combined with the high fluorescence quantum yield of rhodamine B, allows for a lasing threshold as low as 12 nJ for free space picosecond excitation at 532 nm. Moreover, we investigated the mechanisms underlying a mode cleaning effect in microresonators to which we had incorporated graphene oxide. By calculating the resonances response to damping mechanisms in the microresonators, we showed that additional losses introduced by graphene oxide play a major role in reducing the visibility of a number of resonances up to the point of effectively filtering a set of modes out. Overall, this work provides a simple strategy to accomplish high quality factor polymeric microresonators and offers interesting physical insights that can be useful in the design and fabrication of photonic micro/nanodevices.

Keywords: Optical microresonators. Two-photon polymerization. Whispering gallery modes. Rhodamine B. Graphene oxide.

RESUMO

TOMAZIO, N. B. **Escrita direta a laser de micro-ressonadores poliméricos de alto fator de qualidade para Fotônica**. 2020. 122 p. Tese (Doutorado em Ciências) - Instituto de Física de São Carlos, Universidade de São Paulo, São Carlos, 2020.

Micro-ressonadores ópticos têm promovido avanços científicos notáveis devido à sua grande capacidade de confinar a luz em pequenas estruturas dielétricas e às suas singulares características, tais como seletividade de frequências, alta sensibilidade e fácil integração a um grande número de plataformas fotônicas. Em particular, polímeros são materiais atraentes para a confecção de ressonadores uma vez que oferecem flexibilidade estrutural, facilidade de processamento/funcionalização e baixo custo. Entretanto, a fabricação de micro-ressonadores poliméricos de alto fator de qualidade a partir de metodologias simples de fabricação que permitam realizar um ajuste fino das dimensões da estrutura e a sua integração a diferentes plataformas/substratos ainda representa um grande desafio. Neste trabalho, nós demonstramos o potencial da técnica de fotopolimerização por absorção de dois fótons em fabricar micro-ressonadores poliméricos de modos de galeria de alto fator de qualidade, os quais foram dopados com compostos ativos para viabilizar aplicações em Fotônica. Nossos micro-ressonadores foram fabricados a partir de uma resina de base acrílica. Eles são micro-cilindros ocos de 50 μm de diâmetro externo com rugosidade de parede lateral de 1.5 nm, o que os torna adequados para aplicações na faixa espectral de comprimentos de onda do visível e infravermelho. Eles exibem um fator de qualidade de 1×10^5 para 1550 nm, um alto desempenho atingido a partir de uma única etapa de escrita a laser. Com o intuito de viabilizar operação laser, nós dopamos os micro-ressonadores com rodamina B. A grande amplificação de potência atingida no interior dos micro-ressonadores, combinada à alta eficiência quântica de fluorescência da rodamina B, produz um limiar de ação laser de apenas 12 nJ para a excitação de espaço livre com laser de picossegundos centrado em 532 nm. Além disso, nós investigamos os mecanismos que levam a um efeito de filtragem de modos em micro-ressonadores aos quais nós incorporamos óxido de grafeno. Por meio do cálculo da resposta das ressonâncias aos mecanismos de dissipação nos micro-ressonadores, nós mostramos que as perdas adicionais introduzidas pelo

óxido de grafeno contribuem de forma mais significativa para a atenuação de um conjunto de modos. Sobretudo, esse trabalho introduz uma estratégia simples para realizar micro-ressonadores poliméricos de alto fator de qualidade e oferece soluções interessantes que podem ser úteis para o desenho e fabricação de micro/nanodispositivos fotônicos.

Palavras-chave: Micro-ressonadores ópticos. Fotopolimerização por absorção de dois fótons. Modos de galeria. Rodamina B. Óxido de grafeno.

LIST OF FIGURES

LIST OF ABBREVIATIONS AND ACRONYMS

2D	Two-dimensional
3D	Three-dimensional
2PP	Two-photon polymerization
AFM	Atomic force microscopy
CCD	Charge-coupled device
CW	Continuous wave
dB	Decibel
DoF	Depth of field
E-field	Electric field
FSR	Free spectral range
FWHM	Full width at half maximum
GM	Göppert-Mayer
GO	Graphene oxide
H-field	Magnetic field
ISC	Intersystem crossing
LED	Light-emitting diode
NA	Numerical aperture
OPA	Optical parametric oscillator
Q	Quality factor
RhB	Rhodamine B
SERS	Surface enhanced Raman spectroscopy
Taper	Tapered optical fiber
TIR	Total internal reflection
TPA	Two-photon absorption
UV	Ultra violet
Vis	Visible light
WGM	Whispering gallery mode

CONTENTS

1 INTRODUCTION

The invention of the laser by Theodore H. Maiman in 1960[1] and the breakthrough brought with the development of optical fibers in the following decades[2] paved the way for the development of Photonics as an independent research field and source of technology. Photonics, the science of generating, controlling and detecting light, has gathered a great deal of Nobel Prizes over the years[3] and has a significant impact on industry, having moved over 300 billion dollars with light-based technologies in the last years.[4] It is responsible for developing instrumentation for research laboratories and industry by exploiting applications such as optical fiber communications, material processing, data storage and imaging systems.[5]

Integrated Photonics is a branch of Photonics that comprises optical and electronic components such as lasers, modulators, electronic circuits and waveguides in a single platform of nano/micrometer dimensions.[6] It has been rapidly growing due to its potential for ultrafast data communication, high performance signal processing, sensing for the diagnostic and treatment of diseases, among other applications.[7-9] Besides, it addresses the increasingly high power consumption on chip processors, which allows switching gears towards faster, cheaper and greener broadband networks.[10] In this direction, there has been a high demand for photonic devices that combine high performance, robustness and versatility in a small footprint.

One of the most studied photonic devices is the microresonator.[11] Its ability to strongly confine light within small dielectric volumes makes it suitable for fundamental studies based on light-matter interaction and a wide variety of applications ranging from optical switches to sensors.[12-15] In this context, microresonators that support whispering gallery modes stand out due to its unique properties such as high performance, operation at optical and telecommunication wavelengths, high sensitivity and their ease of integration into a range of photonic systems.[12] Whispering gallery modes (WGMs) are wave fields that propagate along the rim of structures featuring circular geometry, e.g., spheres and cylinders, by total internal reflection.[16] The term WGM was first introduced by Lord Rayleigh in 1910 to describe the propagation of acoustic waves in the dome of St Paul's Cathedral in London.[17] Even though the phenomenon was discovered over a hundred years ago, it took until the 1990s before it began to be widely studied in the field of Optics.

The materials exploited for the fabrication of WGM microresonators are diverse and depend on both the application and the fabrication technique to be used. Silicon dioxide (SiO_2) has long been used for the fabrication of high quality factor (high-Q) WGM resonators due to its transparency to visible and telecommunication wavelengths and its surface optical quality.[18-19] SiO_2 microspheres and microtoroids can reach a quality factor over 10^8, which makes them suitable for fundamental studies requiring strong light-matter interaction such as nonlinear optics and quantum electrodynamics.[13,20-21] Crystals as resonator materials provide a few advantages over SiO_2, such as broader transparency range from ultraviolet to mid-infrared and higher nonlinearities.[22-24] Also, they may present less, or not at all, losses caused by chemical adsorption of OH^- ions and water, which is a limiting factor for the performance of silica resonators.[25-26] Ultrahigh-Q was reported for WGM microdisks of calcium fluoride (CaF_2, $Q>10^{10}$), sapphire (Al_2O_3, $Q>10^9$) and lithium tantalate ($LiTaO_3$, $Q>10^8$) fabricated by mechanical polishing techniques.[22] For large scale integration, CMOS-compatible, planar semiconductor WGM microresonators are advantageous.[27] Owing to their high refractive index, semiconductors, e.g., GaN and Silicon, support strongly confined modes that allow the resonator dimensions to be shrunk down to a few microns.[28] They are usually fabricated in a multi-step process following electron beam lithography and selective etching steps, and can achieve a range of Q-factors in the near-infrared (10^3 - 10^9).[29-31] Some examples of WGM microresonators made of different materials, and featuring different geometries, are displayed in Fig. 1.1.

Polymeric resonators have attracted increasing interest in the past two decades due to their structural flexibility, ease of processing and low cost.[28] A variety of techniques have been used to fabricate WGM polymeric microresonators, including direct lithography patterning,[32-33] molding from a master structure,[34-35] surface-tension based approach[36] and solution-printing technique.[37] Despite the efforts directed towards high quality factor polymeric resonators, there is still a great demand for simple fabrication methodologies that afford fine-tuning of the structure dimensions and its integration into different platforms/substrates. Femtosecond laser writing via two-photon polymerization (2PP) has emerged as a promising alternative to fill this gap.[38-39] The nonlinear nature of the absorptive process confers spatial confinement of the excitation, thus allowing the fabrication of 3D microstructures with flexibility of geometry and submicrometer feature size.[40] Moreover, organic dyes as

well as other active material can be directly incorporated into the polymeric matrix prior to fabrication, which can potentially broaden the range of application of WGM microresonators.[41-43]

The 2PP fabrication of microrings in an integrated photonic platform using an acrylate polymer photoresist have been reported.[38] However, such resonators exhibited modest performance ($Q<10^3$),[38] which restricts the widespread applications of WGM microresonators. Built upon these prior contributions, this work aimed to demonstrate the potential of femtosecond laser writing via two-photon polymerization to fabricate high-Q polymeric WGM microresonators. By leveraging the material flexibility of the 2PP technique, we showed that the incorporation of active compounds to the microresonator gives rise to interesting phenomena, such as low-threshold lasing and effective mode filtering (mode cleaning), which can ultimately enable the development of on-chip integrable devices in soft photonic platforms.

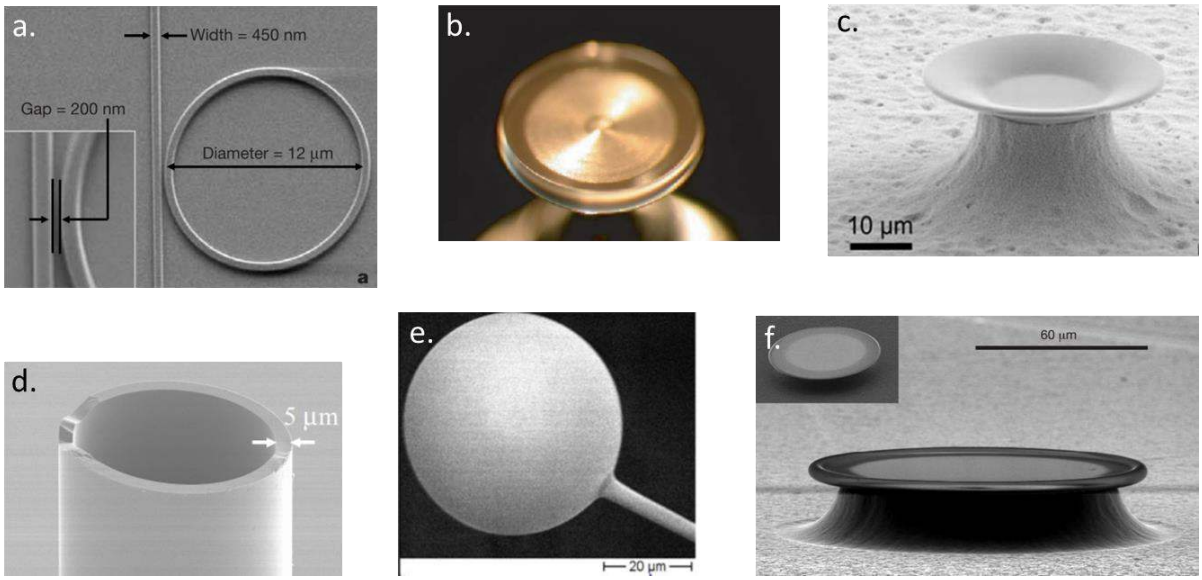

Figure 1.1 – Different types of WGM microresonators: (a) Si or Si_3N_4 microrings, (b) $LiNbO_3$ microtoroids, (c) PMMA microgoblets, (d) SiO_2 microcylinders, (e) SiO_2 microspheres and (f) SiO_2 microtoroids.
Source: Adapted from XU *et al.*[44] ILCHENKO *et al.*[24] GROSSMAN *et al.*[33] LACEY *et al.*[45] MA *et al.*[46] ARMANI *et al.*[21]

This dissertation is directed at describing the fabrication of high-Q WGM polymeric microresonators via 2PP and the mechanisms underlying (i) WGM propagation in pure polymeric microresonators, (ii) effective mode filtering (mode cleaning) in polymeric microresonators incorporated with graphene oxide (GO) and (iii) low-threshold lasing in polymeric microresonators containing rhodamine B (RhB).

To this end, the further chapters are organized as follows: Chapter 2 explores the fundamentals of WGM propagation in optical microresonators. Mode analysis, light coupling, loss mechanisms and parameters used to characterize resonators are described using a microcylinder as a model. Chapter 3 is directed at addressing the basics of microfabrication based on two-photon polymerization. Emphasis is given to subjects like spatial confinement of the excitation, sub-diffraction resolution and the role of femtosecond lasers and objective lenses to the laser writing process. In Chapter 4, the high-Q WGM polymeric microresonators are presented. The fabrication methodology and coupling setup are described in detail and the resonators structural and optical characteristics are discussed. Chapter 5 addresses the physical mechanisms behind the mode cleaning effect observed in WGM polymeric microresonators containing GO. Emphasis is given to experimental methods employed for the characterization of GO properties that play a major role in the mode cleaning. In addition, a theoretical model describing the resonances response to loss mechanisms prompted by GO is provided. Chapter 6 features the low-threshold lasing achieved in the RhB-doped WGM polymeric microresonators. This chapter encompasses the typical dye-doped structures, the experimental methods used to characterize their emission, along with a discussion on their lasing activity. Finally, Chapter 7 presents the overall conclusions and perspectives of this work.

The results presented in Chapters 4 and 6 are published in the Refs. 39[39] and 47,[47] respectively, and part of the results shown in Chapter 5 is published in Ref. 48.[48]

2 FUNDAMENTALS OF WHISPERING GALLERY MODES

This Chapter addresses the fundamentals behind both light propagation in whispering gallery mode microresonators and light coupling to them using a straight waveguide. It begins with an introduction to the history and current relevance of whispering gallery modes, followed by the theoretical basis to find the resonance frequencies of an electromagnetic field propagating within a dielectric microresonator featuring cylindrical geometry. The parameters used to characterize the microresonators, such as free spectral range, quality factor and finesse are presented. In addition, this Chapter describes how light coupling to the microresonators has been done, the transmission response of a straight waveguide coupled to a microresonator and the different coupling regimes.

2.1 History and current relevance of whispering gallery modes

The term whispering gallery mode (WGM) was introduced by Lord Rayleigh, at the beginning of the XX century, to describe an intriguing phenomenon involved in the propagation of acoustic waves along the dome of the St. Paul's cathedral, in London.[12,16-17] It was known that a person whispering close to the surface of the dome, which has 32 m of diameter, could be heard with good sound quality at any other point along the dome's perimeter if the receptor was also close to the surface (Fig. 2.1).[12] Lord Rayleigh attributed this phenomenon to the refocusing effect imposed by the curved surface of the dome over the successive grazing-angle reflections of the acoustic waves and named it whispering gallery modes.[12,49]

In the following decades, the same phenomenon was observed in the field of optics by Debye,[50] who confirmed Rayleigh's predictions and derived the equations to describe the resonance frequencies resulting from the propagation of electromagnetic waves in dielectric and metallic spheres.[16] Built upon Rayleigh and Debye works, several other scientists focused their efforts on the theoretical description of such modes. Despite the notable progress on the theory of WGMs, their potential of application in the field of optics started to be widely exploited only after the 1990s, owing to the development of more efficient and practical coupling methods.[16,49]

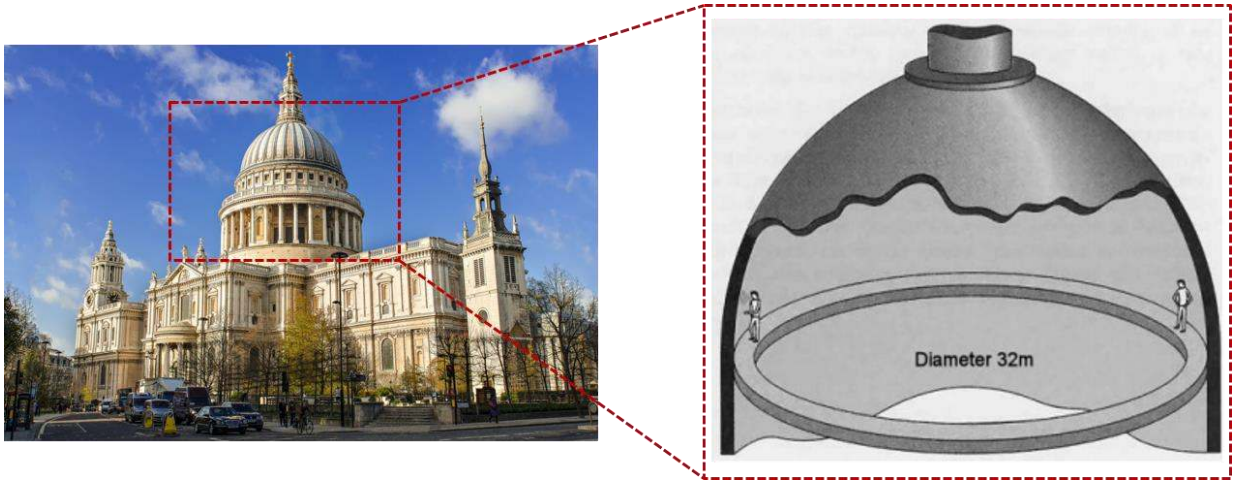

Figure 2.1 – Photograph of the St Paul's cathedral in London, UK, with a sketch of the whispering gallery in the dome.
Source: Adapted from ORAEVSKY[49]

Nowadays, the research towards the development and applications of optical WGM microresonators has been receiving enormous attention, with hundreds of publications per year reporting resonators with various geometries, ranging from the ones with simple geometry, e.g., microspheres and microcylinders,[19,51] to the ones featuring non-trivial geometry, such as microtoroids[21] and bottle-like structures.[52] Figure 2.2 shows how fast the number of publications based on WGM optical microresonators has grown over the years to become a topic of great scientific interest in the last decades.

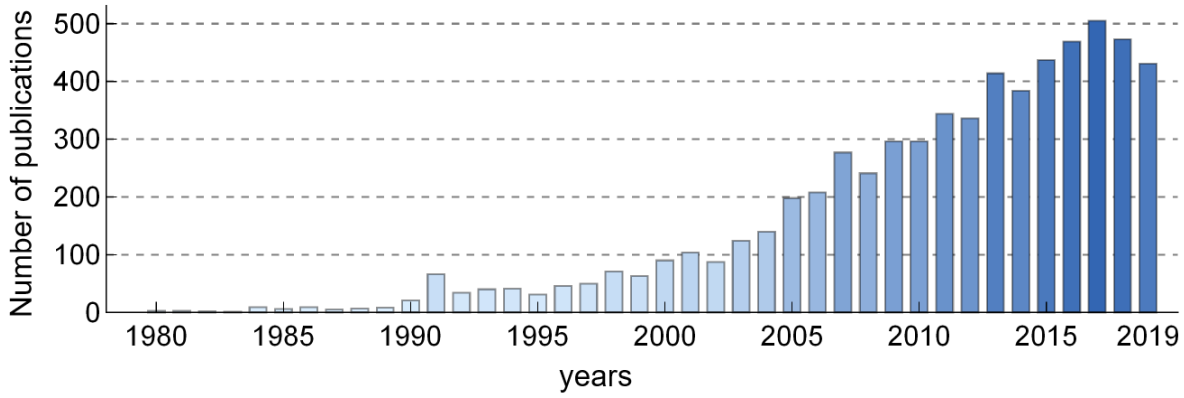

Figure 2.2 – Evolution of the number of publications reporting whispering gallery mode microresonators over the years. The histogram was obtained from data available at the Web of Knowledge collection on March 19, 2020.
Source: By the author

2.2 Fundamentals

2.2.1 Whispering gallery modes explained using geometric optics

For the sake of simplicity, we will first introduce the concept of WGMs through geometric optics. Consider that a disk made of dielectric material with refractive index n and radius a, much larger than the wavelength of light ($a \gg \lambda$), has been placed in the air ($n_{air} = 1$). The light rays propagate as shown in Fig. 2.3, forming an angle of incidence θ_i with the normal to the surface of the disk. If θ_i is larger than the critical angle, $\theta_c = sen^{-1}\left(\frac{1}{n}\right)$, the light rays experience total internal reflection (TIR) at the disk's interface with the air and are trapped inside the disk, since all the successive angles of incidence are equal owing to the disk's azimuthal symmetry.[12] The WGMs can be pictured as light rays whose optical path after a round trip in the disk results in closed-trajectories, as shown in Fig. 2.3.[12]

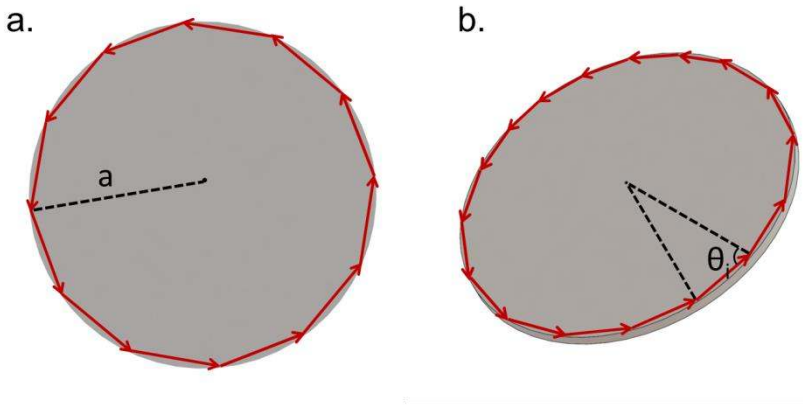

Figure 2.3 – (a) Propagation of light rays along the perimeter of a disk with radius a. (b) Angled view of the disk showing the angle of incidence θ_i formed between the light rays and the normal to the surface.

Source: TOMAZIO[53]

2.2.2 Modal analysis of a cylindrical microresonator

In this section, we will calculate the fields and the resonance frequencies for two orthogonal polarizations of an electromagnetic wave propagating along the azimuthal direction of a cylindrical structure.[51,54] The parameters used to characterize the media, along with the coordinate system, are depicted in Fig. 2.4.

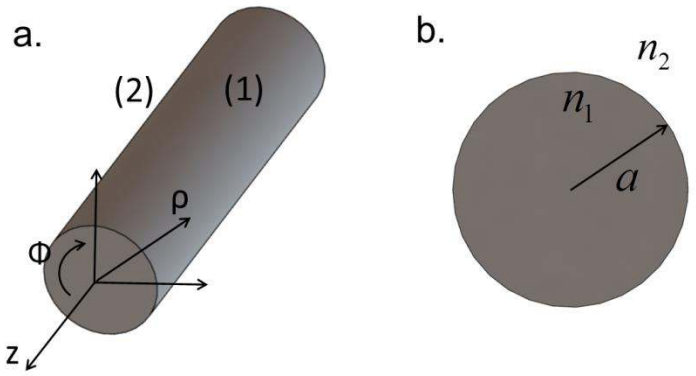

Figure 2.4 – (a) Dielectric cylinder under study in the modal analysis. The media (1) and (2) and the coordinate system are indicated in the Figure. (b) Transverse cut of the cylinder highlighting the parameters: refractive index (n_i) and cylinder's radius (a).
Source: TOMAZIO[53]

Let us consider a propagating electromagnetic wave in the azimuthal direction with harmonic time dependence, i.e., the electric (E) and magnetic (B) fields dependency on the azimuthal coordinate (ϕ) and on time (t) follows $e^{i\beta\phi - i\omega t}$, in which β is the propagation constant in the azimuthal direction and ω is the angular frequency of the electromagnetic wave.[6,54] Besides, we assume that the fields have translational symmetry along the z direction, given that the cylinder is homogeneous along z and infinitely long.[6,54-55] The expressions for the E- and H-fields are shown in Eq. 2.1.

$$\vec{E}(\rho,\phi,t) = \vec{E}_0(\rho)e^{i\beta\phi}e^{-i\omega t} = \left[\vec{E}_\perp(\rho) + \vec{E}_z(\rho)\right]e^{i\beta\phi}e^{-i\omega t}, \qquad (2.1)$$
$$\vec{H}(\rho,\phi,t) = \vec{H}_0(\rho)e^{i\beta\phi}e^{-i\omega t} = \left[\vec{H}_\perp(\rho) + \vec{H}_z(\rho)\right]e^{i\beta\phi}e^{-i\omega t}.$$

Note that the fields are expressed in terms of their transverse ($\perp$) and parallel (z) components with respect to the z coordinate.

As the WGMs propagate along the cylinder's rim, after a certain traveled path the fields reach a roundtrip in the structure. The phenomenon of resonance occurs when the fields interfere constructively after a roundtrip in the structure, i.e., the fields should match themselves after a roundtrip, except for a phase factor of 2π:[54]

$$\vec{E}(\rho,\phi) = \vec{E}_0(\rho)e^{i\beta\phi} = \vec{E}_{after\ a\ roundtrip}(\rho,\phi) = \vec{E}_0(\rho)e^{i\beta(\phi+2\pi)}. \qquad (2.2)$$
$$\therefore\ \beta = m; \qquad m = 1,2,3,\ldots$$

The condition stated in Eq. 2.2 accounts for the selectivity of the fields allowed in the structure. The fields for which β is an integer constitute the modes of the structure.[54]

There is a spectrum of modes for each polarization component of the electromagnetic field.[56] They are expressed as TM$^{(z)}$ modes when the magnetic field in the longitudinal direction is null ($H_z = 0$) and TE$^{(z)}$ modes when the electric field in the longitudinal direction is null ($E_z = 0$).[56] Here, we will determine the modes for the TM$^{(z)}$ polarization. One can proceed analogously to obtain the modes for the TE$^{(z)}$ polarization.

The transverse components of the electromagnetic fields for the TM$^{(z)}$ modes can be obtained by plugging Eq. 2.1 into Maxwell's equations. As shown in Eqs. 2.3(a-c), they are univocally determined once E_z is found.[54]

$$H_\phi = \frac{i}{\mu_0 \omega} \frac{dE_z}{d\rho}, \tag{2.3.a}$$

$$H_\rho = \frac{\beta}{\mu_0\, \omega\, \rho} E_z\,, \tag{2.3.b}$$

$$E_\phi = E_\rho = 0\,. \tag{2.3.c}$$

In the Eqs. 2.3(a-c), μ_0 is the vacuum magnetic permeability and ω is the angular frequency of the electromagnetic field.

In cylindrical coordinates, the wave equation for the E_z component is given by:[54]

$$\rho^2 \frac{\partial^2}{\partial \rho} E_z(\rho) + \rho \frac{\partial}{\partial \rho} E_z(\rho) + \left[{k_i}^2 \rho^2 - m^2\right] E_z(\rho) = 0\,, \tag{2.4}$$

for which:

$$k_i = n_i \frac{2\pi}{\lambda_0}, \quad i = 1{,}2$$

Equation 2.4 stands for a family of Bessel differential equations,[57] each one for a different value of m. The solutions of such equations for each media are represented in Eq. 2.5.[51]

$$E_z(\rho,\phi,t) = \begin{cases} a_m J_m(k_1\rho)e^{i(m\phi-\omega t)}, & \rho < a. \\ b_m H_m^{(2)}(k_2\rho)e^{i(m\phi-\omega t)}, & \rho > a. \end{cases} \quad (2.5)$$

In the Eq. 2.5, $J_m(k_i\rho)$ and $H_m^{(2)}(k_i\rho)$ are Bessel function of first kind and Hankel function of second kind, respectively, m is the azimuthal order and a_m and b_m are the field amplitude coefficients.

By plugging the solution for the E_z field component (Eq. 2.5) into Eqs. 2.3(a-c), one obtains the transverse components of the electromagnetic field:

1. Medium 1 ($\rho < a$)

$$H_\rho^{(1)} = \frac{m}{\mu_0\,\omega\,\rho} a_m J_m(k_1\rho)e^{i(m\phi-\omega t)}\,, \quad (2.6.a)$$

$$H_\phi^{(1)} = \frac{ik_1}{\mu_0\omega} a_m J_m'(k_1\rho)e^{i(m\phi-\omega t)}\,, \quad (2.6.b)$$

$$E_\rho^{(1)} = E_\phi^{(1)} = 0\,. \quad (2.6.c)$$

2. Medium 2 ($\rho > a$)

$$H_\rho^{(2)} = \frac{m}{\mu_0\,\omega\,\rho} b_m H_m^{(2)}(k_2\rho)e^{i(m\phi-\omega t)}\,, \quad (2.7.a)$$

$$H_\phi^{(2)} = \frac{ik_2}{\mu_0\omega} b_m H_m^{(2)\prime}(k_2\rho)e^{i(m\phi-\omega t)}\,, \quad (2.7.b)$$

$$E_\rho^{(2)} = E_\phi^{(2)} = 0\,. \quad (2.7.c)$$

Note that, in the Eqs. 2.6(a-c) and 2.7(a-c), the notation $' \equiv \frac{d}{d\rho}$ was used.

The boundary conditions that ensure the continuity of the tangential fields at the interface (Eq. 2.8 and Eq. 2.9) are applied to obtain the characteristic equation stated in Eq. 2.10.[54]

$$E_z^{(1)}(\rho = a) = E_z^{(2)}(\rho = a)\,, \quad (2.8)$$

$$H_\phi^{(1)}(\rho = a) = H_\phi^{(2)}(\rho = a), \quad (2.9)$$

$$\frac{1}{n_1}\frac{J_m(k_1 a)}{J_m'(k_1 a)} = \frac{1}{n_2}\frac{H_m^{(2)}(k_2 a)}{H_m^{(2)\prime}(k_2 a)}; \qquad k_i = n_i k_0 \ (i = 1,2)\,. \qquad (2.10)$$

For each azimuthal order (m), Eq. 2.10 gives a set of complex wave numbers that constitute the TM$^{(z)}$ modes of the cylinder.[51] The real part of them gives the resonant wave numbers, and their imaginary part is associated with radiation losses resulting from the cylinder's curvature.[51]

As an example, in Fig. 2.5, we show the E_z field distribution over a transverse plane of the cylinder for $m = 120$ and different radial orders ($l = 1,2,3$) obtained by plugging the roots of Eq. 2.10 into Eq. 2.5. For this analysis, we considered the parameters $n_1 = 1.51$, $n_2 = 1.0$ and $a = 22.5\ \mu m$, typical values of the microresonators to be described in the next chapters. The azimuthal order stands for the number of field amplitude maxima along the azimuthal direction, whereas the radial order represents the number of field amplitude maxima along the radial direction. The field distribution of the most fundamental radial mode (Fig. 2.5(a)) is more confined to the cylinder's surface. On the other hand, higher-order radial modes (Fig. 2.5(c-d)) have their field distribution more spread out inside the resonator, thus rendering their peak-intensity lower. The electromagnetic field trapped inside the cylinder exhibits an exponentially decaying tail extending into the surrounding medium with the decay length of a few hundred nanometers.[28,56] This feature allows light coupling in and out of the structure and is largely exploited for the development of sensors.[12,56]

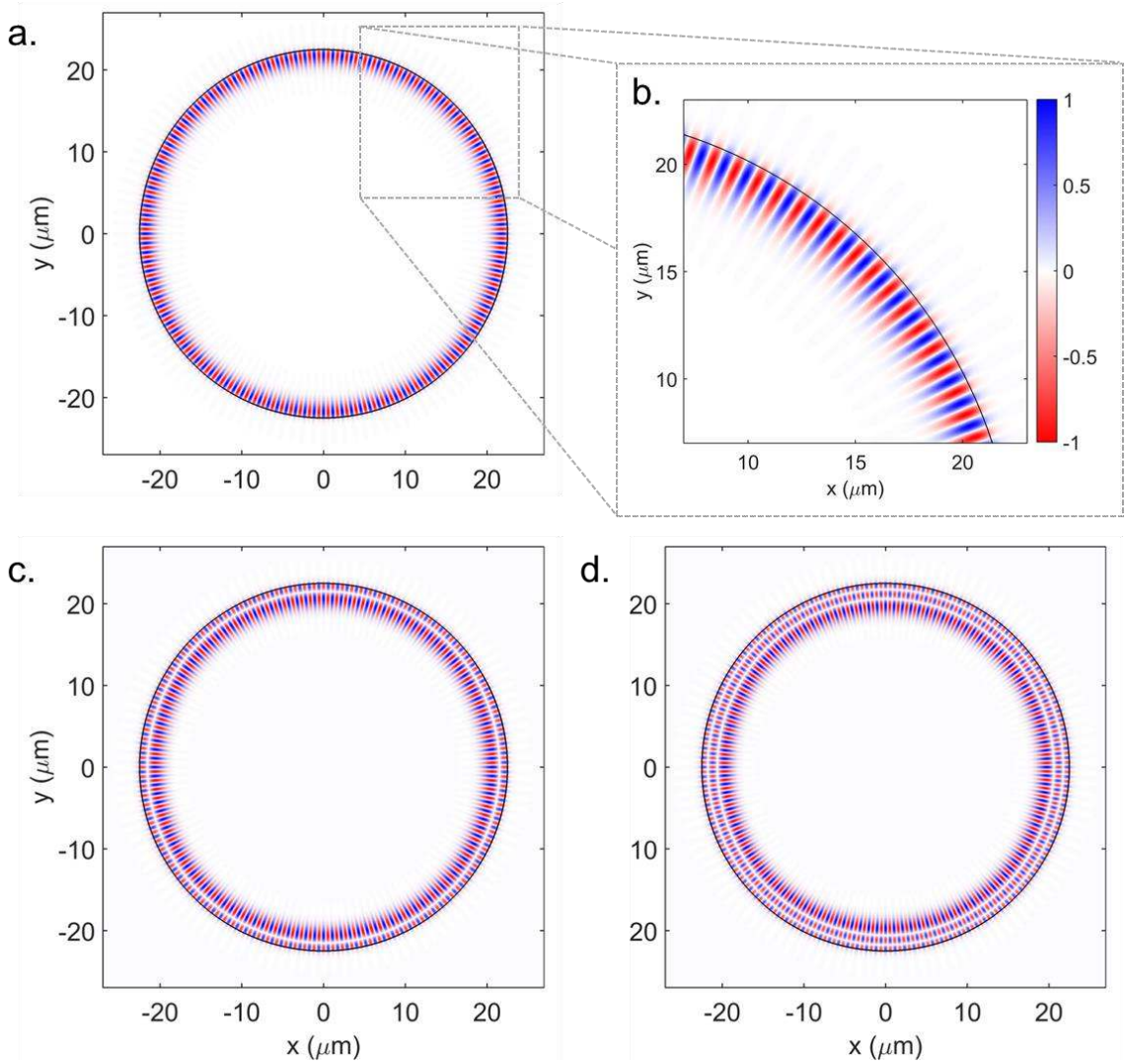

Figure 2.5 – E_z field amplitude over a transverse plane of the cylinder for the azimuthal order $\mathrm{m} = 120$ and the following radial orders: (a-b) $l = 1$ ($\lambda_{120,1}$ = 1668.2 nm), (c) $l = 2$ ($\lambda_{120,2}$ = 1579 nm) and (d) $l = 3$ ($\lambda_{120,3}$ = 1510.9 nm). Item (b) shows a zoomed view of the field distribution displayed in (a), along with the colorbar for all the field distributions. The circumference corresponds to the cylinder's edge. To obtain these field profiles, the refractive indices of both media and cylinder's radius were set to $n_1 = 1.51$, $n_2 = 1.0$ and $a = 22.5\ \mu m$ in Eq. 2.10.

Source: By the author

The total internal reflection imposes an additional constraint to the azimuthal index m.[54] As can be seen in Fig. 2.6, there are three wave vectors involved in the phenomenon of TIR: $\vec{k}^i$, $\vec{k}^r$ and $\vec{k}^t$, which denote the incident, reflected and transmitted waves, respectively.

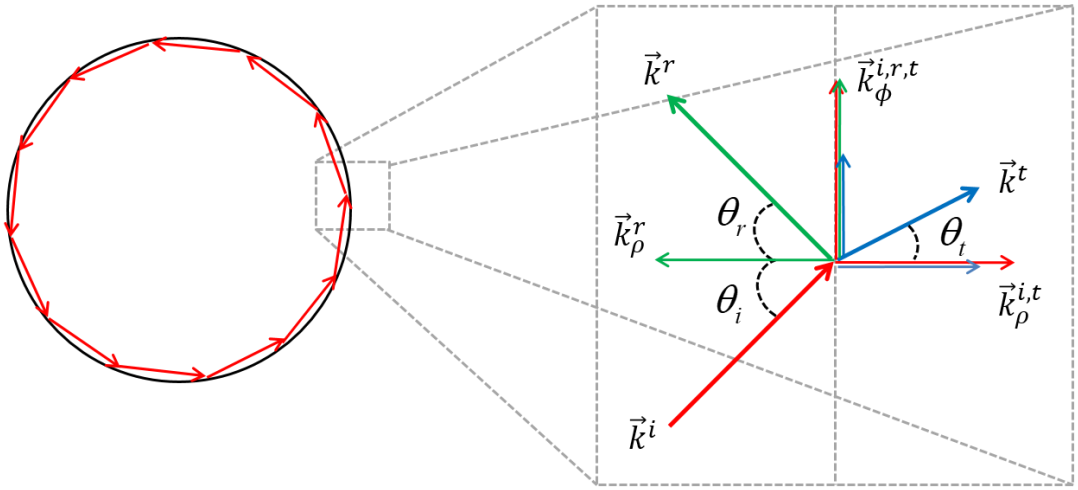

Figure 2.6 – Wave vectors involved in the phenomenon of total internal reflection, along with their projections in the azimuthal and radial directions. $\vec{k}^i$ (red), $\vec{k}^r$ (green) and $\vec{k}^t$ (blue) stand for the wave vectors of the incident, reflected and transmitted waves.
Source: Adapted from MECHÓ[54]

The WGMs are waves that propagate inside the microresonator and decay exponentially in the outside.[54] A real phase factor implies in propagating waves, whereas a pure imaginary phase factor leads to evanescently decaying waves.[54] The radial projection of the electromagnetic field inside the cylinder ($k_\rho^{i,r}$) and the azimuthal projection of the electromagnetic field in both media ($k_\phi^{i,r,t}$) are real, which translates into wave propagation for these fields.[54] Therefore, only the radial projection of the transmitted wave vector can be complex and contribute to the evanescent tail of the electromagnetic fields extending out of the cylinder. The WGM phase condition is summarized in Eq. 2.11:

$$\begin{cases} k_\rho^{i,r} = \sqrt{(k^{i,r})^2 - k_\phi^2} & \epsilon\ \mathbb{R} \\ k_\rho^t = \sqrt{(k^t)^2 - k_\phi^2} & \epsilon\ \mathbb{C} \end{cases} \rightarrow\ k^t < k_\phi < k^{i,r}\ . \qquad (2.11)$$

The incident, reflected and transmitted wave vectors can be identified as $k^{i,r} \equiv k_1$ and $k^t \equiv k_2$, where k_1 and k_2 are the wave vectors inside (medium 1) and outside the cylinder (medium 2), respectively. Using this label, the condition that restricts the interval for the azimuthal index is enunciated as:[54]

$$k_2 a < m < k_1 a \ , \quad \text{in which } \ k_i = n_i \frac{2\pi}{\lambda_0} . \tag{2.12}$$

The condition stated in Eq. 2.12 constrains the azimuthal index to be within the interval determined by the product of the wave vector in the different media by the cylinder's radius. Therefore, the WGMs are the roots of the characteristic equation (Eq. 2.10) that meet the TIR constraint.[54]

2.3 Parameters that characterize microresonators

2.3.1 Free spectral range

The free spectral range (FSR) of a WGM microresonator is frequency/wavelength spacing between consecutive azimuthal modes.[5] This parameter is commonly used to check if the peaks in the microresonator's spectrum correspond to the WGMs.

In the case of negligible material dispersion, the FSR for high-order azimuthal WGMs ($m \gg 1$) can be calculated as:[5,13]

$$FSR = \frac{\lambda^2}{2\,\pi\, a\, n_{eff}}, \tag{2.13}$$

in which, λ is the wavelength of light, and a and n_{eff} are the resonator's radius and effective refractive index, respectively.

2.3.2 Quality factor

The performance of a resonator is quantified through the quality factor (Q-factor), which is defined as the ratio between the total energy stored in the resonator and the power dissipated in one cycle of the oscillating field.[5-6]

$$Q = \omega_0 \frac{stored\ energy}{dissipated\ power}, \tag{2.14}$$

in which ω_0 is the angular frequency of the oscillating field that propagates in the resonator (resonance frequency).

The electromagnetic field in the resonator oscillates with a frequency ω_0 and decays exponentially in time with a lifetime τ. The basic equation for the time dependence of the field inside the resonator ($\vec{E}$) is given by:[6]

$$\frac{d\vec{E}}{dt} = \left[i\omega_0 - \frac{1}{\tau}\right]\vec{E}\,. \tag{2.15}$$

The total energy stored in the resonator is proportional to $\left|\vec{E}\right|^2$.[6] Power dissipation occurs due to internal losses in the resonator and coupling to the outside world. The rate at which power is dissipated is given by the rate of change in $\left|\vec{E}\right|^2$ as:[6]

$$\frac{d}{dt}\left|\vec{E}\right|^2 = -\frac{2}{\tau}\left|\vec{E}\right|^2. \tag{2.16}$$

Following the definition presented in Eq. 2.14, the Q-factor of a resonator is given by:

$$Q = \frac{\omega_0 \left|\vec{E}\right|^2}{\frac{2}{\tau}\left|\vec{E}\right|^2} = \frac{\omega_0\,\tau}{2}. \tag{2.17}$$

As it is shown in Eq. 2.17, the Q-factor is proportional to the field's lifetime inside the resonator, which is the time that it takes for the amplitude to drop by a factor of $1/e$. Therefore, the Q-factor measures the resonator's ability to confine the field in time.

We can also define the Q-factor in terms of its spectral properties. The Fourier transform of the solution of Eq. 2.15 yields:[6]

$$\vec{E} = \frac{\vec{E}_0}{i\,(\omega - \omega_0) + 1/\tau}. \tag{2.18}$$

The squared amplitude ($\left|\vec{E}\right|^2$) of Eq. 2.18 is a Lorentzian curve with full width at half maximum ($\Delta\omega$) given by:

$$\Delta\omega = \frac{2}{\tau}. \tag{2.19}$$

By plugging Eq. 2.19 into Eq. 2.17, the Q-factor can be enunciated as the ratio between the resonance frequency and its corresponding linewidth ($\Delta\omega$):

$$Q = \frac{\omega_0}{\Delta\omega}. \tag{2.20}$$

This definition of Q is largely used to characterize the time confinement of resonant systems. The Q-factor can also be expressed in terms of the resonance wavelength (λ_0) and its linewidth ($\Delta\lambda$):

$$Q = \frac{\lambda_0}{\Delta\lambda}. \tag{2.21}$$

Alternatively, the resonator's performance can be determined by its finesse, which is defined in terms of the FSR and the linewidth of its resonances according to:[5]

$$\mathcal{F} = \frac{\mathrm{FSR}}{\Delta\lambda}. \tag{2.22}$$

High-Q WGM microresonators confine light for a relatively long time, which makes it possible to achieve high circulating intensities from moderate excitation power levels, given that the effective volume of the WGMs is extremely small in these

structures.[28] Their high-Q and tight mode confinement, combined with their frequency selectivity, make such microresonators a compelling platform for fundamental studies in quantum electrodynamics and nonlinear optics and for applications ranging from optical switches in photonic circuits to biosensors.[12-15] Microresonators with Q in the range of 10^3 to 10^6 are named high-Q and those outperforming 10^7 are referred to as ultra-high-Q.[11]

The intrinsic Q-factor of WGMs is determined by several factors:[20,25]

$$Q_{in}{}^{-1} = Q_{mat}^{-1} + Q_{rad}^{-1} + Q_{surf}^{-1}\,, \tag{2.23}$$

in which, Q_{mat}^{-1}, Q_{rad}^{-1} and Q_{surf}^{-1} are the main contributions to the intrinsic Q-factor due to material, radiation and surface scattering losses, respectively.

The term Q_{mat}^{-1} refers to power dissipation through linear absorption and/or scattering at irregularities in the resonator's volume, and can be calculated by:[25]

$$Q_{mat}^{-1} = \frac{\alpha\lambda}{2\pi n}. \tag{2.24}$$

In Eq. 2.24, α is the optical attenuation coefficient and n is the refractive index of the material and λ denotes the wavelength. For example, in the case of silica microresonators ($n = 1.45$) excited at $1.55\ \mu m$ ($\alpha = 0.2\ dB/km$), Q_{mat}^{-1} is as low as $5 \cdot 10^{-11}$.[25] It is important to stress out that the value of Q_{mat}^{-1} can become considerably higher for wavelengths at which the absorption coefficient is large.

The term Q_{rad}^{-1} accounts for intrinsic radiation losses that occur due to the microresonator's curvature.[25] It decreases exponentially with the structure's dimensions,[25] i.e., the larger the ratio a/λ, in which a is the resonator's radius, the less significant are radiation losses. For instance, for a silica microsphere with a diameter of $30\ \mu m$ excited at $1.55\ \mu m$, Q_{rad}^{-1} drops to values below 10^{-11}.[20]

Q_{surf}^{-1} stands for scattering losses at irregularities present on the surface (e.g., surface roughness and contamination by adsorbed molecules). As the WGMs are tightly confined to the microresonator's surface, this is usually the dominant source of loss. To prevent surface scattering, the size of residual surface inhomogeneities must be kept orders of magnitude smaller than the excitation wavelength.[25]

Besides the aforementioned losses, power dissipation can also occur through nonlinear processes, such as multiphoton absorption[58] and self-focusing effect,[59] prompted by the high intensities achieved in WGM microresonators.

2.4 Light coupling into the microresonators

To enable the use of WGM microresonators, it is essential to have an efficient coupling scheme. There are several ways to couple light into the microresonators, most of which are based on the energy exchange between the WGMs and the evanescent field of either waveguides or other dielectric structures.[12]

One of the first coupling methods relied on the use of prisms.[20,60] In this method, a prism is positioned near the microresonator in such a way that the evanescent field of a laser beam experiencing total internal reflection (TIR) in one of its facets transfers energy to the WGMs in the microresonator. Another way to promote evanescent field-coupling is through the use of an angle-cleaved and polished optical fiber tip.[61] However, the efficiency of these methods is limited due to difficulties associated with alignment, which is required to ensure the proper overlap between the modes of the coupler element and of the microresonator. One of the most efficient ways of coupling light into WGMs is by using tapered optical fibers (tapers). It has been demonstrated that the use of tapers makes it possible to achieve a coupling efficiency above 99%.[62] The tapers are produced through heating and stretching processes that reduce the diameter of a conventional optical fiber (125 μm) to values either comparable or smaller than the wavelength of light to be guided through the structure.[63] In such cases, TIR ensures the guiding of light through the taper, but most of the power is being transmitted by the evanescent field around it, which enables the excitation of WGMs as long as both fields are properly overlapped and phase-matched.[64] Moreover, the original dimensions of the taper's edges are kept to allow the input and output of optical signals through usual systems of telecommunications. Figure 2.7 depicts the coupling methods described in this section.

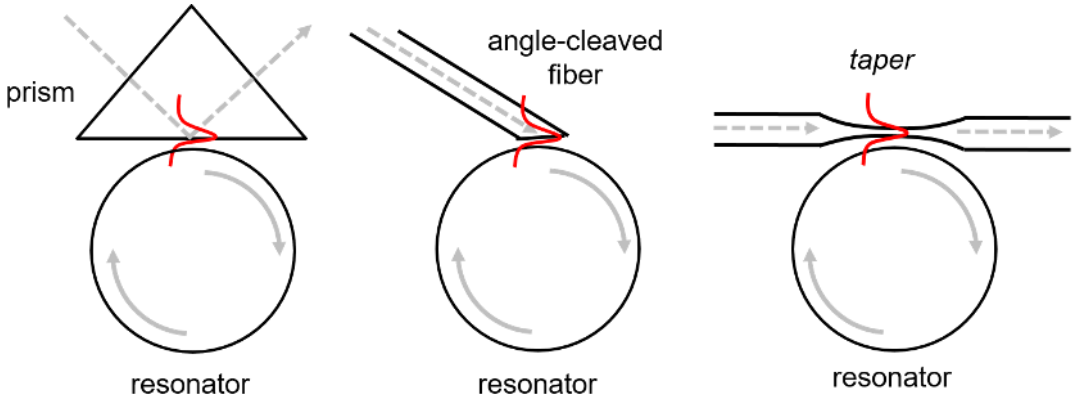

Figure 2.7 – The most common coupling schemes used to transfer optical power to WGM microresonators.
Source: Adapted from RIGHINI *et al*[12]

2.4.1 Microresonator coupled to a straight waveguide

Consider the configuration shown in Fig. 2.8 of a microresonator coupled to a straight waveguide (e.g., a taper).[6,65] Light is launched to the waveguide and is either coupled into the microresonator or transmitted. The incoming and outgoing light fields are given by $\vec{s}_{+1}$ at $z = z_A$ and $\vec{s}_{-2}$ at $z = z_B$. Here, we will assume that the waveguide is a single mode one.

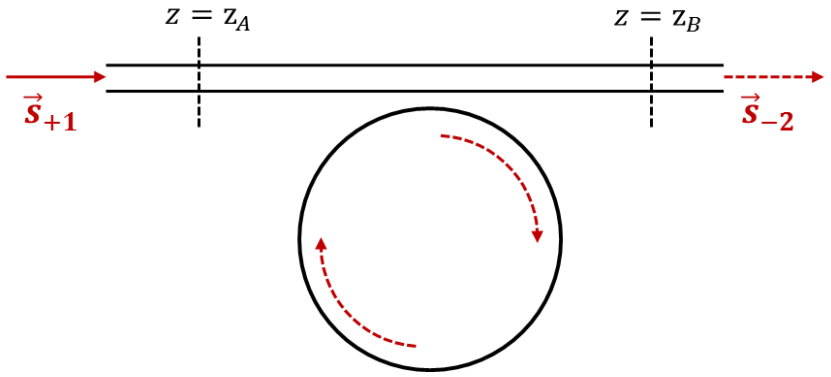

Figure 2.8 – Schematics of a straight waveguide coupled to a microresonator, in which the incoming ($\vec{s}_{+1}$) and outgoing ($\vec{s}_{-2}$) light fields are indicated.
Source: By the author

The outgoing field ($\vec{s}_{-2}$) is given by:[6]

$$\vec{s}_{-2} = e^{i\beta_w(z_B - z_A)}\left(\vec{s}_{+1} - k_1^* \vec{E}\right), \tag{2.25}$$

in which, β_w is the propagation constant of the waveguide mode, k_1^* is the coupling coefficient between the waveguide and the microresonator and the product $k_1^* \vec{E}$ represents the fraction of the field in the waveguide that is coupled into the microresonator. One can see from Eq. 2.25 that, in the absence of the resonator, the waveguide mode propagates undisturbed, achieving a phase delay of $\beta_w(z_B - z_A)$ at $z = z_B$. The coupling coefficient k_1 is calculated by the overlap integral between the waveguide mode and each excited WGM.[6,66] Therefore, it becomes higher with shrinking the gap between the waveguide and the microresonator.

The time evolution of the fields in the microresonator is given by a modified version of Eq. 2.15, which includes the coupling contribution:[6]

$$\frac{d\vec{E}}{dt} = \left[i\omega_0 - \frac{1}{\tau_0} - \frac{1}{\tau_c}\right]\vec{E} + k_1\vec{s}_{+1}\,, \tag{2.26}$$

where $1/\tau_0$ and $1/\tau_c$ are the decay rates due to internal losses in the microresonator and due to the coupling to the straight waveguide, respectively, and the product $k_1\vec{s}_{+1}$ stands for the coupling rate to the microresonator. In this case, the overall Q-factor (Q_{loaded}) is deduced from the intrinsic and coupling Q-factors values by:[12]

$$Q_{loaded}^{-1} = Q_{in}^{-1} + Q_{coup}^{-1}\,, \tag{2.27}$$

in which:

$$Q_{in} = \frac{\omega_0\tau_0}{2} \text{ and } Q_{coup} = \frac{\omega_0\tau_c}{2}\,. \tag{2.28}$$

In the frequency domain, the solution of Eq. 2.26 becomes:[6]

$$\vec{E} = \frac{k_1\vec{s}_{+1}}{i(\omega - \omega_0) + \frac{1}{\tau_0} + \frac{1}{\tau_c}}\,. \tag{2.29}$$

By plugging Eq. 2.29 into Eq. 2.25, one determines the outgoing field $\vec{s}_{-2}$ (Eq. 2.30) and the transmission coefficient in the waveguide (Eq. 2.31):[6,12,67]

$$\vec{s}_{-2} = e^{i\beta_w(z_B - z_A)}\vec{s}_{+1}\left[1 - \frac{|k_1|^2}{i(\omega - \omega_0) + \frac{1}{\tau_0} + \frac{1}{\tau_c}}\right], \tag{2.30}$$

$$T = \frac{|\vec{s}_{-2}|^2}{|\vec{s}_{+1}|^2} = \frac{(\omega - \omega_0)^2 + \left(\frac{1}{\tau_0} - \frac{1}{\tau_c}\right)^2}{(\omega - \omega_0)^2 + \left(\frac{1}{\tau_0} + \frac{1}{\tau_c}\right)^2}\ . \tag{2.31}$$

In Fig. 2.9, the transmission coefficient of a waveguide coupled to a microresonator for different values of optical losses is shown. The relative values of the decay rates $1/\tau_0$ and $1/\tau_c$ determine the microresonator coupling regime as follows:[12,67-69]

- For $1/\tau_0 > 1/\tau_c$, the rate of power dissipation through internal losses exceeds the coupling rate, and the microresonator is undercoupled. In this case, the optical power inside the microresonator is lower than that transmitted in the waveguide.
- For $1/\tau_0 = 1/\tau_c$, the rate of power dissipation through internal losses is equal to the coupling rate. In this case, the microresonator is critically coupled, meaning that all the optical power from the waveguide is transferred to it.
- For $1/\tau_0 < 1/\tau_c$, the rate of power dissipation through internal losses is smaller than the coupling rate, and the microresonator is overcoupled. In this case, the optical power inside the microresonator is higher than that transmitted in the waveguide.
- For $1/\tau_0 \rightarrow 0$, the resonator is lossless and no light is coupled to it.

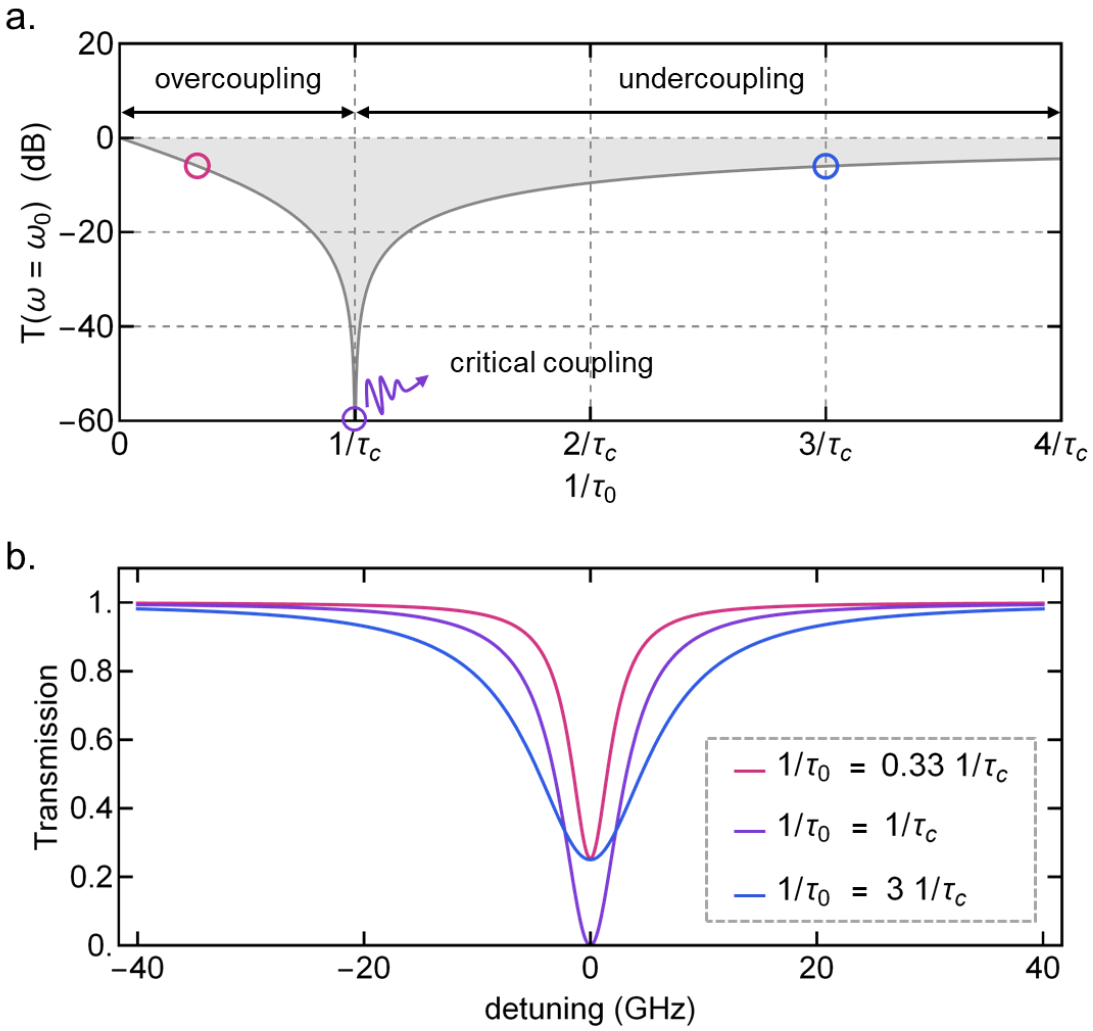

Figure 2.9 – (a) Transmission in the straight waveguide (Eq. 2.31) at a microresonator's resonance ($\omega = \omega_0$) as a function of the rate of power dissipation through internal losses in the microresonator ($1/\tau_0$). The x-axis tick labels are given in units of the coupling rate ($1/\tau_c$). The different coupling regimes are indicated in the figure. (b) Transmission in the waveguide as a function of frequency detuning ($\omega - \omega_0$) for three different levels of power dissipation through internal losses: $1/\tau_0 = 0.33\ 1/\tau_c$ (overcoupling), $1/\tau_0 = 1/\tau_c$ (critical coupling) and $1/\tau_0 = 3\ 1/\tau_c$ (undercoupling). The coupling rate is fixed at $1/\tau_c$ = 10 GHz.

Source: By the author

3 FUNDAMENTALS OF MICROFABRICATION BASED ON TWO-PHOTON POLYMERIZATION

This Chapter covers the fundamentals underlying the process of femtosecond laser writing via two-photon polymerization, which is the technique used for the fabrication of high-performance WGM polymeric microresonators presented herein. It is directed at addressing subjects relevant to microfabrication based on two-photon polymerization, including spatial confinement of the excitation, sub-diffraction resolution and the role of femtosecond lasers and objective lenses to the laser writing process.

3.1 Two-photon absorption

The phenomenon of two-photon absorption (TPA) was theoretically predicted by Maria Göppert-Mayer in her doctoral thesis in 1931.[70] On the basis of quantum mechanics, Göppert-Mayer calculated the probability of promoting an electronic transition by the simultaneous absorption of two photons. Nevertheless, this probability was found to be very low for the phenomenon to be observed with the light sources available at the time. In 1961, Kaiser e Garrett reported the detection of a fluorescence signal emitted by a $CaF_2:Eu^{+2}$ crystal under TPA excitation.[71] This was the first experimental evidence of TPA, observed thirty years that followed its theoretical description owing to the invention of lasers. The development of pulsed Ti:sapphire lasers in the 1980s catapulted the field of multiphoton processes.[72] Since then, it has been extensively studied due to its wide variety of technological applications, such as high-resolution fluorescence spectroscopy and microfabrication, and its importance for basic research.[73] For example, TPA processes can provide insights on the molecular geometry and electronic charge distribution of an excited molecule state and make it possible to measure properties of some electronic states inaccessible with traditional spectroscopy.[73]

To illustrate how unlikely the probability of TPA is under conventional light exposure, let us take as example the rhodamine B molecule, which can undergo electronic transitions via one and multiphoton absorption.[74] In bright sunlight, this molecule absorbs a photon through an one-photon process about once a second.[74]

Under the same exposure conditions, it absorbs a pair of photons via TPA every 10 million years.[74] However, if a loosely focused femtosecond laser (1 GW/cm^2) is employed as the excitation source, rhodamine B absorbs a pair of photons via TPA every 6 microseconds, which is much closer to the reach of laboratory measurement setups.

Multiphoton absorption refers to a nonlinear process where an electronic transition is induced by the collective action of two or more photons.[58,75] For the effect to occur, the energy sum of the involved photons must be resonant with the energy gap of the transition.[58] In particular, in the process of TPA, two-photons are absorbed to drive a transition between two energy levels.[76] When these photons have the same energy, as illustrated in Fig. 3.1(b), the process of TPA is said to be degenerated.[73] TPA may also occur for photons with different energies as long as the sum of their individual energies matches the energy gap.[73]

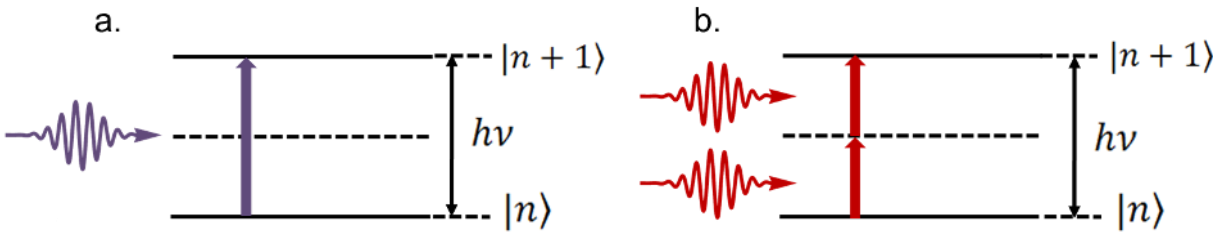

Figure 3.1 – Energy diagram representing (a) the linear and (b) the two-photon absorption.
Source: TOMAZIO[53]

The process of TPA is described by admitting the existence of a virtual state, which represents an intermediate state that mediates the otherwise forbidden transition.[77] The transition to a real state is only possible if the delay between the photons involved in the process is shorter than the virtual state lifetime (τ_v).[77] As τ_v is extremely short, on the order of femtoseconds,[76] it is usual to describe the TPA as the “simultaneous” absorption of two photons.

TPA is an optical phenomenon linked to the imaginary part of the third-order nonlinear susceptibility.[75] It may occur when the electromagnetic field interacting with a given material has a magnitude comparable to the interatomic field ($E_{int} \approx 10^{11}\ V \cdot m^{-1}$).[75] In this regime, the contribution of higher-order susceptibility terms becomes relevant, thus triggering a nonlinear response of the material charge distribution to

the applied field.[75] In the presence of strong electromagnetic fields, the absorption coefficient becomes dependent on the pump intensity according to:[73,75]

$$\alpha(I) = \alpha_0 + \beta I. \tag{3.1}$$

In Eq. 3.1, α_0 and β are the linear absorption and TPA coefficient, respectively, and I is the light intensity. β is directly associated with the TPA cross-section (σ_{2P}) as stated in Eq. 3.2:[73,75]

$$\beta = \frac{N\sigma_{2P}}{h\nu}, \tag{3.2}$$

in which, N, h and ν are the concentration of entities, the Planck constant and the pump frequency, respectively. The TPA cross-section (σ_{2P}) of most molecules is on the order of $10^{-50} cm^4 \cdot s \cdot photon^{-1}$ or 1 GM, the unit being a reference to the Nobel-laureate physicist Maria Göppert-Mayer.[58,78]

As light propagates through the material, its intensity is attenuated according to the Beer-Lambert equation.[76] For wavelengths out the linear absorption spectrum of the material ($\alpha_0 = 0$), the rate at which light is attenuated along propagation follows Eq. 3.3:[73,76]

$$\frac{dI(z)}{dz} = -\beta I^2(z)\,. \tag{3.3}$$

As shown in Eq. 3.3, the attenuation rate prompted by TPA depends on the pump intensity squared. This nonlinear dependence, combined with the small TPA cross-section of most materials, makes it possible to achieve spatial confinement of the excitation through the use of focused high-intensity laser beams, e.g. femtosecond pulses delivered by a mode-locked Ti:sapphire oscillator.[73] A comparison between the degree of attenuation induced by one and two-photon absorption is provided in Fig. 3.2. In the linear absorption case, the beam intensity is exponentially attenuated as it penetrates the medium, whereas in the TPA case the attenuation is confined within the focal volume of the beam. The nonlinear nature of TPA makes it attractive for a wide range of applications, such as three-dimensional

optical data storage,[79-80] photodynamic therapy,[81] microscopy[82-83] and microfabrication.[84-85]

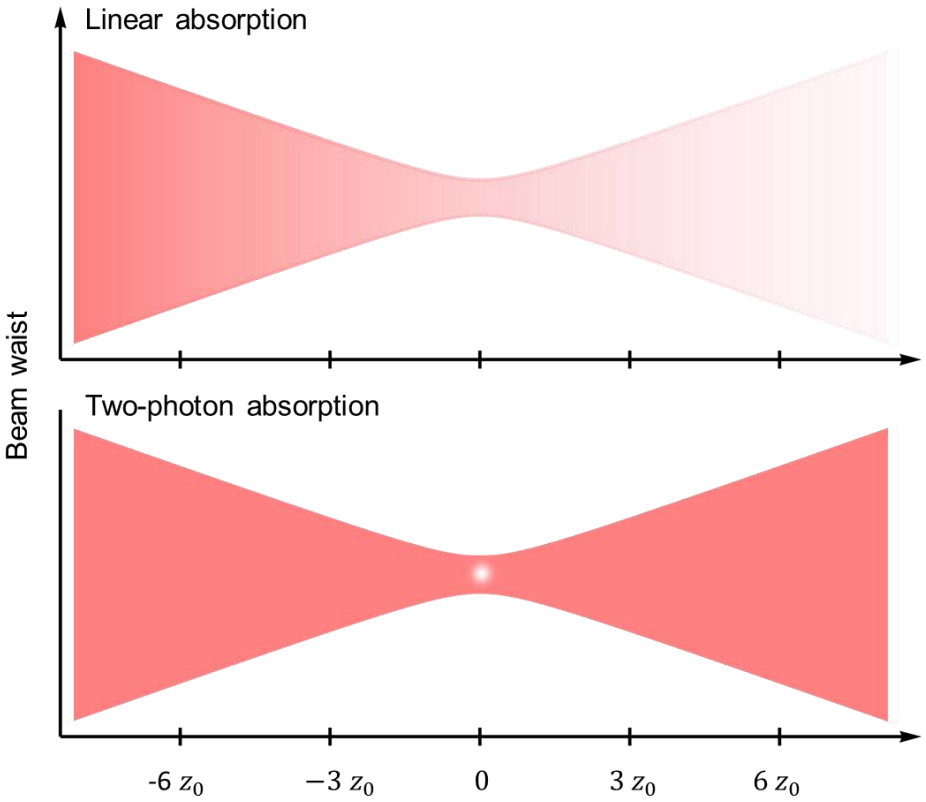

Figure 3.2 – Differences in the attenuation produced by one (above) and two-photon (below) absorption in a focused Gaussian laser beam. X-axis is given in units of the confocal parameter denoted by z_0.
Source: By the author

3.2 Two-photon polymerization

The photoresist used for two-photon polymerization (2PP) has two crucial components: the monomers and the photoinitiator.[58,86] The former are molecules of low molecular weight whereas the latter is the photo-sensitive compound responsible for driving the chain reaction that results in the cross-linked polymer. The success of polymerization depends strongly on the choice of the photoinitiator, for which characteristics such as high TPA cross-section and polymerization rate and broad solubility are desirable.[58]

The radical polymerization stands out among the different types of polymerization reactions used for TPA-based fabrication due to its ease of processing, high reaction rates and wide availability of monomers and photoinitiators

for this type of chemistry.[58] It comprises three main steps of radical generation, initiation and propagation,[58,87] as illustrated in Fig. 3.3. First, the interaction of the photoinitiator molecules with light gives rise to free radicals, which react with the monomers by breaking their unsaturated bonds and creating reactive species. In the propagation step, such reactive species bind to monomers, increasing the size of the molecular chain. Each added monomer leads to a new reactive species that reacts with other monomers, causing the chain to grow. Eventually, the reactive species containing over hundreds of monomers are suppressed by reacting with other large reactive species, giving rise to a highly cross-linked polymeric blend.

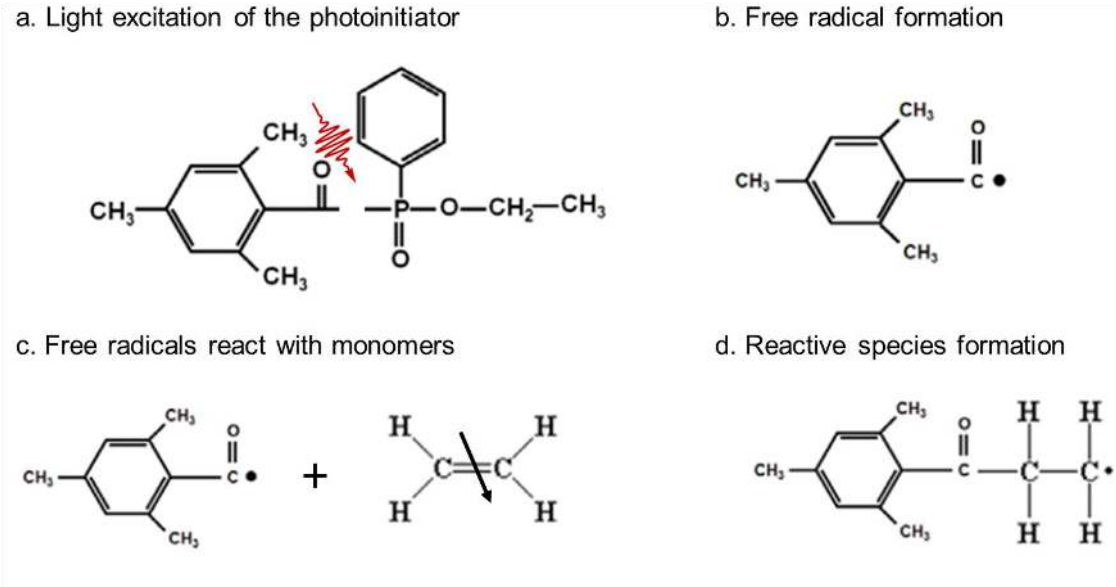

Figure 3.3 – Main steps of the photo-induced radical polymerization exemplified with the molecules of ethene (C_2H_4) and the photoinitiator ethyl-2,4,6-trimethylbenzoyl phenyl phosphinate.
Source: Adapted from GOMES[87]

The nonlinear nature of TPA makes it possible to restrict the radical formation and subsequent polymerization to the focus volume of a laser beam, which translates into spatial resolution to nano/microdevice fabrication.[58] Moreover, the quadratic dependence of TPA on the pump intensity pushes the resolution down by a factor of $\sqrt{2}$, thus allowing the fabrication of sub-diffraction features.[88] TPA-based fabrication can achieve even higher resolution through quenching processes that set up an intensity threshold below which radical polymerization cannot be sustained to create a solid structure.[87,89] Polymerization suppression at low-intensity levels is largely caused by the presence of molecular oxygen.[89] Oxygen molecules react with the free

radicals formed by the photo-driven breakdown of the photoinitiator, reducing the polymerization rate significantly. Though this polymerization threshold may be detrimental for some applications, it is advantageous for TPA-based fabrication since it allows reducing the polymerized feature size even further by employing peak intensity levels slightly above the threshold. Commercial 2PP-based setups can fabricate structures with feature size as small as 200 nm[90] and 2PP-based setups of research laboratories can achieve a lateral resolution below 100 nm.[88,91-94]

3.3 Femtosecond laser writing via two-photon polymerization

Femtosecond laser writing via two-photon polymerization (2PP) has proven to be a powerful tool for high-precision 3D microfabrication of organic and hybrid materials due to its unique set of advantages, such as the fabrication of sub-diffraction features and 3D structuring of arbitrary shapes.[39,95-96] Moreover, its material versatility makes it possible to tailor the microstructures' physical, chemical or biological properties by either changing the composition of the photoresist or adding extra functionality through the incorporation, via doping or coating processes, of a large variety of materials.[73] For example, polymer hardness and the amount of shrinkage the material undergoes upon polymerization can be controlled by changing the proportion of the monomers in the photoresist. Other examples of the technique's material versatility would be the introduction of optically induced and erased birefringence in polymeric microstructures doped with azopolymers[97] or the fabrication of drug delivery-microneedles featuring low infection risk owing to the incorporation of an antimicrobial compound.[98]

In this technique, a high-intensity pulsed laser is tightly focused to the volume of the photoresist by using an objective lens.[58] The pump wavelength is set out of the linear absorption spectrum of the photoinitiator to constrain polymerization to TPA and leverage its nonlinear nature to ensure spatial confinement of the excitation. The focused beam gives rise to a polymerized volume with sub-micrometer dimensions (voxel).[58] By scanning the laser beam over the photoresist, the voxels are overlapped to create arbitrary high complexity three-dimensional nano/microstructures, including those containing movable parts.[96,99-100] Examples of microstructures that can be accomplished with femtosecond laser writing via 2PP are shown in Fig. 3.4.

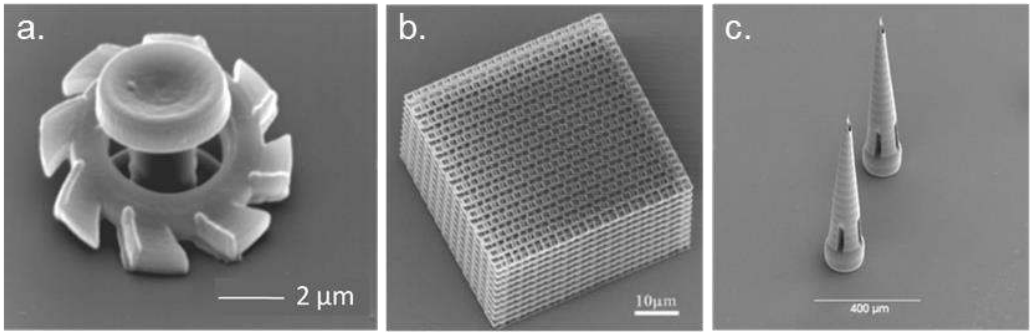

Figure 3.4 – Scanning electron micrographs of functional microstructures fabricated by femtosecond laser writing via two-photon polymerization. (a) Micro-gears, (b) photonic crystal and (c) micro neddles for controlled drug delivery.
Source: Adapted from MARUO; IKUTA; KOROGI[99] SEET *et al.*[96] OSTENDORF; CHICHKOV[100]

3D microfabrication techniques based on 2PP require high peak intensities, on the order of 100 GW/cm^2, which can be readily accomplished by femtosecond lasers. One of the most popular laser systems used for 2PP-based 3D microfabrication is the mode-locked Ti:sapphire oscillator.[101-104] Its active medium is a titanium-doped sapphire crystal, which is usually pumped by a green CW laser, such as the frequency-doubled solid-state lasers based on neodymium-doped gain media.[102] The broad gain bandwidth of titanium ions (Ti^{3+}) combined with the mode-locking mechanism allows producing pulses with time duration on the order of femtoseconds.[101,103] For example, the Ti:sapphire laser system used to fabricate the polymeric microstructures presented in this work delivers infrared (790 nm) femtosecond pulses at 86 MHz of repetition rate. Their time duration can reach 20 fs for transform-limited pulses and the output average power can exceed 400 mW. Such pulses carry around 4.5 nJ of energy and 0.2 MW of peak power and, when focused to a 1 µm-waist beam, can achieve a peak intensity of 60 TW/cm^2, which is much higher than which is required to enable 2PP microfabrication. Interestingly, this power level (0.2 MW) is only three orders of magnitude lower than that produced by a turbine of the World's largest hydroelectric power stations, such as Brazil and Paraguay's Itaipu or China's Three Gorges.

Objective lenses play a crucial role in determining the voxel characteristics since they define the intensity spatial profile around the focal volume.[58] Their focusing power can be inferred from their numerical aperture (NA), which reflects their ability to gather light.[105] The higher the lens NA, the greater is their focusing power. The NA of an objective lens can be calculated using Abbe's equation:[105-106]

$$NA = n\, sen(\theta). \tag{3.4}$$

In Eq. 3.4, n is the refractive index of the medium between the lens and the object, and θ is one-half of the lens angular aperture. The radius of a gaussian beam at the focal plane (w_0) depends on the objective lens NA according to:[73]

$$w_0 = \frac{\lambda}{\pi\, NA}\sqrt{n^2 - NA^2}\,, \tag{3.5}$$

in which λ is the wavelength of light, n is the refractive index of the medium between the lens and the object and NA is the objective lens's numerical aperture. From Eq. 3.5, one can see that the higher the lens NA, the higher is the resolution in the transverse plane of the object (lateral resolution).

Another important parameter of objective lenses is their axial resolution, which is usually referred to as depth of field (DoF). It stands for the distance interval between the lens and the object within it the object can be translated without getting out of focus. For gaussian beams, the DoF corresponds to the double of the confocal parameter:[106-107]

$$DoF = 2z_0 = \frac{2\pi\, w_0^2}{\lambda}. \tag{3.6}$$

In the Eq. 3.6, z_0 is the axial distance from the smallest beam waist ($z = 0$) at which the beam waist increases by a factor of $\sqrt{2}$. As opposed to the focusing power, the DoF is shorter for high NA objective lenses.

The voxel dimensions and shape are determined by the intensity distribution around the focal volume constrained by the optical and chemical nonlinearities of the 2PP-based microfabrication.[58] Thus, the voxel exhibits an elliptical shape with transversal and longitudinal dimensions that can be smaller than the objective lens lateral resolution ($2\, w_0$) and DoF ($2z_0$), respectively. As it is illustrated in Fig. 3.5, higher NA objective lenses (NA ≥ 0.65) feature great focusing power and short DoF, thus producing smaller rounded voxels that are required for high-resolution microfabrication. On the other hand, lower NA objective lenses produce more elongated voxels that allow obtaining smooth surfaces more easily in microstructures

featuring straightforward geometries. The sidewalls of microstructures fabricated with lower NA objective lenses feature higher surface smoothness than that obtained with its high NA counterpart for the same degree of voxel overlap.

The voxel can become bigger depending on the intensity level and exposure time of the laser writing process.[58] Higher intensity levels increase the volume for which TPA is significant, which translates into bigger voxels. Longer exposure times also increase the voxel size by allowing the photoinitiator molecules to diffuse in the photoresist and, consequently, to extend the cross-linking reaction to a bigger volume. Other factors such as the photoinitiator concentration and its radical quantum yield, the photoresist viscosity and the concentration of any polymerization quencher can play a role in the ultimate voxel dimensions.[58]

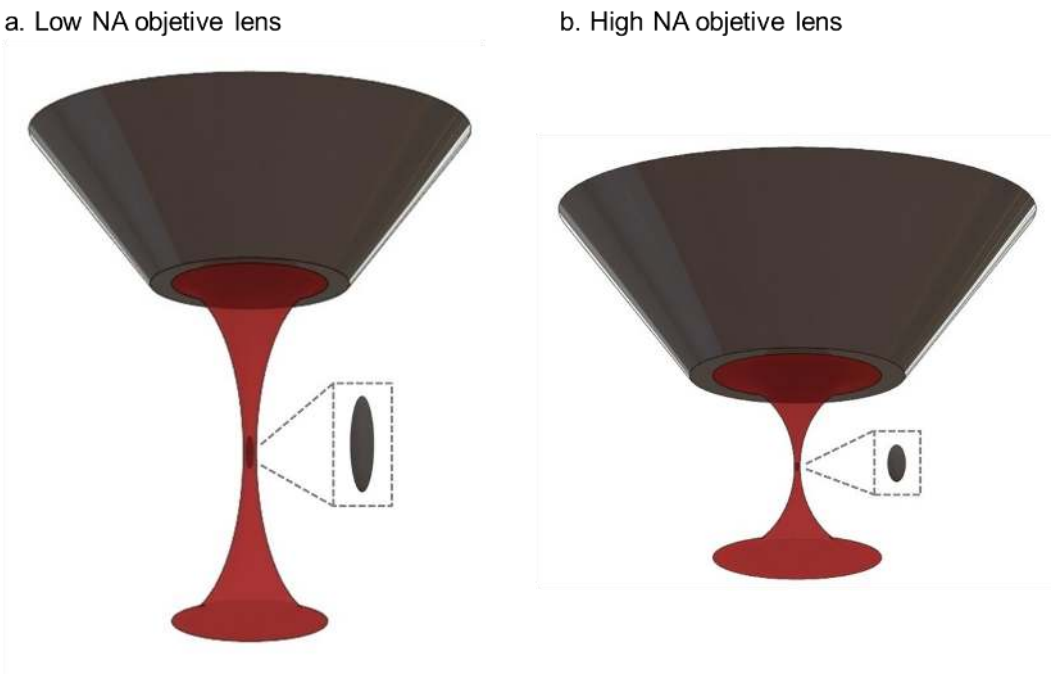

Figure 3.5 – Comparison between voxels produced by (a) low (e.g., 0.25 NA) and (b) high numerical aperture (e.g., 0.85 NA) objective lenses.
Source: Adapted from TOMAZIO[53]

4 FEMTOSECOND LASER WRITING OF HIGH-Q POLYMERIC WHISPERING GALLERY MODE MICRORESONATORS†

This Chapter is directed at describing the fabrication methodology, the setup used to couple light to the microresonators and the typical high-Q polymeric WGM microresonators. The resonators are fabricated by femtosecond laser writing via two-photon polymerization using an acrylic-based photoresist. They are interrogated by a coupling setup based on the evanescent field through the use of tapered optical fibers. The microstructures morphological and optical properties were characterized by scanning electron and atomic force microscopies and by near-infrared spectroscopy, respectively.

4.1 Femtosecond laser writing via two-photon polymerization

4.1.1 Photoresist preparation

The microstructures are fabricated using a negative-tone photoresist composed of two acrylate monomers and a photoinitiator. The monomers tris (2-hydroxy ethyl) isocyanurate tryacrylate (SR368 - Sartomer®) and ethoxylated (6) trimethylolpropane triacrylate (SR499 - Sartomer®) are mixed in a proportion of 70/30 wt%. To reach to these optimal proportions, we prepared photoresists with different compositions by varying the proportion of the monomer SR499 in increments of 10 wt% and evaluated the overall quality of the fabricated microstructures by scanning electron microscopy. The aromatic ring of the SR368 confers rigidity to the final polymer while the long straight chains of the SR499 reduce the shrinkage intrinsic to the polymerization reaction.[108] Although the SR368 brings hardness to the structures, it can make them brittle if added in excess to the photoresist. Therefore, the SR499 is added, in a smaller proportion, to ensure flexibility to the microstructures while avoiding shrinkage upon polymerization.

As photoinitiator we chose the ethyl-2,4,6-trimethylbenzoyl phenyl phosphinate, commercially known as Lucirin TPO-L (in excess of 3 wt%, Irgarcure®). When excited via TPA, the Lucirin TPO-L molecule undergoes breakdown of the

† The results presented in this Chapter are published in Ref. 39.[39]

carbon-phosphorus bond, which produces highly reactive radicals.[108-109] This favorable property of Lucirin TPO-L counteracts its low TPA cross-section at the wavelength delivered by the Ti:sapphire pump laser (on the order of 0.1 GM), thus leading to an efficient polymerization even for a few milliwatts of average power.[110] Besides, Lucirin TPO-L is liquid at room temperature and has a broad solubility, which allows it to be readily mixed into most photoresist formulations.[108] The molecular structure of the monomers and the photoinitiator is shown in Fig. 4.1.

a. SR499 ethoxylated (6) trimethylolpropane triacrylate

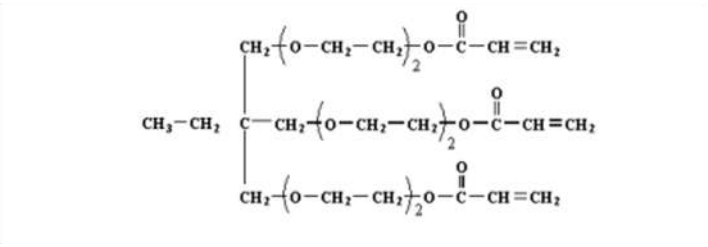

b. SR368 tris (2-hydroxy ethyl) isocyanurate tryacrylate

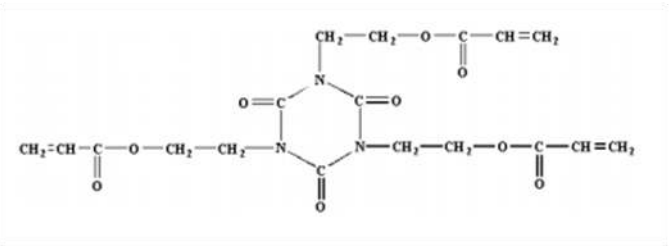

c. Lucirin TPO-L ethyl-2,4,6-trimethylbenzoyl phenyl phosphinate

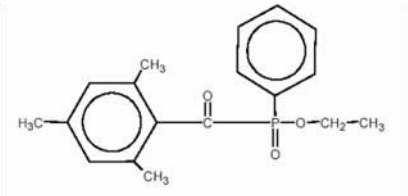

Figure 4.1 – Molecular structure of the acrylic-based monomers (a) SR499 and (b) SR368 and (c) the photoinitiator Lucirin TPO-L.
Source: By the author

The monomers and photoinitiator are put together and steered for 30 min in the dark. After a thorough mixing of its compounds, a drop of the photoresist is sandwiched between a glass substrate and a cover slip separated from each other with a 125 µm spacer. The sample is placed on a translation stage mounted on an inverted microscope in the microfabrication setup.

4.1.2 Microfabrication methodology

A schematic of the setup for femtosecond laser writing via 2PP developed in our laboratory is shown in Fig. 4.2. As excitation source we use a mode-locked Ti:sapphire oscillator (KMLabs Collegiate®) that delivers 100 fs pulses centered at 790 nm, with a repetition rate of 86 MHz. A CW Nd:YVO_4 laser (532 nm) delivering 4.5 W of power is used to pump the Ti:sapphire crystal. Further information on ultrashort pulse generation by mode-locking mechanisms can be found elsewhere.[102,104,111]

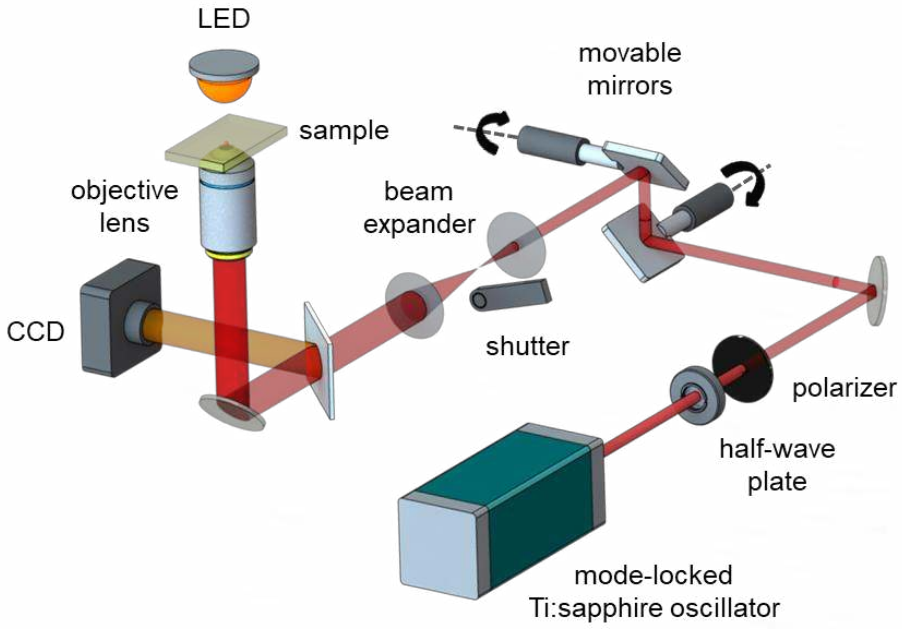

Figure 4.2 – Experimental setup for the microfabrication via femtosecond laser-induced two-photon polymerization built at the Photonics Group (IFSC-USP).
Source: Adapted from TOMAZIO[53]

The laser beam is focused into the photoresist using an objective lens. A beam expander is used to match the objective lens entrance aperture. A pair of movable mirrors scans the laser transversally in the photoresist. Their amplitude of rotation is limited by the objective lens entrance aperture, which restricts the dimensions of the microstructure. For example, microstructures with dimensions up to 200 µm can be fabricated using a 0.25 NA objective lens. A motorized stage with a step resolution of around 0.5 µm is used to move the sample in the vertical direction, in parallel to the objective lens optical axis. The laser exposure is controlled with the

aid of a mechanical shutter inserted at the focus of the beam expander system and its intensity is adjusted with a half-wave plate and a polarizer. An imaging system is used for real-time diagnostics and troubleshooting of misalignment and misadjusted parameters. It comprises a red LED, a beam splitter and a camera in a transmission microscope scheme. In the camera, the refractive index contrast between the photoresist and the polymerized features allows visualizing the laser writing process. The LED emission is set out of the linear absorption spectrum of the photoinitiator to prevent one-photon induced polymerization.

The coordinated action of the movable mirrors, translation stage and shutter is controlled with a computer-aided software. The laser writing process follows a layer-by-layer approach. Each layer is polymerized according to a vectorization algorithm that provides a set of coordinate points arranged as a pattern of concentric lines, which can be run either from inside out or otherwise (Fig. 4.3(a)). The density of points (d) and exposure time of the laser beam (Δt) defines the laser scan speed according to:

$$v_{scan} = \frac{1}{d\,\Delta t}. \tag{4.1}$$

The density of points, the spacing between concentric lines and the vertical displacement of the stage determine the degree of voxel overlap in the transversal and vertical directions, as depicted in Fig. 4.3(a). The voxel overlap achieved throughout the laser writing process gives rise to the polymerized layers that constitute the final microstructure. To achieve microstructures with great surface optical quality, the voxels must be properly overlapped, as indicated in Fig. 4.3(b). A poor degree of voxel overlap results in microstructures featuring high surface roughness that hold the individual characteristics of the voxels (Fig. 4.3(c)).

To hold the microstructures to the substrate, at the beginning of the laser writing process, the focus of the objective lens should be placed at the substrate surface or somewhat inside it. This way, the first polymerized layer will be adjacent to the substrate. After the fabrication is finished, the unsolidified photoresist is removed by rinsing the sample with ethanol at 60°C for 20 min, leaving only the microstructures on top of the glass substrate.

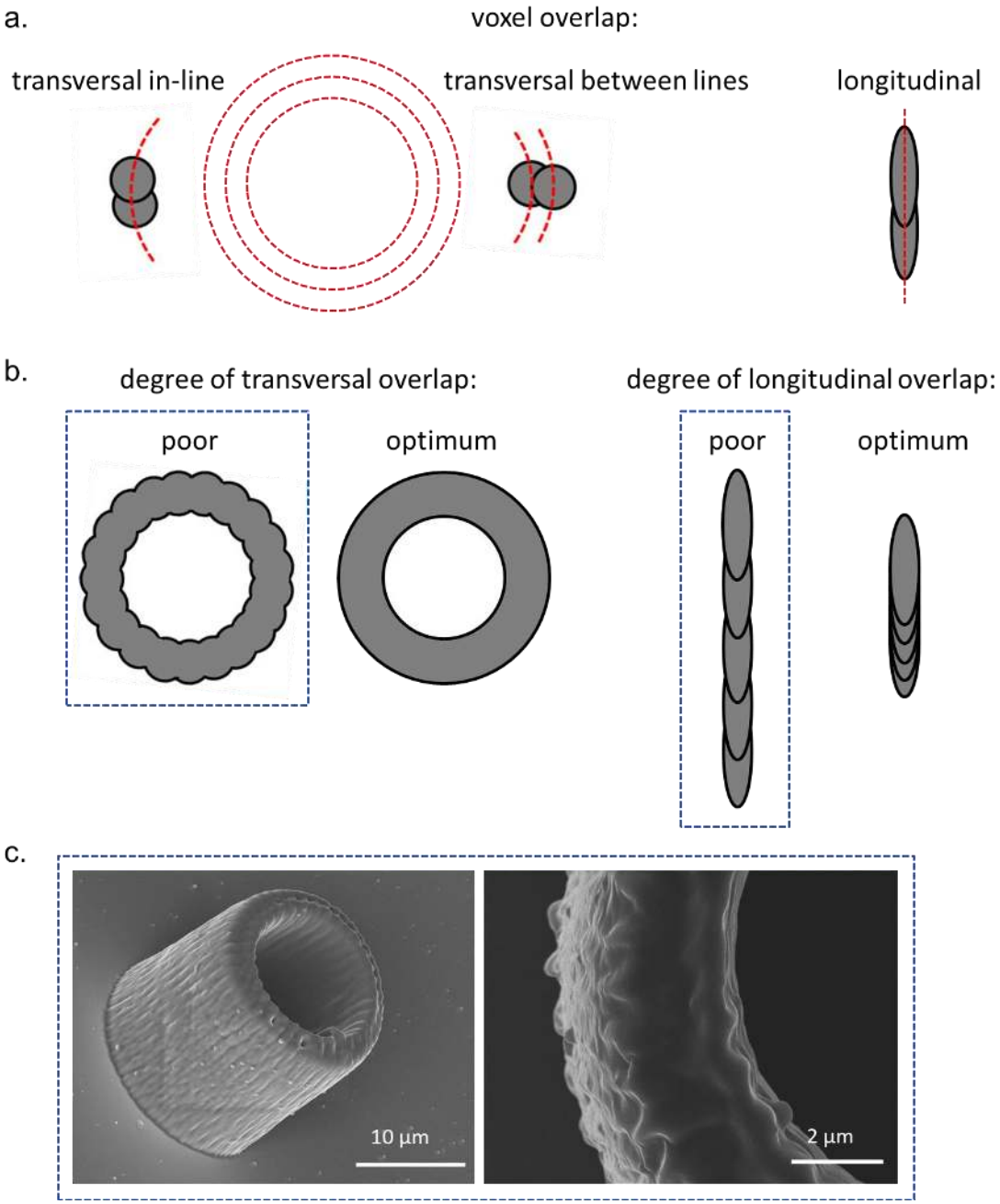

Figure 4.3 – (a) Different types of voxel overlap. In the transverse direction, the density of points and the spacing between vectorization lines determine the degree of voxel overlap intra- and interline, respectively. The z-step of the motorized stage defines the degree of voxel overlap in the longitudinal direction. (b) Comparison between a poor and an optimum degree of voxel overlap. (c) Example of microstructure fabricated with a poor degree of voxel overlap.

Source: By the author

4.1.3 Typical microstructures

Figure 4.4(a) shows a typical resonator fabricated by two-photon polymerization employing 0.1 nJ pulses (measured at the sample) from a Ti:sapphire

oscillator with 40 µm/s of laser scan speed (exposure time = 5 ms and density of points = 5 μm^{-1}). The fabricated hollow microcylinders exhibit an outer diameter of 55 µm, 3.9 µm of sidewall thickness and approximately 60 µm of height. They feature good structural integrity and smooth sidewall surface. The structural quality is a direct result of the appropriate proportion between the acrylate monomers in the photoresist; the 70/30 wt% (SR368/SR499) proportion leads to a highly cross-linked polymeric blend that does not shrink significantly nor becomes distorted after polymerization.

To be used as microresonators, the fabricated microcylinders must feature great optical quality. The required optical quality implies on spatially homogeneous polymeric volume and surface roughness much smaller than the excitation wavelength.[58] Volumetric homogeneity is ensured by stabilizing the laser output power and keeping the scanning conditions uniform throughout the microstructure fabrication. Achieving optically smooth surfaces, on the other hand, is considerably challenging. For such a task, as opposed to previous works,[38,112-113] we employed a 0.25 NA objective lens (w_0 = 1 µm, z_0 = 4 µm). Due to its greater depth of field in comparison to its counterparts, the 0.25 NA objective lens produces a more elongated polymerized volume (voxel), which exhibits transverse and longitudinal dimensions of 1 µm and 10 µm, respectively, for 40 um/s of laser scan speed and 0.1 nJ of pulse energy. Some strategies to measure the voxel dimensions are presented in Refs. 58 and 114.[58,114] Each layer that comprises the microcylinder was vectorized as a pattern of concentric circumferences 0.5 µm apart from each other. The layer height was adjusted to 1.5 µm. Both parameters, the distance between the circumferences and the layer height, were set to achieve a vertical and transversal (interline) voxel overlap of 85% and 50%, respectively. The density of points was set to 5 μm^{-1}, resulting in a degree of voxel overlap of 90% along the vectorization lines.

The surface quality of the microresonators was obtained by directly measuring their outer sidewall roughness using atomic force microscopy (Nanosurf FlexAFM). In Fig. 4.4(b), an AFM micrograph taken on the sidewall surface of a typical microcylinder is presented. As the sidewall thickness of such microresonators is larger compared to the excitation wavelength, the WGMs do not overlap with the inner sidewall surface, which has not been taken into account on this analysis. From the AFM results we obtained an arithmetic average of the *roughness* (Ra) of 1.5 nm for the microstructures outer sidewall surface, which is considerably smaller than

wavelengths typically used in telecommunication, thus making the microcylinders promising candidates as resonators in the near-infrared regime.

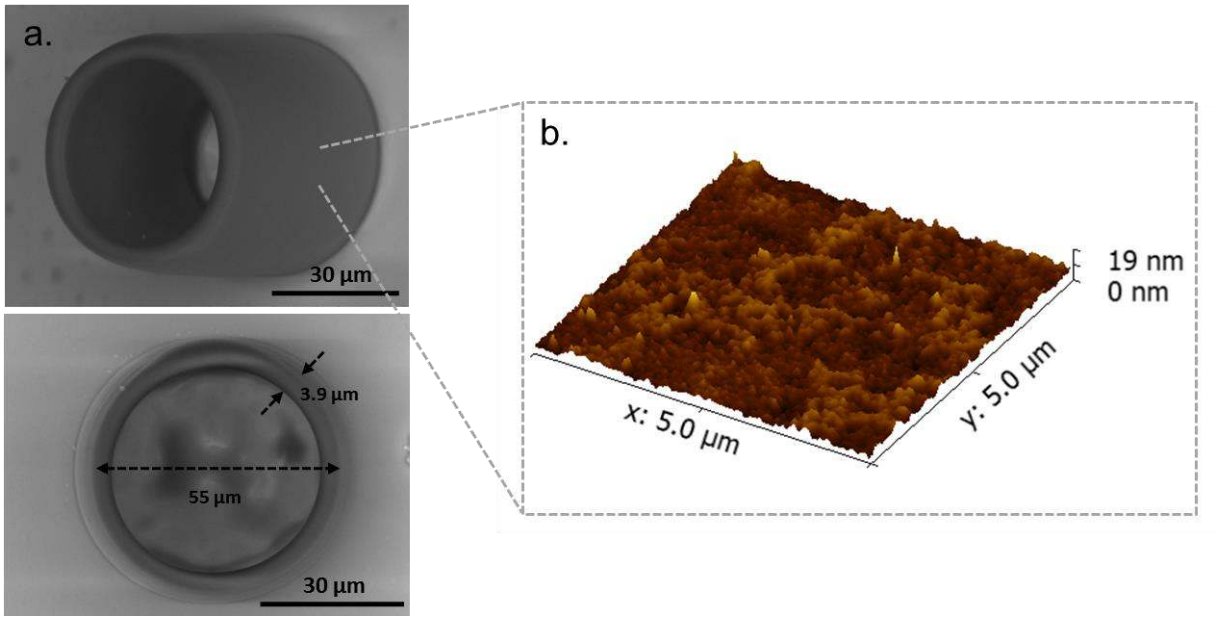

Figure 4.4 – (a) Scanning electron micrographs of a typical microcylinder produced by femtosecond laser writing via two-photon polymerization. (b) Atomic force microscopy of the microcylinder outer sidewall surface.
Source: TOMAZIO *et al*[89]

4.2 Light coupling into the microresonators

4.2.1 Coupling methodology

The microresonator modes were characterized by a coupling setup based on the evanescent field from a tapered optical fiber (Fig. 4.5). In this setup, we used an external-cavity tunable laser (SANTEC – TSL-510 / type A) as the excitation source. Its tuning range varies from 1510 nm to 1630 nm, with a minimum wavelength step of 5 pm. The polarization state of light is adjusted by using manual fiber polarization controllers, which create independent wave plates via stress-induced birefringence produced by wrapping the fiber around the spools. Light at certain frequencies is coupled into the microresonator using a 1.5 µm-waist diameter tapered fiber. To properly align the taper and the microresonator, the former is placed in a 3-axis translational stage while the latter is attached to a goniometer placed on a fixed platform. Their positioning is monitored with the aid of a stereomicroscope and a CCD camera. The transmitted light is measured with an InGaAs photodiode

connected to a computer-aided software, which remotely controls the laser tuning and acquires the photodiode signal along the spectrum. The WGMs are identified as attenuation peaks in the transmission spectrum.

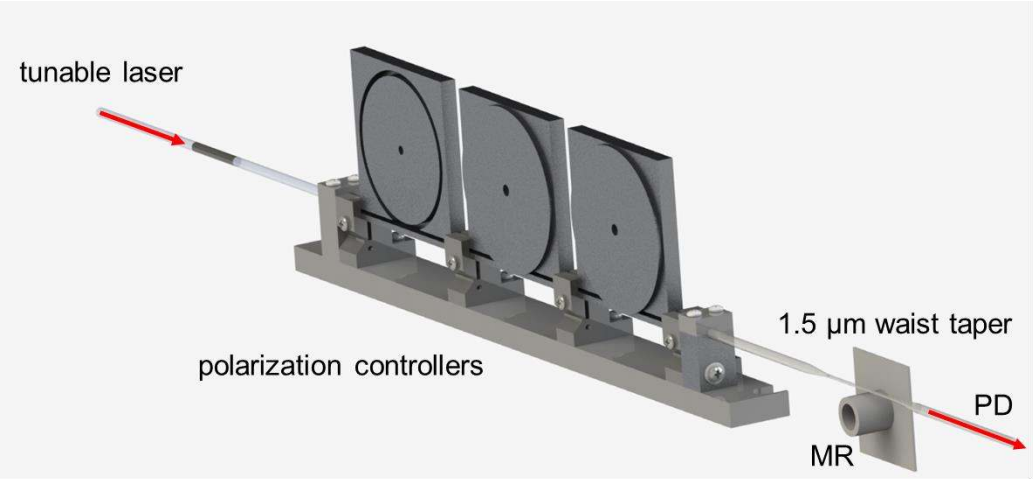

Figure 4.5 – Main components of the setup used to couple light to the polymeric WGM microresonators. MR and PD denote microresonator and photodiode, respectively.
Source: By the author

4.2.2 Tapered optical fiber fabrication

A tapered optical fiber is formed by heating and stretching a section of an optical fiber until it reaches a few micrometers of diameter.[64] The outcome is a small waist section (taper) connected to the untreated ends of the fiber by adiabatic taper transitions. In the thinner part of the tapered fiber, the fiber core is no longer significant, and light propagates in the fundamental mode through the waveguide formed by the silica waist surrounded by air.[63-64] If the waist is small compared to the wavelength of light, such mode exhibits an evanescent tail extending considerably out into the free space surrounding the taper, in which most of the power is transmitted.[115] The evanescent light makes it possible to couple optical power to the microresonators by bringing the taper close to them.

The fabrication of tapers was carried out using a setup developed in our laboratory, through which fibers of arbitrary dimensions and with transmission around 80% can be produced. Although tapers with arbitrary widths can be accomplished with this setup, we usually fabricate tapers with a few microns of waist diameter (1-3 µm). In this setup, a conventional single-mode fiber is attached to movable stages coupled to a software-controlled step motor. To stretch the fiber, the stages are

simultaneously displaced with the same speed and in opposite directions. Fiber heating is performed by using a conventional blowtorch filled with butane, which provides temperatures sufficiently high to melt silica. Following the flame brush technique,[116] the blowtorch is placed on a motorized stage that oscillates with constant speed within a certain length. It heats only a small section of the fiber at a time, so that every element in the fiber length is identically heated after an oscillation cycle. A fiber-laser and a photodetector are used to monitor the optical power guided through the fiber over the stretching process. The main components of the setup, along with the fiber-taper positioning scheme, are shown in Fig. 4.6.

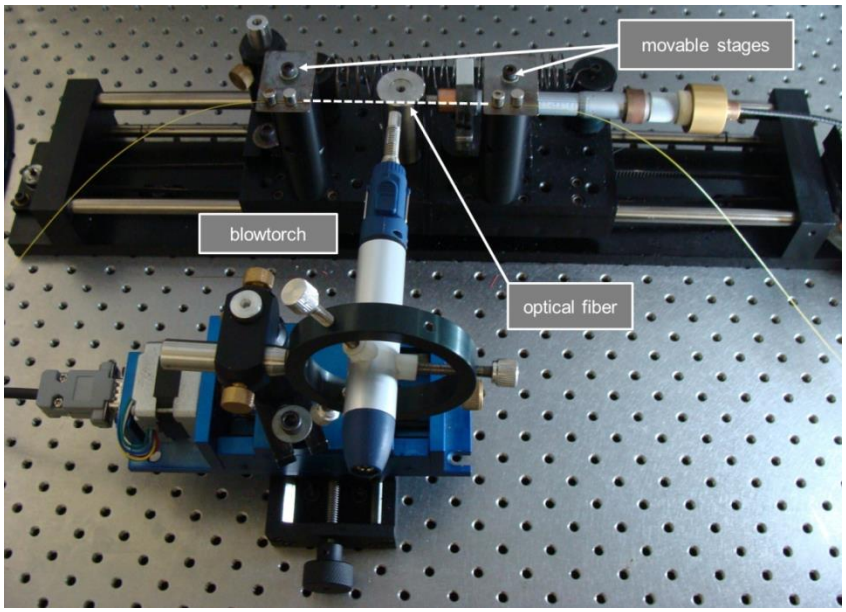

Figure 4.6 – Tapered optical fiber fabrication setup assembled in the Photonics Group (IFSC-USP).
Source: Adapted from TOMAZIO[53]

The software that controls the movable stages allows adjusting the fiber stretching length and speed. The flame oscillation length and speed can be tuned by varying the frequency of the electric signals sent to the motorized stage to which the blowtorch is attached. The length of the taper (smallest-waist section) matches the flame oscillation length (L) as pictured in Fig. 4.7. For a constant value of L, the radius of the taper (r_t) is determined by Eq. 4.2, which derives from mass conservation principles over the stretching process.[63]

$$r_t = r_0 \exp\left[-\frac{d}{2L}\right]. \qquad (4.2)$$

In Eq. 4.2, r_0 is the initial radius of the fiber, L is the flame oscillation length and d is the total length of the transition sections.

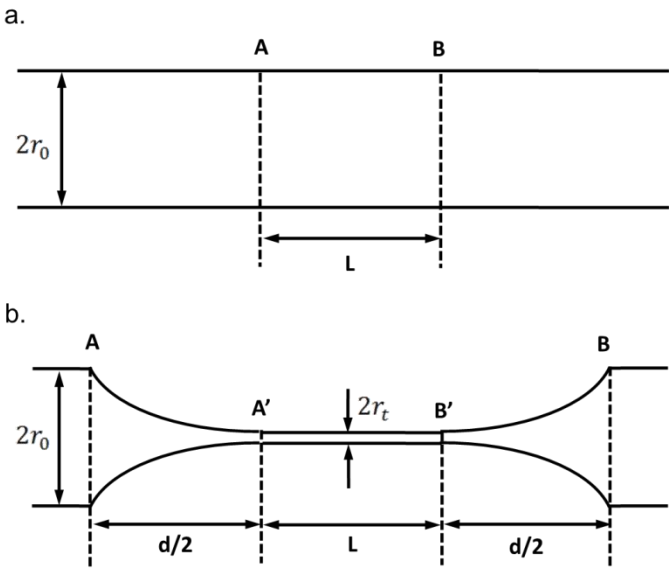

Figure 4.7 – Longitudinal cut of the optical fiber (a) before and (b) after the stretching process.
Source: TOMAZIO[53]

The stretching speed is set to 3 mm/min to produce low-loss tapers with smooth transition sections. Once the radius and length of the taper are chosen, the software uses Eq. 4.2 to match these dimensions. Since the fibers that we use to produce tapers are conventional single-mode fibers, r_0 is set to 62.5 um.

4.2.3 Microresonator modal analysis and performance

The microresonator modal analysis was performed around 1550 nm, the wavelength region of interest for telecommunications. In such spectral region the acrylate polymer exhibits a small absorbance plateau (Fig. 4.8), which sets a fundamental upper limit to the resonator quality factor. Following the description given in section 2.3, the Q-factor due to attenuation losses in the volume can be determined by using:[25]

$$Q_{mat} = \frac{2\,\pi\,n(\lambda)}{\alpha\,\lambda}, \qquad (4.3)$$

in which λ denotes the excitation wavelength, $n(\lambda)$ is the material refractive index at λ, and α is the attenuation coefficient. The attenuation coefficient and refractive index of the acrylate polymer at 1550 nm were found to be (0.32 $\pm$ 0.05) cm^{-1} and 1.510 $\pm$ 0.001, respectively, by running Fourier Transform Infrared Spectrophotometer (IRTracer-100) and refractometry (Carl Zeiss Jena Pulfrich Refractometer PR2) experiments. These measurements were performed in macroscopic samples with the same composition used to produce the microstructures. They are UV-cured freestanding disks with 1.1 mm of thickness and 2 cm of diameter made from the acrylic-based photoresist. By taking these values (α = 0.32 cm^{-1} and n = 1.51) into consideration, we obtained Q_{mat} = 1.9×10^5. This material losses contribution is certainly the main limit for the polymeric microresonator Q-factor at 1550 nm, given the low sidewall roughness and the large curvature radius of the fabricated structures compared to the excitation wavelength.

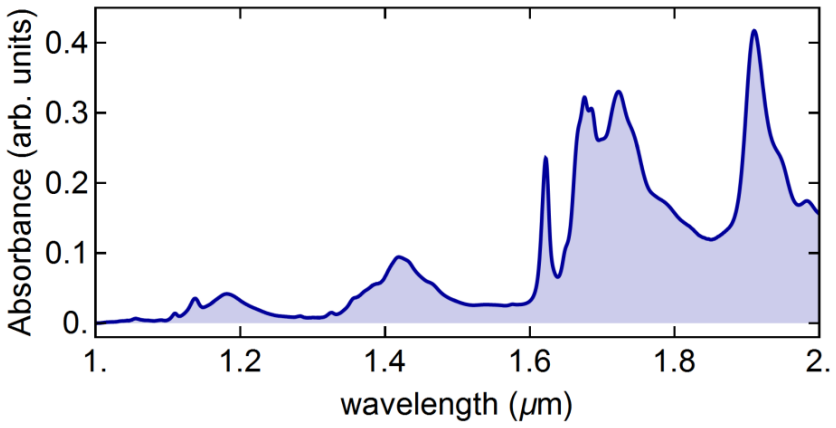

Figure 4.8 – Absorbance spectrum of a 1.6 mm-thick polymeric macroscopic sample (prepared from the photoresist composition: 30 wt% SR499, 70 wt% SR368 and 3 wt% Lucirin TPO-L) measured in the near-infrared.
Source: By the author

Shown in Fig. 4.9(a) is the transmission spectrum of a tapered fiber coupled to a polymeric microresonator. The resonances are sharp, and present an asymmetric linewidth that is either attributed to the thermo-optic effect that causes the resonances to drift or to the excitation of Fano resonances.[117-120] In order to determine the free spectral range (FSR) for the fundamental radial order TM and TE modes, we performed a numerical simulation (Matlab) following the approach described in the section 2.2.[51] Basically, Maxwell equations were solved for both TM and TE electromagnetic waves in a dielectric hollow cylinder placed in air. The

characteristic equation, that follows from applying the boundary conditions at the outer and inner interfaces of the cylinder, gives the allowed modes. By taking into consideration the microcylinder radius (a = 27.5 μm) and refractive index at 1550 nm (n = 1.51), we were able to solve the characteristic equation specifically for our microresonators. We numerically computed the TE and TM fundamental radial order modes within the range 1540 – 1560 nm (excitation window) and sought the ones that best matched the experimental peaks in terms of absolute value and free spectral range. By doing so, we found the peaks tagged in Fig. 4.9(a) to be the pairs $TE^{159,1}$, $TE^{158,1}$ and $TM^{160,1}$, $TM^{159,1}$, where the upper indexes correspond to the azimuthal and radial orders, respectively. The FSR of these TE and TM modes was calculated as 9.4 nm and 9.43 nm, which are in agreement with the experimental FSR, highlighted in Fig. 4.9(a).

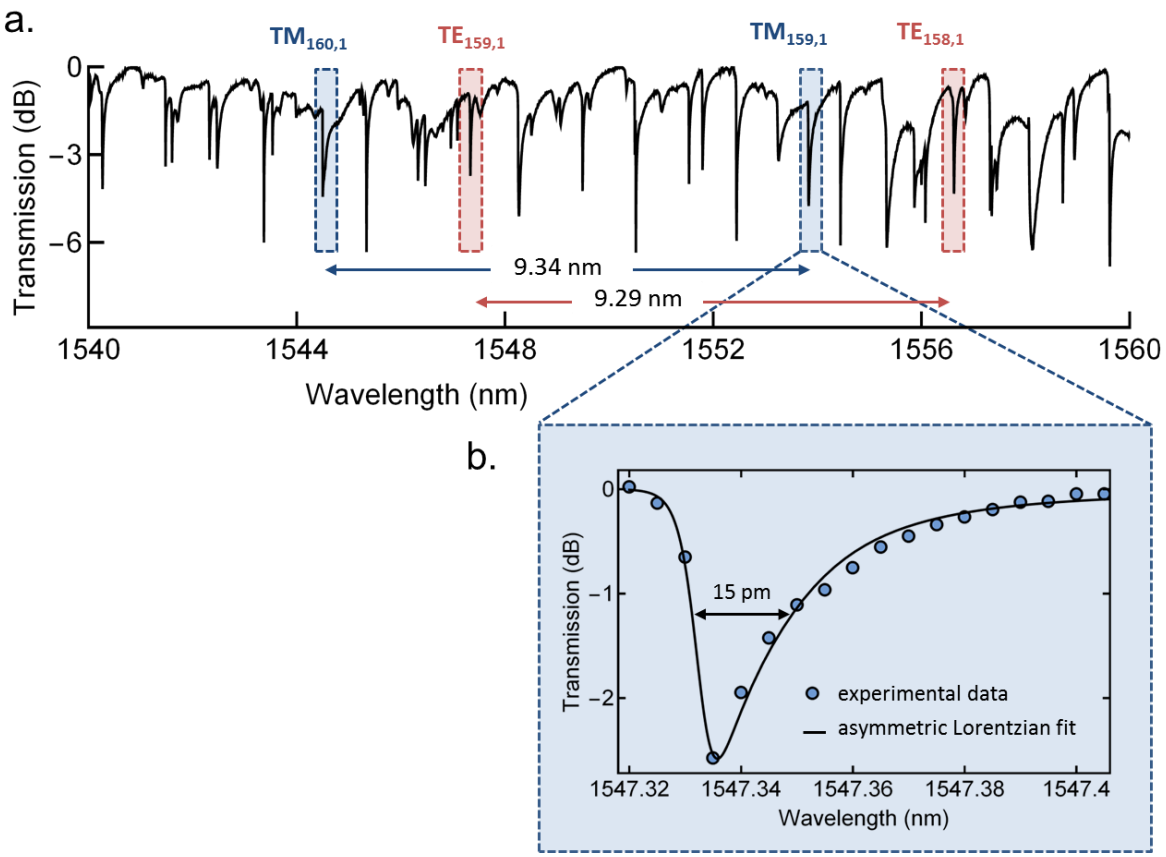

Figure 4.9 – (a) Transmission spectrum of a 1.5 um-waist diameter taper coupled to a typical polymeric microresonator. The attenuation peaks represent the resonances accounting for different azimuthal and radial orders. Highlighted in the figure are the modes identified with the help of a numerical simulation with their corresponding FSR. (b) Polymeric microresonator resonance $TE^{159,1}$ fitted to an asymmetric Lorentzian curve.
Source: Adapted from TOMAZIO *et al*[39]

The Q-factor of $TE^{159,1}$ (Fig. 4.9(b)) was calculated to be 1×10^5 by evaluating the linewidth (full width at half maximum) of the attenuation peaks, using an asymmetric Lorentzian:[121]

$$y(\lambda) = y_0\left[1 - \frac{A}{1 + \frac{4(\lambda-\lambda_0)^2}{\Delta\lambda^2}}\right], \tag{4.4}$$

in which the asymmetric linewidth ($\Delta\lambda$) varies sigmoidally according to:

$$\Delta\lambda = \frac{2\,\Delta\lambda_0}{1 + \exp[\alpha(\lambda-\lambda_0)]}. \tag{4.5}$$

In the Eqs. 4.4 and 4.5, λ is the variable wavelength of light, λ_0 and $\Delta\lambda_0$ are the resonance wavelength and linewidth (full width at half maximum), respectively, A is the Lorentzian peak value, α is the parameter that accounts for the asymmetry and y_0 is an offset correction factor. Note that, for $\alpha = 0$, $\Delta\lambda$ matches the linewidth of the symmetric Lorentzian ($\Delta\lambda_0$). Such Q-factor is slightly lower than the predicted upper limit for the Q-factor due to material intrinsic losses (1.9×10^5), indicating that the polymeric resonator Q-factor is close to its fundamental limit. It is worthwhile to mention that such high Q-factor was achieved without applying any additional material processing step (e.g. thermal reflow, etching), thereby broadening the range of materials that can be either incorporated into the polymeric matrix or deposited onto the microresonator sidewall surface.

The finesse of the polymeric resonators around 1550 nm is 840, exceeding in 66 times that reported for microring resonators fabricated using a similar material and approach.[38] Because the authors in Ref. 38[38] used a similar material, absorption is not the dominant source of losses in their microrings. Also, since their resonators are larger than ours, radiation losses can be neglected for excitation at 1550 nm. Thus, scattering losses at the surface are probably playing a major role in limiting their microring's performance, although we are not able to provide a direct comparison of the surface roughness since such characterization was not presented in Ref. 38.[38] Therefore, the high Q-factor obtained here is mainly due to the low surface

roughness achieved by the proper choice of laser power, objective lens and, overall, the degree of voxel overlap.

4.3 Conclusions

We have successfully fabricated polymeric hollow microcylinders that can potentially be used as high-Q WGM resonators for the visible and infrared wavelengths. Contrary to complex techniques used to produce polymeric microresonators, the fabrication technique used here consists of a single-step process of femtosecond laser writing, which stands for both material and geometry flexibility. The finesse of the polymeric microcylinders goes far beyond which have been achieved for microrings made from a similar material. Besides, their loaded Q-factor is close to the fundamental limit for the Q, without employing any additional processing step that would otherwise restrict the choices of material to be either incorporated into the polymeric matrix or deposited over the microresonator surface. Given these advances, these polymeric WGM microresonators are well-positioned to become an important platform for lasing, sensing and nonlinear optics research.

5 MODE CLEANING IN GRAPHENE OXIDE-DOPED POLYMERIC WHISPERING GALLERY MODE MICRORESONATORS[†]

This Chapter describes the mechanisms underlying a mode cleaning effect observed in whispering gallery mode polymeric microresonators doped with graphene oxide. It begins with a general introduction of graphene oxide properties and how they have been harnessed for the development of photonic micro/nanodevices. The following sections encompasses the typical graphene oxide-doped microresonators, the coupling setup used to interrogate them and the spectral signature of the mode cleaning, along with the methods and modeling employed to study the mechanisms behind it.

5.1 Introduction

Graphene Oxide (GO) is chemically modified graphene[122] containing oxygen functional groups, such as epoxides, alcohols and carboxylic acids on the basal plane and/or on the sheet edge.[123] It has become a highly promising member of the graphene family due to its intriguing physical and chemical properties arising from the hybridization of the sp^2- and sp^3-carbon atoms.[122-124] The manipulation of the relative fraction of the sp^2-hybridized domains of GO by either chemical or laser irradiation methods provides opportunities for tailoring its optical and electrical properties, such as conductivity, bandgap and refractive index.[125-126] Moreover, the presence of oxygen-functional groups allows GO to interact with a myriad of organic and inorganic materials in non-covalent, covalent and ionic manners.[126] This makes GO easier to process and more soluble compared to graphene, which ultimately translates into lower-cost manufacturing and easier integration into a range of photonic systems.

An efficient way to harness these properties for the development of photonic devices is to incorporate GO in a composite material.[127] Besides leveraging on the outstanding properties of GO, this strategy confers practical advantages, such as flexible packaging and on-chip integration.[127-128] GO-based composites have been used for a wide range of applications, including ultrafast lasers,[128-129] polarization

[†] Part of the results presented in this Chapter are published in Ref. 48.[48]

selective devices[130] and multimode optical recording,[131] and have been mostly patterned by 2D techniques. Nevertheless, the processing of GO-based composites by direct laser writing, which affords vast patterning and material flexibility in a single step process, has been far less explored.

In this work, we investigate the mechanisms underlying a mode cleaning observed in GO-doped whispering gallery mode (WGM) microresonators fabricated by femtosecond laser writing via two-photon polymerization using an acrylic-based photoresist doped with GO. Light was coupled to the microresonators via evanescent field through the use of tapered optical fibers. The mode cleaning was investigated by modeling the resonances with the transmission function of a straight waveguide coupled to a microresonator, which takes into account the main mechanisms of power dissipation of this system. The extra absorption and scattering introduced by GO were quantified through modeling of absorbance data obtained with the help of near-infrared spectroscopy. In addition, the GO-doped microresonators were characterized by scanning electron microscopy and by Raman spectroscopy.

5.2 Graphene oxide-doped microresonators

The photoresist composition was changed to a similar one[38] in which the monomers dipentaerythritol pentaacrylate (SR399 - Sartomer®) and tris (2-hydroxy ethyl) isocyanurate tryacrylate (SR368 – Sartomer®) are added into the photoresist in a proportion of 90/10 wt%. We have reached to these proportions following the same procedures as described in section 4.1. Graphene Oxide (GO) (Sigma Aldrich, powder, 15-20 sheets, 4-10% edge-oxidized) was ultrasonicated for 1 h in 20 mL of ethanol and incorporated into the photoresist in a concentration of 0.0025 wt%. Its molecular formula is displayed in Fig. 5.1. The suspension was kept under magnetic stirring for 24 h and left to rest until complete evaporation of the solvent (extra 24 hours). It has been shown that the combination of stirring with ultrasonication can reduce the lateral size of GO sheets to a few microns through tensile stress buildup created by drag forces during intense fluid motion.[132] Stirring followed by ultrasonication can also introduce cracking in the GO sheets through the formation of C-O groups over the carbon network, which severely weakens the bond energy between carbon atoms.[133] The fabrication methodology for the GO-doped microresonators followed the description presented in section 4.1. It is important to

mention that we have used the photoresist with the highest concentration of GO before scattering starts to impair the laser writing process. For example, the microstructures fabricated from a photoresist with GO concentration of 0.005 wt% exhibit several structural faults, which hinder their potential as optical resonators.

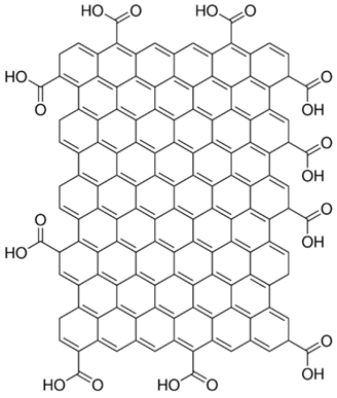

Figure 5.1 – Molecular formula of the graphene oxide obtained from Sigma Aldrich.
Source: GRAPHENE …[134]

Figure 5.2(a) shows a typical GO-doped microresonator fabricated by employing 0.1 nJ pulses (measured at the sample) from the Ti:sapphire oscillator with 40 µm/s of laser scan speed. The hollow microcylinders exhibit an outer diameter of 53 µm, 6.5 µm of sidewall thickness and approximately 150 µm of height. They feature good structural integrity and smooth sidewalls, despite the presence of GO, and low shrinkage.

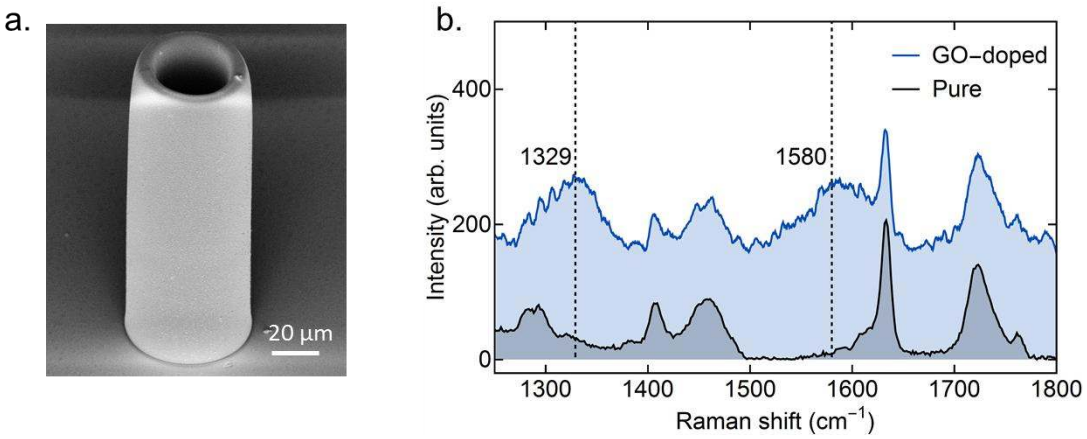

Figure 5.2 – (a) Scanning electron micrograph of a typical graphene oxide-doped microresonator fabricated by femtosecond laser writing via two-photon polymerization. (b) Raman spectra of a undoped (gray) and a GO-doped (blue) microresonator. Highlighted in the graph is the spectral position of the two peaks that indicate the presence of graphene oxide.
Source: By the author

The presence of GO in the microresonators was confirmed with Surface Enhanced Raman Spectroscopy (SERS) by coating the microresonators with a gold nanoscale layer.[135-137] The measurement was carried out in a LabRAM micro Raman system using 6 mW of a solid-state laser centered at 532 nm. Figure 5.2(b) shows the Raman spectra of a pure and a GO-doped microresonator. The GO-doped microresonator spectrum differs from that of its undoped counterpart by two prominent peaks at 1329 cm^{-1} and 1580 cm^{-1}, arising from vibrations of the sp^2 carbon of GO.[138] The D band at 1329 cm^{-1} is due to the breathing mode of the aromatic rings,[139] while the G band at 1580 cm^{-1} corresponds to the first-order scattering of the E_{2g} mode.[138] The other peaks at 1280, 1410, 1455, 1637 and 1736 cm^{-1} are respectively assigned to the =CH rock,[140] the deformation vibrations of CH_2,[140] the vibration of the photoinitiator aromatic ring[141] and the stretching of the carbon-carbon double bond (C=C) and of the carbonyl group (C=O) of the monomers.[142-144]

5.3 Light coupling into the graphene oxide-doped microresonators

The tapered fiber-based coupling setup used herein is similar to that described in section 4.2, except that a broadband source (superluminescent diode) centered at 1.53 μm was used as the excitation source and a 20 pm-resolution optical spectral analyzer (OSA) was used to measure the transmission spectrum. Besides, since the superluminescent diode is a randomly polarized light source, an in-line polarizer was added to the setup.

Figure 5.3(a) displays the set of whispering gallery modes for independent polarization states of a GO-doped microresonator in the range of 1520 to 1540 nm, excited in the undercoupling regime through a 2 μm-waist taper. Consecutive azimuthal modes could be easily identified in the spectrum, and their corresponding free spectral range (FSR) was found to be around 9.2 nm, in agreement with the expected value for these microresonators at this wavelength window (FSR = 9.34 nm at 1.53 μm). The highest extinction ratio resonance is 6.2 dB and exhibits a Q-factor of 1.1×10^4 (Fig. 5.3(a)). An asymmetric Lorentzian fit was used to determine its linewidth.[39,121] For comparison purposes, the resonance spectrum of an undoped microresonator with the same dimensions of its GO-doped counterpart is shown in Fig. 5.3(b). It was interrogated with the same taper and coupling conditions as those

employed to load the GO-doped microresonator whose resonance spectrum is shown in Fig. 5.3(a).

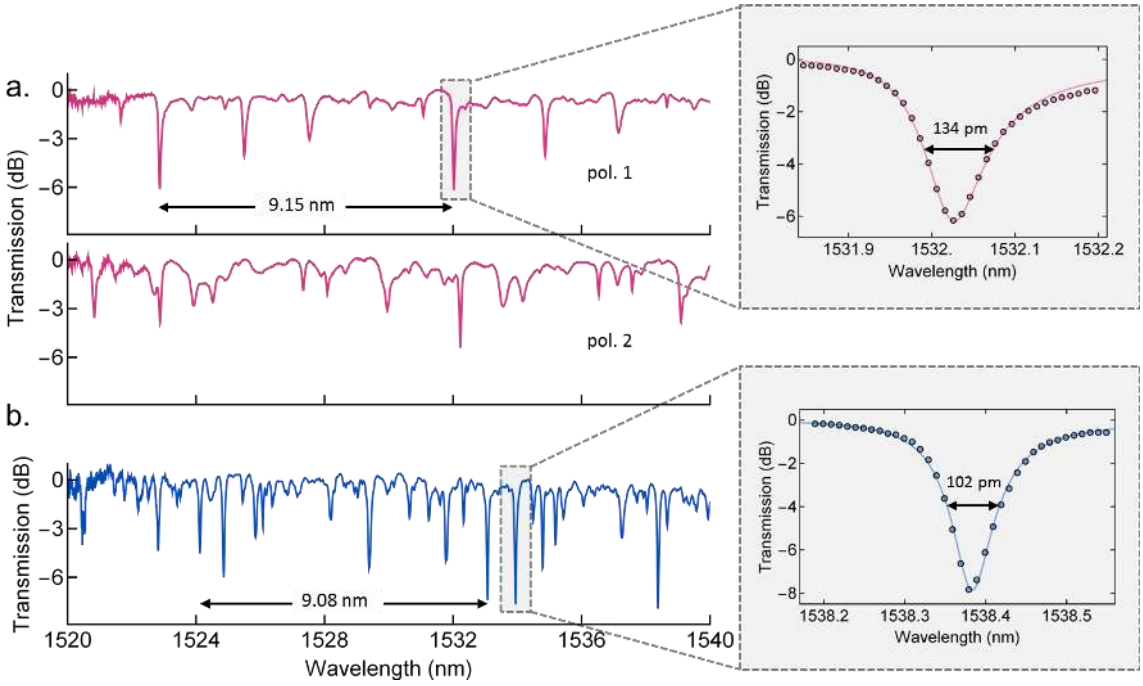

Figure 5.3 – Transmission spectra of a 2 µm-waist taper coupled to a (a) GO-doped microresonator for different polarization states (750 µW of input power) and to a (b) pure microresonator (35 µW of input power). Shown in the right-hand side are the highest extinction ratio resonances for a GO-doped (above) and for an undoped (below) microresonator. The free spectral range for both spectra is highlighted in the graphs.
Source: By the author

The undoped microresonator spectrum is filled with resonances featuring a range of extinction ratios and linewidths, regardless of the coupled power. On the other hand, notably fewer resonances were systematically observed for the GO-doped microresonators, which places the presence of GO as the determinant factor in reducing the visibility of a number of resonances up to the point of effectively filtering (cleaning out) a set of modes. Interestingly, even though the presence of GO brings up extra losses to the microresonator, the Q-factor of the highest extinction ratio resonances does not decrease significantly. As can be seen in Fig. 5.3(a-b), the linewidth of the highest extinction ratio resonance of the GO-doped microresonator spectrum is only 1.3 times broader than a resonance with similar characteristics in the undoped microresonator spectrum, which does not change the order of magnitude of the Q-factor.

It is important to notice that the mode cleaning occurs for both polarizations. This result is consistent with our hypothesis that polarization-selective effects[130] do not play a role in extinguishing certain modes. Since the GO flakes are randomly oriented throughout the microresonators, we expected any polarization-dependent effect to be averaged out along propagation.

The overall change in the resonance spectrum with the incorporation of GO was investigated by modeling the resonances with the transmission function of a straight waveguide coupled to a resonator. The transmission response of the system at the frequency ω is given by:[6,12]

$$T(\omega) = T_0 \frac{(\omega - \omega_0)^2 + \left(\frac{1}{\tau_0} - \frac{1}{\tau_c}\right)^2}{(\omega - \omega_0)^2 + \left(\frac{\Delta\omega}{2}\right)^2}, \quad (5.1)$$

which includes a sigmoid function to capture the asymmetry of the resonances:[121]

$$\Delta\omega = \frac{4\left(\frac{1}{\tau_0} + \frac{1}{\tau_c}\right)}{1 + \exp[\alpha(\omega - \omega_0)]}. \quad (5.2)$$

In the Eq. 5.1 and 5.2, T_0 is an offset correction factor, ω_0 is the resonance frequency, α is the asymmetry factor and τ_0 and τ_c are the lifetimes associated with power dissipation through intrinsic losses in the microresonator and through coupling losses, respectively.

The photon lifetime associated with intrinsic losses (τ_0) is proportional to the intrinsic Q-factor (Q_{in}):[6]

$$\tau_0 = \frac{2\,Q_{in}}{\omega_0}. \quad (5.3)$$

Q_{in} accounts for the main sources of loss in the microresonators, which are material attenuation in the volume (material absorption and scattering) and surface scattering at the resonator sidewalls. Due to the large diameter of the microresonators compared to wavelength of light, radiation losses can be neglected in this particular

case. Q_{in} can be discriminated into the Q-factors associated with material attenuation (Q_{mat}) and surface scattering ($Q_{s.s.}$) according to:[12]

$$\frac{1}{Q_{in}} = \frac{1}{Q_{mat}} + \frac{1}{Q_{s.s.}}. \tag{5.4}$$

Note that the material attenuation (Q_{mat}) and the surface scattering contribution to the Q-factor ($Q_{s.s.}$) ultimately affect the photon lifetime associated with intrinsic losses (τ_0), whose variation leads to a different transmission response for a given resonance.

The contribution of material attenuation to the intrinsic Q-factor can be determined through:[12]

$$Q_{mat} = \frac{2\,\pi\,n}{\lambda_0 \alpha}, \tag{5.5}$$

where n, λ_0 and α denote the refractive index, the resonance wavelength and the material attenuation coefficient, respectively.

The impact of the incorporation of GO on each resonance's linewidth and extinction ratio was therefore evaluated through the variation of its transmission curve in response to an increase of intrinsic losses. We adjusted the material attenuation and the surface scattering contribution to the Q-factor of each individual resonance to match both Q_{mat} and the $Q_{s.s.}$ that are expected with the incorporation of GO to the microresonator. The latter was obtained by comparing each resonance of the undoped microresonator (Fig. 5.3(b)) to the resonances of the GO-doped microresonator's spectrum (Fig. 5.3(a)) to find the best match in terms of linewidth and extinction ratio. The $Q_{s.s.}$ of the undoped resonance is then adjusted according to the $Q_{s.s.}$ of its best matched GO-doped resonance. For example, the undoped resonance tagged in Fig. 5.3(b), which exhibits 8 dB of extinction ratio and 102 pm of linewidth, had its surface scattering Q-factor decreased from 23900 to 19840 to match the $Q_{s.s.}$ of the GO-doped resonance tagged in Fig. 5.3(a) (6.2 dB of extinction ratio and 134 pm of linewidth). All the undoped resonances had their material attenuation Q-factor (Q_{mat}) adjusted according to the increase of the material attenuation coefficient (α) from 0.32 cm^{-1} (undoped polymer) to 0.8 cm^{-1} (GO-doped

polymer). Q_{mat} is calculated through Eq. 5.5. The absorbance of the undoped and the GO-doped polymer material around 1550 nm was analyzed by a Fourier Transform Infrared Spectrophotometer (IRTracer-100). For this analysis, macroscopic samples with the same composition as those of the microresonators were prepared. They are UV-cured freestanding disks with 1.1 mm of thickness and 2 cm of diameter made from both photoresists.

By modeling the experimental resonances for the undoped microresonator within a 10 nm-spectral range (blue spectrum on the left of Fig. 5.4) to simulate the incorporation of GO to the microresonator, we obtained the spectrum highlighted in Fig. 5.4 (black spectrum). The presence of GO broadens the linewidth of the resonances and decreases their extinction ratio to different extends. The resonances that are closest to the critical coupling condition, like the one tagged in Fig. 5.3(b), suffer a subtle broadening of their linewidth and have their extinction ratio decreased a little down 6 dB. On the other hand, the lowest extinction ratio resonances, which stand for over 40% of the resonance spectrum, undergo a stronger linewidth broadening and are attenuated to extinction ratio values below 1.2 dB.

As can be seen in Fig. 5.4, the overall aspect of the simulated spectrum matches reasonably well the one of the GO-doped microresonator (magenta spectrum), thus placing the linear absorption and scattering introduced by GO as the main factors behind the mode cleaning. It is important to point out that, even though the undoped and GO-doped microresonators have the same dimensions, the spectral position of their resonances cannot be matched due to a combination of factors. The microresonators suffer from polymerization shrinkage, which was minimized with the photoresist composition but cannot be completely eliminated. The shrinkage introduces a subtle conical shape to the microresonators, thus making their diameter to vary along their axis. Added to this, the taper is not guaranteed to approach the microresonator at the same height in every coupling attempt, which brings uncertainty in the determination of the resonator dimensions. These factors, combined with the thermal drift of the resonances caused by environmental perturbation and/or probe-induced noise, make it difficult to match the resonance spectrum for different microresonators, especially if they differ in composition.

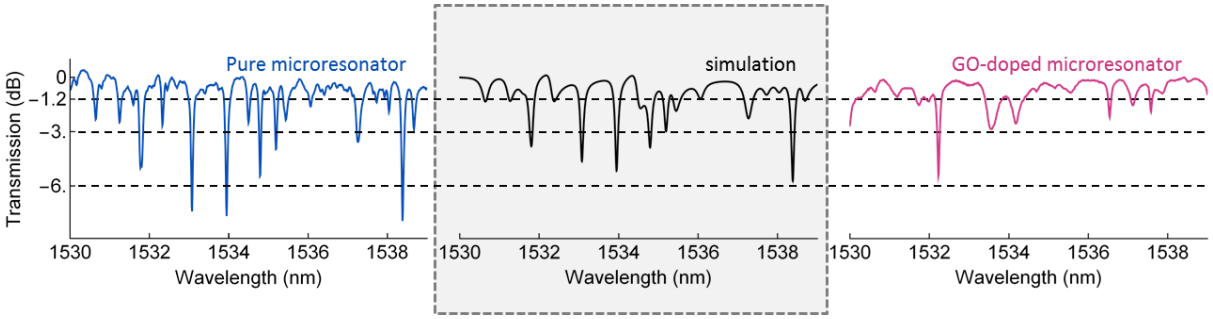

Figure 5.4 – From left to right: Resonance spectra (1530 - 1539 nm) for the pure microresonator (experimental data), for the simulation and for the GO-doped microresonator (experimental data).

Source: By the author

Further mode suppression can be caused by loss mechanisms not taken into account in the aforementioned model, such as the presence of GO agglomerates throughout the microresonator and nonlinear absorptive effects (e.g., saturable absorption[145]). The presence of GO agglomerates in the interior of the resonators, close to their inner sidewall surface, can selectively introduce losses to the modes depending on their radial order. In other words, the higher-order radial WGMs, which overlap the most with the agglomerates, are more susceptible to scattering than the most fundamental WGM. The saturable absorption contribution of GO can also affect the modes differently, and, similarly to the agglomerates, it introduces higher losses to the higher-order radial WGMs. Since the intensity profile of higher-order radial WGMs is more spread out inside the resonator, their peak intensity might not be high enough to saturate the absorption, thus rendering these modes attenuated.

5.4 Saturable absorption of the graphene oxide-polymer composite

To verify the contribution of absorptive nonlinearities to the mode filtering, we investigated the saturable absorption response of graphene oxide incorporated in the acrylate polymer at 1550 nm through femtosecond Z-scan technique in the open-aperture configuration.[48,146] To this end, macroscopic samples were prepared from a 0.05 wt% concentrated GO-doped photoresist (1.15 mm of thickness and 2 cm of diameter). For comparison purposes, pure polymer disks were also prepared. More details about the sample preparation can be found in Ref. 48.[48] It should be noted that the GO-doped macroscopic samples are 20x more concentrated than the

microresonators. Even though different concentrations change the modulation depth, they do not affect the saturation intensity, which is the focus of this study.

In the femtosecond Z-scan setup (Fig. 5.5), a Ti:sapphire laser amplifier (775 nm - Clark MXR Inc.) delivering 150 fs pulses at a 1kHz repetition rate was used as the excitation source for an optical parametric oscillator (OPA) (Quantronix, model TOPAS) that delivers 130 fs pulses in the wavelength range of 470 – 2200 nm. The OPA output beam was focused, resulting in a focus beam radius of 25 μm at 1550 nm (z_0 = 1.27 mm). To ensure the Gaussian beam profile, a spatial filter was added before the Z-scan line. The sample was translated through the focused beam with the help of a motorized stage and its transmittance across different intensity levels was acquired using a silicon photodetector. To improve the signal-to-noise ratio, we employed the oscillatory Z-scan method in which the sample is scanned through the beam multiples times and the transmittance at a given position is obtained by averaging the values measured over multiple scans.

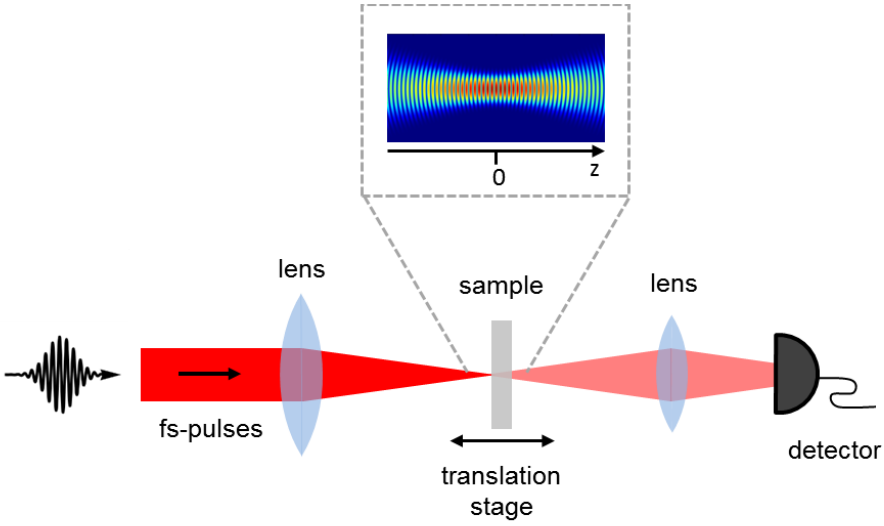

Figure 5.5 – Experimental setup for the femtosecond Z-scan technique in the open-aperture configuration.

Source: By the author

The photo-carrier dynamics of GO in the composite was described using a two-level model. The photo-carrier density evolves in time according to:[145]

$$n_2(t) = W\tau'(1 - e^{-t/\tau'}) ,$$
$$n_1(t) = 1 - n_2(t) , \quad (5.6)$$

in which $n_1(t)$ and $n_2(t)$ are the population fraction in the states 1 and 2, respectively, $W = \sigma I/h\nu$ is the pump rate and $(\tau')^{-1} = (W + 1/\tau)$. These quantities depend on the ground-state cross-section σ, the intensity I, the photon energy $h\nu$ and on the electron-hole recombination time τ.

When the pulse width is longer than the electron-hole recombination time of the system, e.g., for picosecond/nanosecond pulses and CW lasers, the interaction occurs at the steady-state regime, in which the population no longer varies over time and the attenuation coefficient is described as:[145]

$$\alpha(I) = \frac{\alpha_0}{\left(1 + \frac{I}{I_{sat}}\right)} + \alpha_p \,, \tag{5.7}$$

where α_0 and α_p are the GO and polymer host linear absorption coefficient, respectively, and $I_{sat} = h\nu/\sigma\tau$ is the saturation intensity, defined as the intensity required for the absorption coefficient to drop to half its linear contribution.

On the other hand, when the pulse width is shorter than the electron-hole recombination time, the interaction occurs in the transient regime. In this case, the temporal dependence is kept, and the absorption coefficient is described by:[48]

$$\alpha(I) = \alpha_0 \left(1 - \frac{\frac{I}{I_{sat}}}{1 + \frac{I}{I_{sat}}} \left(1 - e^{-\frac{t}{\tau}\left(\frac{I}{I_{sat}} + 1\right)} \right) \right) + \alpha_p \,. \tag{5.8}$$

The intensity of light traveling through a medium varies along the propagation direction (z) according to:[106]

$$\frac{dI}{dz} = -\alpha(I)\, I \,. \tag{5.9}$$

Following Eq. 5.9, the intensity that comes out from the medium (I_{out}) is calculated by plugging the absorption coefficient obtained for either the transient (Eq. 5.8) or steady-state (Eq. 5.7) regime into Eq. 5.9 and numerically solving the resulting transcendental equation:

$$\int_{I_{in}}^{I_{out}} \frac{dI}{\alpha(I)I} = -L\,, \tag{5.10}$$

where the integration limits I_{in} and I_{out} are the input and output intensities and L is the medium thickness. The normalized transmittance is obtained by taking the ratio I_{out}/I_{in} and dividing it by the transmittance in the linear regime.

Figure 5.6(a-b) shows the nonlinear transmittance acquired over different peak intensities for the undoped and GO-doped polymer samples. The transmittance signal for the GO-doped polymer sample grows as the intensity increases, reaching a plateau of 1.11 for intensities above 20 GW/cm^2. No transmittance increase was observed for the undoped polymer sample for intensities high enough to induce a nonlinear absorption response in the GO-doped sample, confirming that the polymer host does not contribute to the saturable absorption.

Since the excitation occurs in the femtosecond scale, which is short compared to the electron-hole recombination time reported for graphene and its derivatives (~1 ps),[147-149] the nonlinear absorption was described through equations in the transient regime. The theoretical transmittance, depicted as grey dots in Fig. 5.6(b), was obtained by solving Eq. 5.10 with the absorption coefficient given by Eq. 5.8 for a set of input intensities. The fixed parameters in Eq. 5.10 were set to α_p = 0.32 cm^{-1}, L = 0.115 cm, τ_0 = 130 fs and τ = 1.67 ps.

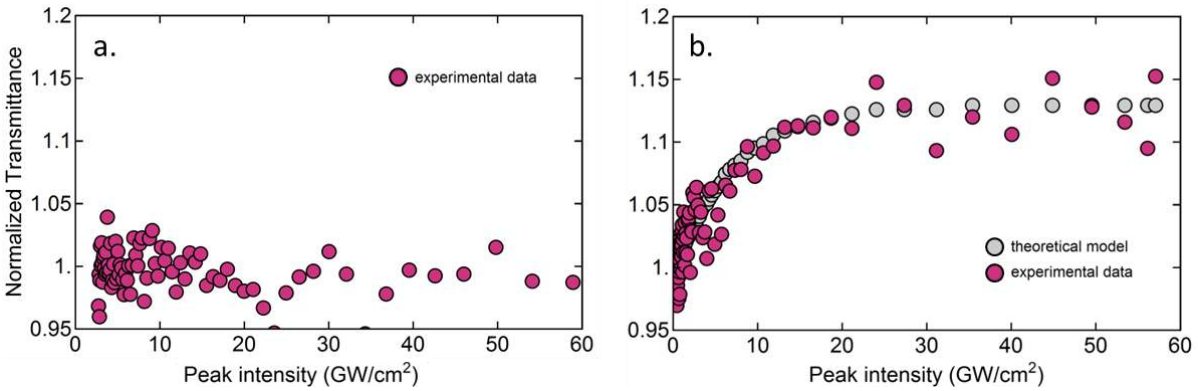

Figure 5.6 – Femtosecond Z-scan measurements carried out in the open-aperture configuration at 1550 nm for the (a) pure polymer and (b) GO-doped polymer sample. The theoretical model was obtained by solving Eq. 5.10 for a set of input intensities.
Source: Adapted from TOMAZIO *et al*[48]

By fitting the experimental data to the aforementioned model, we found the saturation intensity to be 500 MW/cm^2. Such saturation intensity is in agreement with what is expected for graphene derivatives excited in the transient regime, according to Ref. 146.[147] Though, it is important to mention that higher I_{sat} values (on the order of GW/cm^2) have been reported for GO when similar experimental conditions were employed (fs-pulses at 1 kHz of repetition rate as excitation source).[149-150] As opposed to our approach, in these works I_{sat} is determined by fitting the Z-scan transmittance data set to a two-level model in the stead-state regime, where the absorption coefficient is described as in Eq. 5.7.

The intracavity peak intensity circulating in a fundamental WGM of the GO-doped microresonator is on the order of kW/cm^2 for 1 mW of input power. To calculate the intracavity peak intensity, the mode area was determined by considering a fundamental radial mode featuring lateral and vertical spot sizes of 2 and 5 μm, respectively, and the power enhancement (P_c/P_{in}) achieved in the resonator was calculated using the expression provided in Ref. 28:[28]

$$P_c = \frac{P_{in}}{\tau} \frac{4\,\kappa_{coup}}{\left(\kappa_{coup} + \kappa_{in}\right)^2}, \tag{5.12}$$

in which P_{in}, τ, κ_{coup} and κ_{in} denote the input power, the photon lifetime in the resonator, the rate of coupling losses ($\kappa_{coup} = 1/\tau_c$) and of intrinsic losses ($\kappa_{in} = 1/\tau_0$), respectively. The parameters τ, κ_{coup} and κ_{in} for a certain resonance can be obtained by fitting it to Eq. 5.1. For example, the intracavity peak intensity for the resonance highlighted in Fig. 5.3(a) was found to be 5.3 kW/cm^2. This is several orders of magnitude lower than the intensity levels required to saturate the absorption of the GO-doped polymer, thus ruling out completely the contribution of nonlinear absorptive effects to the mode filtering.

5.5 Conclusions

In conclusion, we investigated the mechanisms behind the mode cleaning observed in GO-doped WGM polymeric microresonators fabricated in a single step of femtosecond laser writing via 2PP. Our results show that the mode cleaning occurs

for both polarizations, which renders the influence of polarization-selective effects unlikely. Even though the presence of GO brings up extra losses to the microresonator, the Q-factor of the highest extinction ratio resonances does not drop significantly. On the other hand, the low extinction ratio resonances undergo a stronger linewidth broadening and are considerably attenuated. A comparison between the simulated and experimental GO-doped microresonator spectra revealed that the major contribution to the mode cleaning arises from linear absorption and scattering introduced by GO, though the presence of GO agglomerates inside the microresonator might also be playing a role in filtering some higher-order WGMs out. Finally, the intracavity intensity achieved in the GO-doped microresonators for a pump power on the miliwatt level was found to be several orders of magnitude lower than the saturation intensity of the GO-doped polymer, which rules out completely the contribution of nonlinear absorption to the mode cleaning process. Overall, this work offers interesting physical insights that can be useful to the design and fabrication of GO-based photonic micro/nanodevices. For example, the mode cleaning strategy presented herein can be helpful to applications that rely on the resonance shift as a sensing mechanism.

6 LOW THRESHOLD DYE-DOPED POLYMERIC WHISPERING GALLERY MODE MICROLASERS†

The following chapter begins with an introduction on dye lasers and on the strategies to make them more compact and competitive with modern solid-state lasers. The next sections are devoted to a general discussion on the properties of dye molecules and their application as gain media and, overall, to the description of the typical dye-doped whispering gallery mode polymeric microlasers and their emission features.

6.1 Introduction

Pioneering studies back in the sixties demonstrated the potential of many dyes as gain material for the development of tunable coherent light sources, covering the spectrum from ultraviolet to infrared wavelengths.[151-153] The first dye lasers used liquid dye solutions as an active medium in which bleached molecules could be easily exchanged.[154] Besides, they were more easily cooled and cheaper than the solid-state laser materials available at that time.[154] From these early findings forward, many different setups were investigated. Flashlight and high intensity pump lasers were employed, with threshold excitation of tens of kW/cm^2.[154,155] The high threshold excitation intensities reported for dye laser setups from the past century were mostly caused by misalignment and successive absorptive/scattering losses inside complex cavity setups, which have been overcome with the development of mirrorless optical devices at the micro/nanoscale.

Polymers have been widely used as solid host matrices to make dye lasers more compact and competitive.[28,156] Different cavity configurations have been proposed to decrease losses and to improve light amplifications, including microcavities that exploit the index contrast at the interface of dielectric materials as a feedback mechanism,[157] distributed feedback[158] and WGM microcavities[47,159] (Fig. 6.1). The high Q-factor and tight mode confinement afforded by WGM microcavities enable strong interaction between the light field and gain material,[160] which ultimately translates into low threshold and narrow linewidth lasers.[161-163]

† The results presented in this Chapter are published in Ref. 47.[47]

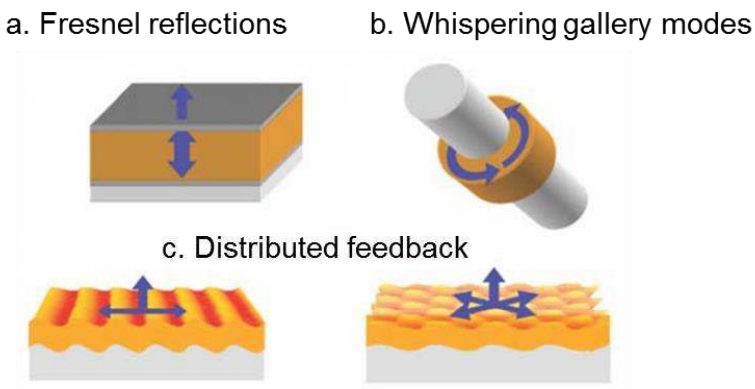

Figure 6.1 – Schematics of various polymeric microcavities for lasing. These microcavities exploit (a) Fresnel reflections, (b) whispering gallery modes and (c) periodic modulation of the refractive index as a feedback mechanism. Blue arrows indicate the resonant path and emission direction of the laser light.
Source: Adapted from SAMUEL; TURNBULL.[156]

Much effort has been directed towards the fulfillment of polymeric WGM microlasers, with the material and fabrication technique to be chosen according to the intended application.[37,159,164-166] However, the versatile fabrication of such devices with the desired photonic performance has proven challenging. In this work, we report on lasing in rhodamine B-doped WGM microcavities fabricated by femtosecond laser writing via two-photon polymerization. They were pumped with free-space picosecond excitation at 532 nm. In addition, their morphological and optical properties were characterized by scanning electron and confocal fluorescence microscopies and by UV-Vis spectroscopy.

6.2 Fundamentals

6.2.1 Photophysics of organic dyes

Organic dyes have been extensively used in the development of laser systems because they stand for wavelength tunability, high lasing efficiency and both continuous and pulsed operation with great beam quality.[151-152,154-155,167] Besides, they are flexible materials that can be used in liquid, gas and solid platforms, and their concentration, and hence their absorption and gain, is readily controlled.[154] Figure 6.2(a) displays examples of dyes typically used as active media for the development of lasers. Strictly speaking, a dye is an organic compound containing conjugated double bonds, which result in absorption of wavelengths above 200

nm.[154] As depicted in Fig. 6.2(b), the molecular plane of organic dyes is formed by σ bonds originated from the hybridized sp^2 orbitals.[168] The carbon p_z orbitals left out from hybridization overlap with each other, creating π bonds (Fig. 6.2(b)).[168] These bonds give rise to an electron cloud above and below the molecular plane, which determines the electronic transitions of the dye molecule. The transition from the ground state to the next upper energy state of the molecule occurs when an electron from the bonding π orbital undergoes a transition to the anti-bonding π* orbital.[168]

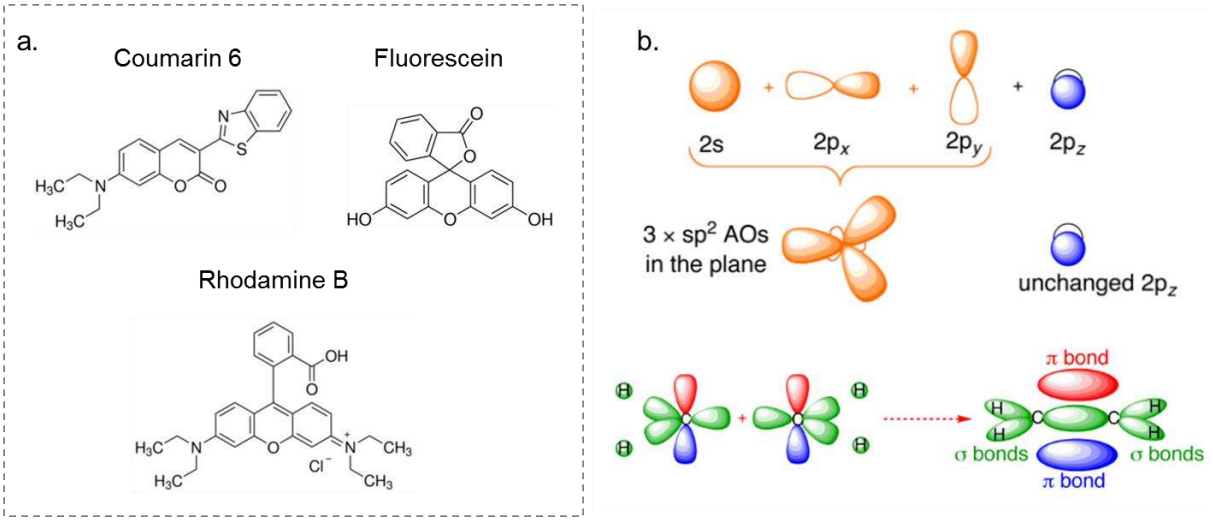

Figure 6.2 – (a) Examples of organic dyes. (b) Schematics of the formation of σ and π bonds through the hybridization of the 2s, $2p_x$ and $2p_y$ carbon orbitals and the unchanged $2p_z$ carbon orbital, respectively. σ bonds forms the molecular plane, whereas π bonds determine the electronic transitions of organic dyes. Sp^2 is the type of hybridization that gives rise to σ bonds, and AOs stand for atomic orbitals.
Source: BONDING...[169]

Opposed to their atomic and ionic counterparts, the absorption spectrum of organic dyes usually extends to tens of nanometers.[154] A typical dye molecule possesses fifty or more atoms, which leads to many normal vibrations of different frequencies coupled to the electronic transitions.[154] Also, electrostatic and collisional perturbations driven by the surrounding molecules of the solvent broaden individual vibrational lines.[154] As a further broadening effect, every vibrational sublevel of every electronic state has superimposed on it a series of rotationally excited sublevels, thereby leading to a quasicontinuum of states for every electronic level.[154]

The likelihood of any electronic-vibronic transition is dictated by the overlap integral between the wavefunction of the states involved in the transition following the Frank-Condon principle.[168,170] As shown in Fig. 6.3(a), absorption is more likely to

drive transitions starting from the electronic and vibronic ground state ($S_{0,v=0}$) to vibrationally excited sublevels of the first excited electronic state ($S_{1,v'\neq 0}$).[168] Fluorescence, on the other hand, more likely occurs from the vibrational ground state of the first excited electronic state ($S_{1,v'=0}$) and ends in vibrationally excited sublevels of the electronic ground state ($S_{0,v\neq 0}$).[168] The fluorescence spectrum thus results in a mirror image of the absorption band shifted towards larger wavelengths. The shift between the maximum of the absorption and the fluorescence spectra is referred to as Stokes shift (Fig. 6.3(b)).[171] Non-radiative relaxation between vibrational states can also occur, and they are usually extremely fast, taking place in less than 10^{-11} s.[154]

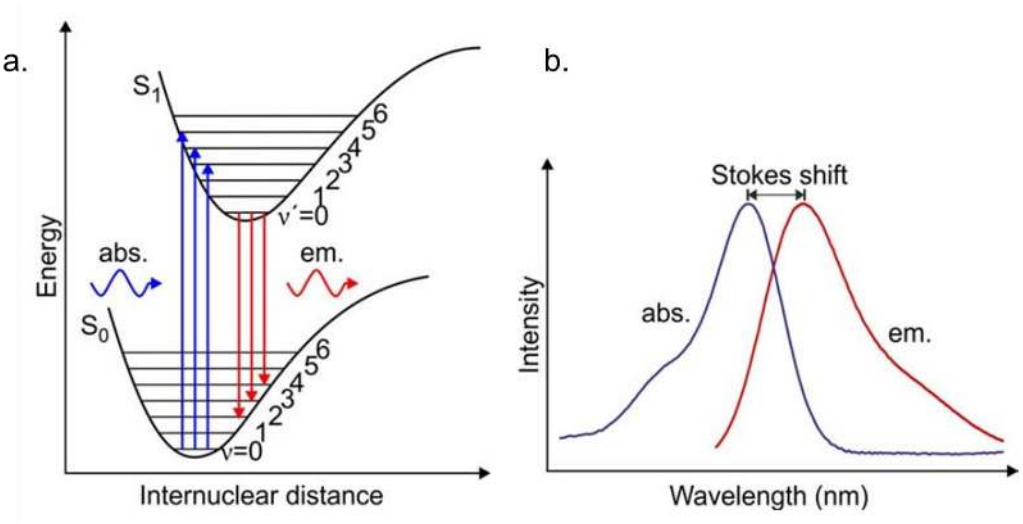

Figure 6.3 – (a) Energy diagram of a dye molecule schematically depicting the potential energy of the electronic states S_0 and S_1 as a function of the inter-nuclear distance. The horizontal lines represent vibrational states and the vertical lines give the absorption (blue) and fluorescence (red) transitions. The vibrational sublevels of the ground and of the first excited electronic states are denoted by v and v', respectively. (b) Schematic absorption and fluorescence spectra of dye molecules.
Source: GROSSMANN[168]

In addition to the above discussed singlet states, with spin state *S = 0*, triplet states (*S = 1*) also exist.[154,168] Each triplet state possesses slightly lower energy than their corresponding singlet state, and cannot be directly excited from a singlet state via electromagnetic radiation since the selection rule $\Delta S = 0$ must be fulfilled.[154] Thus, whereas singlet-singlet and triplet-triplet transitions are allowed, singlet-triplet transitions are forbidden. However, spin-orbit coupling enables the radiationless singlet-triplet transition, in a process known as intersystem crossing (ISC).[154] Even

though this process is slow compared to the fluorescence lifetime (usually 10x slower),[154] it may act as a fluorescence quencher and must be suppressed to ensure efficient laser operation. Due to the spin selection rule, triplet states are extremely long-lived with lifetimes on the order of microseconds.[154] The radiative transition from the first excited triplet state to the ground state is often referred to as phosphorescence.[154] The electronic transitions and conversion processes between energy states of dyes discussed herein are summarized in Fig. 6.4.

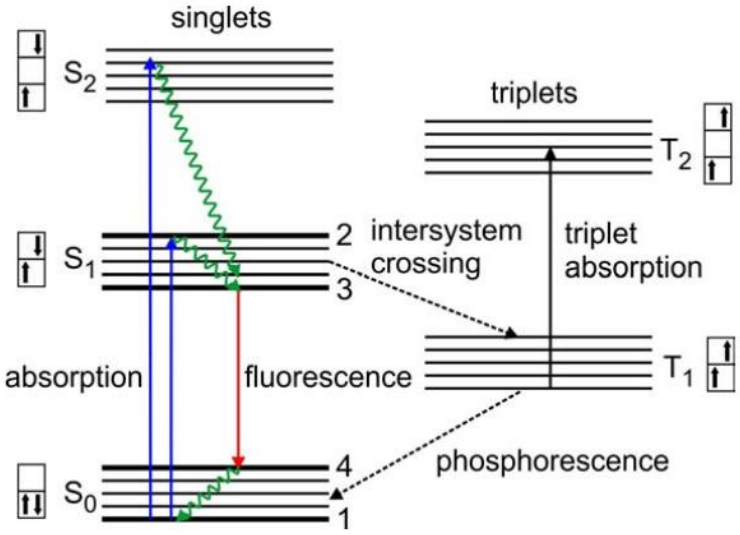

Figure 6.4 – Energy diagram illustrating the spin configuration and the processes involved in the electronic transitions of dye molecules. Solid arrows mark radiative transitions and dashed lines indicate spin-forbidden transitions. Internal conversion processes are marked by green zig-zag lines. The four states relevant for lasing are tagged in bold and numbered from one to four, following the order of the transitions.
Source: GROSSMANN[168]

6.2.2 Lasing in organic dyes

The essential building blocks for making a laser are a gain medium, a resonator/cavity for optical feedback, and a pump to achieve population inversion in the gain medium.[172] Population inversion via optical pumping is only possible for active materials with more than two energy levels.[172] Organic dyes are considered to be four-level systems due to their extremely fast radiationless transitions to vibrational ground states.[154] The four levels of a dye molecule involved in lasing are numbered in Fig. 6.4 from one to four. Since the radiationless relaxation processes of singlet states are much faster than radiative transitions, the population of dye

molecules accumulates in level 3, thus leading to an efficient build-up of population inversion.

Besides population inversion, other prerequisite for efficient lasing operation is a large stimulated emission cross-section $\sigma(\nu)$:[172]

$$\sigma(\nu) = \frac{c^2}{8\,\pi\,\nu^2\,n^2\,\tau}\,g(\nu) \tag{6.1}$$

where c denotes the speed of light, τ is the spontaneous emission lifetime, n is the medium refractive index, ν is the central frequency of the pump light and $g(\nu)$ is the molecular linewidth. From Eq. 6.1, it can be seen that the stimulated emission cross-section is essentially governed by the linewidth and other intrinsic parameters of the molecule. The typical σ for organic dyes is on the order of 10^{-16}, which is several orders of magnitude higher than the one for rare-earth crystals and it is comparable to inorganic semiconductors, such as gallium arsenide.[172] The gain coefficient is therefore written as a function of σ and the population inversion (ΔN):[172]

$$\gamma(\nu) = \sigma(\nu)\Delta N \tag{6.2}$$

As light propagates along the cavity, its intensity varies with the propagation coordinate according to the balance between the gain γ and attenuation α coefficients.[172] The attenuation coefficient takes into account all the losses experienced by light in an optical cavity, such as material absorption, scattering and diffraction. To achieve lasing, the round trip gain must overcome the total round trip losses at the lasing wavelength λ.[172] In terms of population inversion, this condition is enunciated as:[172]

$$\Delta N_{th} = \frac{8\,\pi\,\nu^2 n^2\,\tau}{c^2\,g(\nu)}\,\alpha \tag{6.3}$$

Equation 6.3 gives the minimum or threshold population inversion (ΔN_{th}) that must be created to sustain laser oscillation. The pump intensity must, therefore, be adjusted to achieve such threshold population inversion.

6.3 Dye-doped microcavities

Rhodamine B (RhB) (Sigma-Aldrich®) was first dissolved in ethanol and incorporated onto the photoresist in a concentration of 5 µmol/g of resin (6.7×10^{-3} mol/L).[159] The prepolymer resin used to prepare the RhB-doped photoresist is the same as that described in Chapter 5. The solution was mixed for half an hour and left to rest until complete evaporation of the solvent (48 hours). The fabrication methodology for the doped-microstructures followed the description presented in section 4.1.

Figure 6.5(a) displays a typical RhB-doped microcavity fabricated by employing 0.1 nJ pulses (measured at the sample) from the Ti:sapphire oscillator with 40 µm/s of laser scan speed. The hollow microcylinders exhibit an outer diameter of 50 µm, 6.5 µm of sidewall thickness and approximately 80 µm of height.

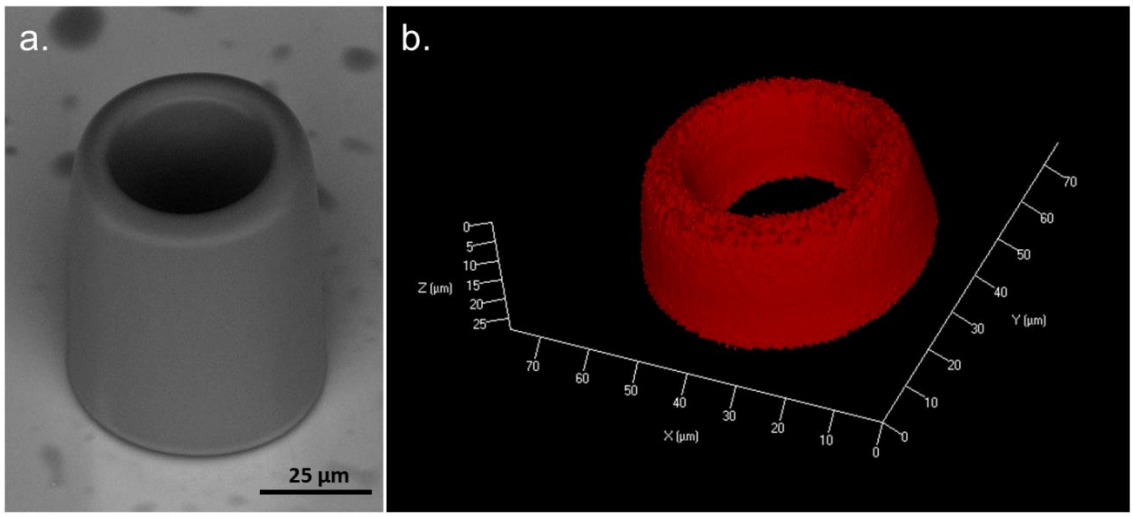

Figure 6.5 – (a) Scanning electron and (b) 3D reconstructed confocal fluorescence micrographs of a rhodamine B-doped microcavity produced by femtosecond laser writing via two-photon polymerization.

Source: TOMAZIO *et al*[47]

Contrary to previous approaches,[164; 173] rhodamine B is easily integrated into the polymer host material. To evaluate the dye distribution throughout the microcavities, we have carried out z-stack confocal fluorescence microscopy (*Zeiss LSM 700*®, 40x / NA = 0.65 Objective lens, excitation at 445 nm, w_0 = 170 nm, DoF = 400 nm, 1 µm of z-step). The reconstructed confocal fluorescence micrograph, illustrated in Fig. 6.5(b), confirms that the dye is uniformly distributed throughout the

top part of the microcavity, which contributes mostly to lasing due to the exponential decay of the pump light, coming from above, along the microstructure. Although there is a good match between the cross-sectional dimensions of both the scanning electron and the confocal micrograph, their height is different due to a measurement artifact. In addition to the exponential decay of excitation that makes fluorescence from close-to-bottom layers of the microcavity dimmer, a fraction of the light spectrum is re-absorbed by the dye molecules as fluorescence goes through the microcavity. Consequently, for an integration time set to prevent signal saturation from the close-to-top layers, fluorescence from lower layers is barely detected.

6.4 Characterization of the dye-doped microcavities emission

6.4.1 Experimental setup

The apparatus assembled for measuring the emission spectra of the RhB-doped microcavities is displayed in Fig. 6.6. As an excitation source, it uses a frequency-doubled (532 nm) Q-switched/mode-locked Nd:YAG laser operating at 100 Hz, which delivers a sequence of 100-ps pulses modulated by the Q-switched envelope (pulse train). To ensure single pulse operation, a Pockels cell and a polarizer are added to the system. Pulsed excitation prevents population transfer to the triplet lowest state, which would otherwise hinder the fluorescence quantum yield of the dye.[154] Besides, given that the fluorescence lifetime of rhodamine B is on the order of a few nanoseconds,[174] the pump carried out in the picosecond regime leads to less molecular cycles, thus extending the device lifetime. The laser beam is loosely focused on the RhB-doped microcavity top surface, resulting in a gaussian intensity profile with 100 µm of radius. As the beam spot is larger than the microcavity dimensions, the microcavity is entirely illuminated. The RhB-doped microcavity emission is acquired with a multimode optical fiber connected to a spectrometer (*Ocean Optics HR4000*®). The substrate containing the microcavities rests on an inverted microscope coupled to a CCD camera that allows real-time monitoring of the excitation process. A half-wave plate combined with a polarizer is used to adjust the optical power delivered to the microcavities.

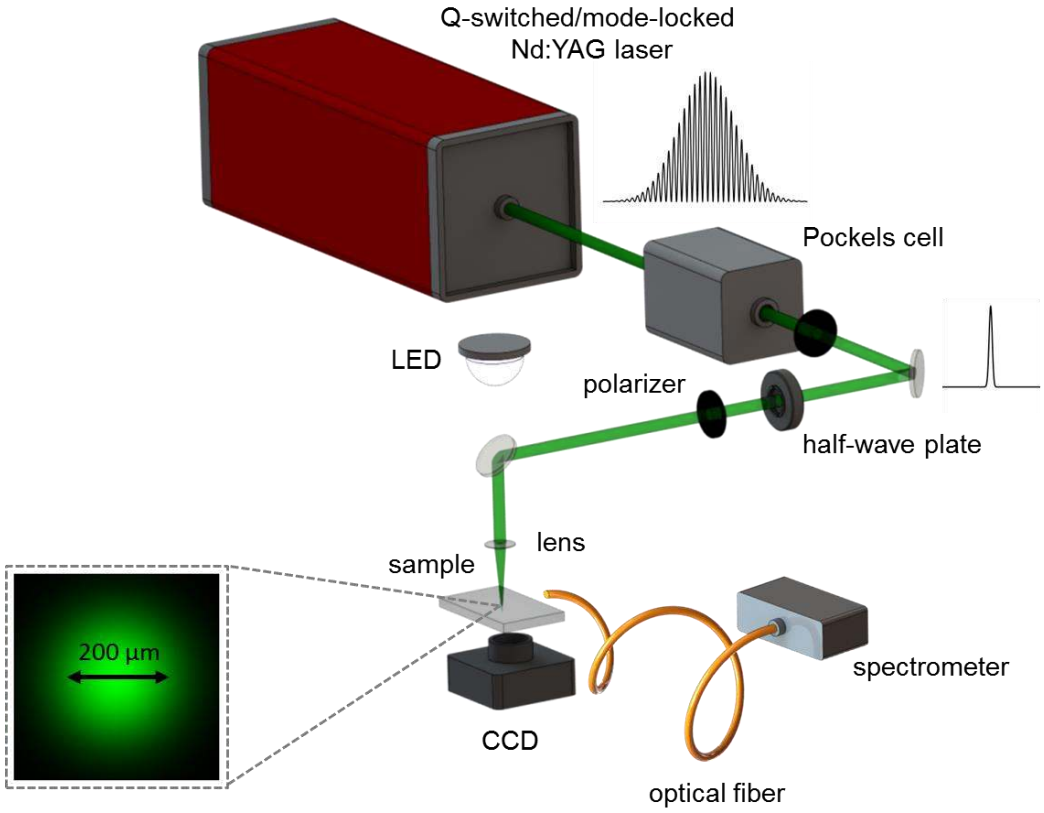

Figure 6.6 – Setup assembled to excite the rhodamine-B-doped polymeric microcavities and collect their emission.

Source: By the author

6.4.2 Emission characteristics

The absorbance of rhodamine B dissolved in both ethanol and in the acrylate polymer was measured with the help of a UV-Vis spectrometer, and its fluorescence spectrum was collected on the same setup used to measure the RhB-doped microcavity emission. These measurements were performed in macroscopic samples of RhB-doped acrylate polymer with the same composition as that used to produce the microcavities. Depicted in Fig. 6.7 are the absorption/emission spectra of rhodamine B dissolved in the acrylate polymer. They were compared to the spectra of a solution of rhodamine B dissolved in ethanol at the same dye concentration as that used to prepare the doped photoresist. The results reveal that the polymeric matrix does not affect significantly the optical properties of the dye. Indeed, the interaction with the acrylate polymer causes a 10 nm-red shift of the dye absorption and emission spectrum. In addition, it is worthwhile to point out that no dye degradation effect was observed after the laser writing process.

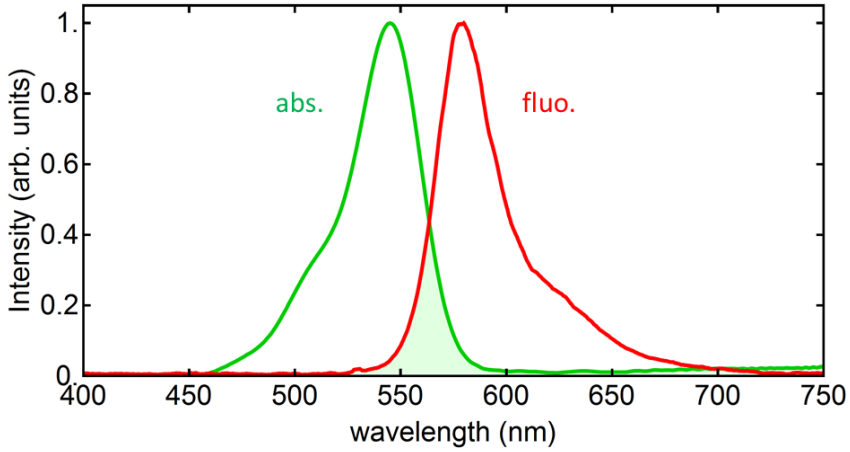

Figure 6.7 – Absorption and fluorescence spectra of an acrylate polymer sample (macroscopic) doped with rhodamine B in a concentration of 5.0 µmol/g of resin. Highlighted in light green is the overlap between both spectra.
Source: Adapted from TOMAZIO *et al*[47]

Figure 6.8(a) shows emission curves acquired for different excitation energy levels. The spectra feature a set of well-defined peaks modulated by a lorentzian-shape envelope with maximum at 600 nm and 10 nm of full width at half maximum (FWHM). Despite the broad emission spectrum of rhodamine B that extends from 550 to 700 nm, the peaks show up only within a narrow spectral window, indicating the onset of laser action. The spectral spacing between consecutive modes within the FWHM of RhB emission spectra was compared to the microcavity free spectral range (FSR). The refractive index of the acrylate polymer over visible wavelengths was measured with the help of a Carl Zeiss Jena Pulfrich Refractometer PR2® (e.g., n = 1.517 at 600 nm). The average FSR taken over all emission curves (e.g., $\mathrm{FSR} = 1.32$ nm at 600 nm) matched the theoretical values within the instrumental error (0.25 nm of spectrometer resolution), thereby attributing lasing to the whispering gallery modes.

The loaded Q-factor, inferred from the peak linewidth, is 1.5×10^3. However, as the peaks are not properly resolved by the spectrometer, nor are the excitation/detection axially localized, we believe the Q-factor to be underestimated. One expects the intrinsic Q-factor of the doped microcavities to not change significantly at 600 nm as compared to the intrinsic Q around 1550 nm. At 600 nm, the attenuation coefficient may drop an order of magnitude (due to the lower absorption of the acrylate polymer at the visible spectrum), scaling up the absorption-limited Q-factor (Q_{mat}).[25] On the other hand, as the ratio $\frac{\sigma}{\lambda}$ ($\sigma \equiv$ surface roughness)

grows for shorter wavelengths, the surface-scattering-limited Q-factor ($Q_{s.s.}$) falls off around 600 nm,[25] which may compensate the rise of Q_{mat}.

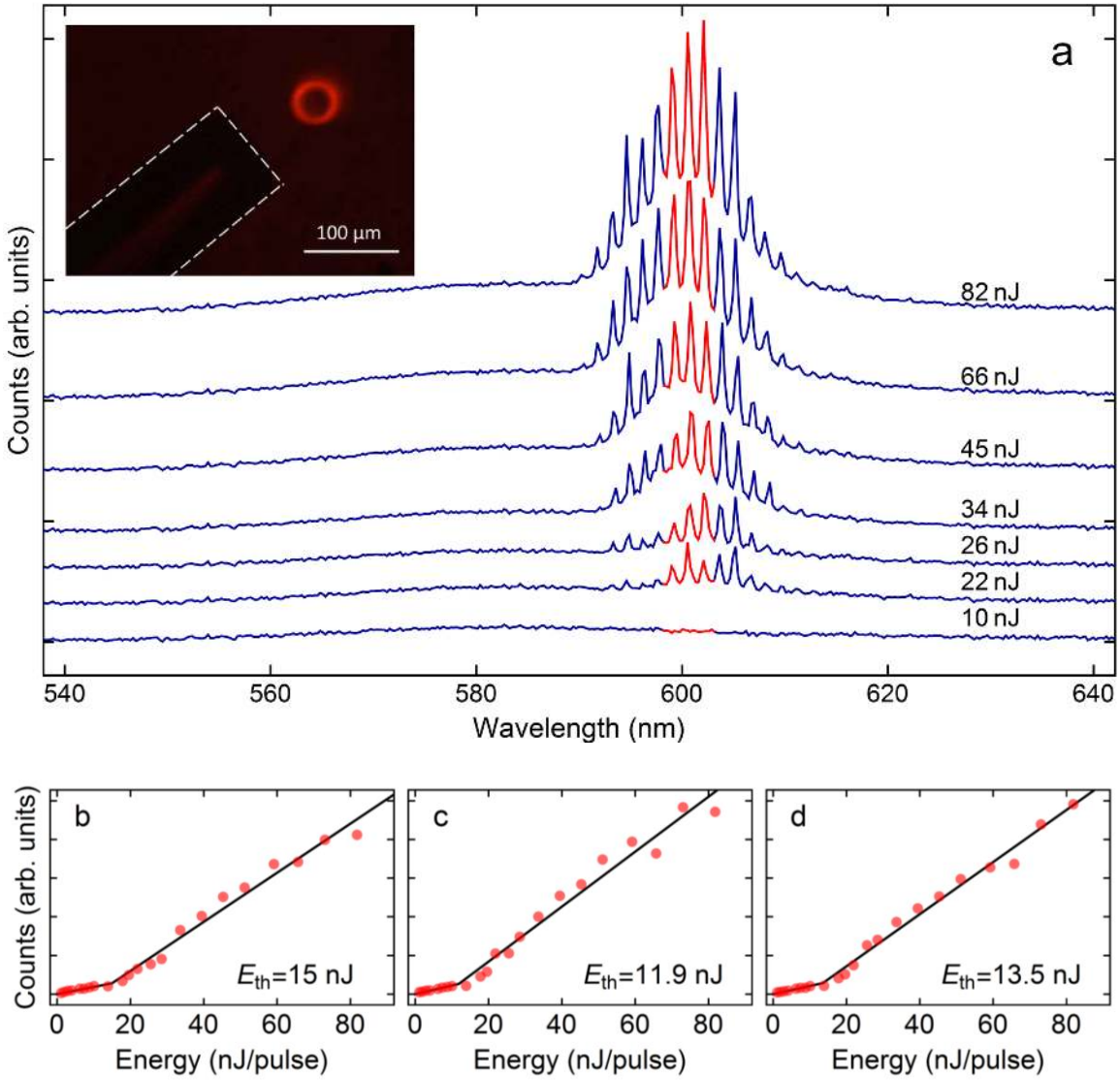

Figure 6.8 – (a) Emission spectra of a rhodamine B-doped microcavity for the excitation energy levels indicated in the right hand side of the graph. To make the visualization easier, an offset was applied to the y-axis of each curve. The first curve represents the spectrum below lasing threshold. The inset shows an image of the microlaser being excited at 82 nJ of input energy. Its emission is collected through an optical fiber (highlighted with a dashed white contour). (b), (c) and (d) Represents the growth of the peaks tagged in red in (a) as a function of the excitation energy. The graphs are plotted on a linear scale. Threshold energies, which were obtained by fitting the experimental data with bilinear curves (black lines), are shown in each corresponding graph.
Source: TOMAZIO *et al*[47]

The bilinear behavior of the integrated intensity collected from the dye microlaser was obtained by plotting the amplitude of each peak present in the emission spectra as a function of the excitation energy (Fig. 6.8(b-d)). As the lasing

threshold depends on the wavelength, it varies slightly for different peaks. The lowest lasing threshold, measured at 12 nJ of pulse energy, occurred to the peak at the maximum of emission spectra. Such low threshold is comparable to which have been achieved for polymeric microlasers fabricated by other techniques,[37,159,175] and is a direct result of the great power density achieved within whispering gallery mode microcavities, combined with the high fluorescence quantum yield of rhodamine B.[28,176-177]

In principle, the crosslinked polymeric matrix may act as a scattering media, which combined with the presence of the dye, may lead to random lasing effects.[178-179] To evaluate such possibility, the emission spectra of RhB-doped cubic hollow microstructures, which do not support WGMs, were compared with those of the microcylinders. The microcubes (Fig. 6.9(a)) were fabricated by means of the same setup described herein and exhibit the same composition and volume as of the microcylinders. As can be seen in Fig. 6.9(b), for the same pump energy levels as those used to excite the microcylinders, the spectra do not exhibit either peaks or a kink in the output versus input energy plot, revealing that random effects do not play a role in lasing threshold.

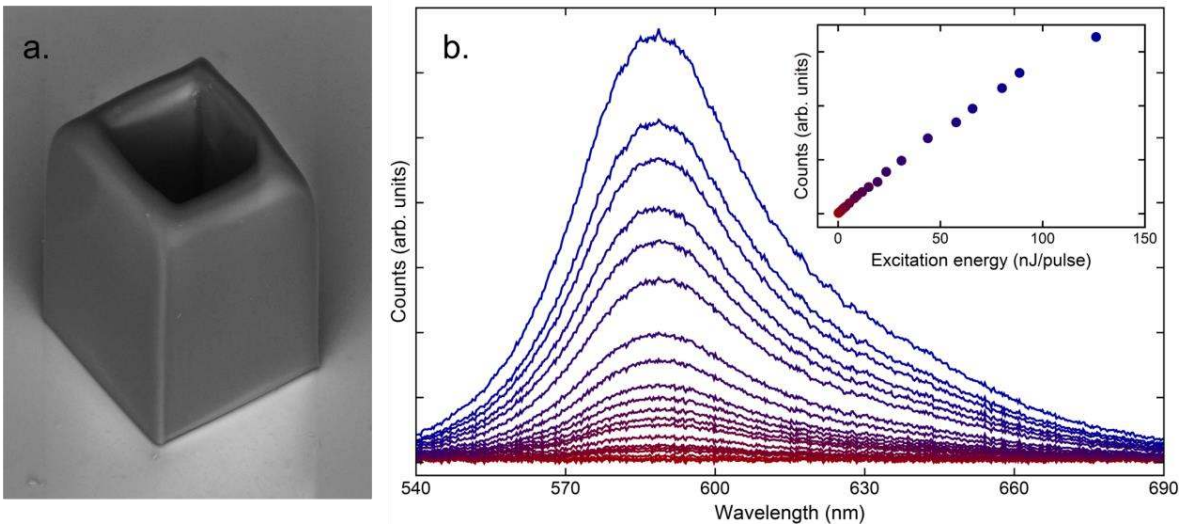

Figure 6.9 – (a) Scanning electron micrograph of a hollow microcube doped with rhodamine B (5.0 µmol/g of resin). (b) Emission spectra of the dye-doped microcube depicted in (a) taken for several excitation energy levels. Indicated in the inset is the growth of the integrated emission intensity of the dye-doped microcube as a function of excitation energy. The colour scale identifies the emission curves.
Source: TOMAZIO *et al*[47]

6.5 Conclusions

In summary, laser action in dye-doped polymeric microresonators fabricated by femtosecond laser writing via 2PP was demonstrated. Rhodamine B is easily integrated into the polymeric host matrix, which does not affect substantially the optical properties of the dye. As a result of their great surface optical quality and the high fluorescence quantum yield of RhB, the microlasers exhibited lasing threshold at a pump energy as low as 12 nJ for free space pulsed excitation at 532 nm. The measured free spectral range is in good agreement with its expected value, revealing that lasing occurs in whispering gallery modes. Besides, no lasing was observed in doped microcubes fabricated with the same composition and volume as those of the microcylinders, thus ruling out the influence of random lasing effects on the measured lasing threshold. This work therefore demonstrates the potential of femtosecond laser writing via 2PP in fabricating low threshold microlasers, which can potentially work as bright light sources for integrated optics applications.

7 CONCLUDING REMARKS AND PERSPECTIVES

We have successfully fabricated high-Q polymeric WGM microresonators, which can find numerous applications in photonics. As opposed to the complex and multi-step techniques employed to produce microresonators, the fabrication technique used herein consists of a single-step process of femtosecond laser writing, which stands for both material and geometry flexibility. The microresonators feature good structural quality and smooth sidewalls, a result of the appropriate proportion of the monomers in the photoresist combined with the proper degree of voxel overlap achieved through optimal microfabrication parameters. Through atomic force microscopy measurements taken directly on the microresonator's sidewall surface, we showed that their sidewall surface roughness is less than 2 nm, which makes the microresonators a compelling platform for applications at the visible and infrared wavelengths. Moreover, they can be fabricated onto different platforms/substrates and their dimensions can be controllably changed.

By coupling light to the microresonators with the aid of tapered fibers, we were able to excite the WGMs and quantify the microresonators' performance. We showed that the polymeric microresonators can achieve a loaded Q-factor as high as 1×10^5 at 1550 nm, which, to the best of our knowledge, is the highest Q-factor achieved for an organic microresonator fabricated by femtosecond laser writing. Given the low surface roughness of the microresonators and the small gap between the loaded and the absorption-limited Q-factors, the acrylate polymer absorption is likely to be the main limit to the microresonator's Q-factor at 1550 nm.

The material flexibility afforded by the femtosecond laser writing technique allowed us to incorporate different active compounds to the microresonator, which gave rise to interesting optical processes that can be exploited for the development of on-chip integrated devices in soft photonic platforms. The incorporation of graphene oxide to the microresonators produced a selective mode-suppression effect that can be used as a strategy to clean up the resonance spectrum for certain applications. By modeling the resonance spectrum with the transmission function of a straight waveguide coupled to a microresonator, we showed that the extra linear absorption and scattering brought up by GO are the determinant factors in cleaning up the spectrum. Interestingly, although the presence of GO attenuates low extinction ratio resonances, it does not hinder considerably the Q-factor of the deepest

resonances, for which most of the power is coupled. Also, we suggested that the presence of residual GO agglomerates spread inside the microresonator might contribute with further mode suppression by filtering some higher-order WGMs out.

In another study, we doped the microresonators with rhodamine B aiming to exploiting laser action. We showed that RhB is homogeneously embedded in the polymeric microstructure, and that the laser writing process does not cause degradation to the dye molecules. To excite the RhB-doped microresonators and collect their emission, we assembled a setup based on free-space optics, which avoids difficulties related to light coupling using tapered fibers. The pumping of the RhB-doped microresonators with increasing intensity levels led to a set of WGMs pointing up within a narrow window in the emission spectrum. For the WGM at the center of the emission spectrum, a lasing threshold as low as 12 nJ was achieved. Such a low threshold is comparable to which has been achieved for polymer microlasers fabricated by more complex techniques, and is a direct result of the great power enhancement reached in WGM microresonators, combined with the high fluorescence quantum yield of RhB.

Many possibilities are left as continuations of this work. To move forward on the study of lasing, one can leverage the material flexibility afforded by the femtosecond laser writing process to produce WGM microlasers incorporated with other active materials, such as rare-earth ions and semiconducting polymers, targeting at specific properties. For instance, semiconducting polymers can be pumped either optically and electrically, thus holding a great prospect for the development of electrically pumped compact microlasers. To enable further advancement of the present platform for applications in sensing and nonlinear optics, the control of its thermo-optic effects is key. The thermal drift of WGMs caused by environmental perturbation and probe-induced noise degrades the high sensitivity and the strength of nonlinear phenomena in microresonators considerably. Therefore, it would be useful to fully understand the thermo-optic dynamics in the polymeric microresonators and develop strategies to have it under control. In addition, given the high-intensity levels required to sustain nonlinear effects, it would be interesting to characterize the thermal damage threshold of the acrylate polymer.

Overall, this work demonstrates the potentiality of femtosecond laser writing via 2PP in fabricating high-performance optical microdevices and offers interesting

physical insights that can be helpful towards the design and fabrication of micro/nanodevice

REFERENCES

1 MAIMAN, T. H. Stimulated optical radiation in ruby. **Natur**e, v. 187, n. 4736, p. 493-494, 1960.

2 MILLER, S. E.; MARCATILI, E. A. J.; LI, T. A. Research toward optical-fiber transmission-systems. **Proceedings of the IEEE**, v. 61, n. 12, p. 1703-1704, 1973.

3 NOBEL LAUREATES. The Optical Society.
Available from: https://www.osa.org/en-us/about_osa/osa_nobel_laureates/
Accessible at: 19 Feb. 2020

4 ECONOMIC IMPACT. 2015 international year of Light and light-based technologies. Available from:
http://www.light2015.org/Home/WhyLightMatters/Economic-Impact.html.
Accessible at: 19 Feb. 2020

5 SALEH, B. E. A.; TEICH, M. C. **Fundamentals of photonics**. Hoboken: John Wiley & Sons, 1991.

6 POLLOCK, C. R.; LIPSON, M. **Integrated photonic**s. New York: Springer Science+Business Media, 2003.

7 NAGARAJAN, R. *et al*. Large-scale photonic integrated circuits. **IEEE Journal of Selected Topics in Quantum Electronics**, v. 11, n. 1, p. 50-65, 2005.

8 O'BRIEN, J. L.; FURUSAWA, A.; VUCKOVIC, J. Photonic quantum technologies. **Nature Photonics**, v. 3, n. 12, p. 687-695, 2009.

9 THOMAS-PETER, N. *et al*. Integrated photonic sensing. **New Journal of Physics**, v. 13, n. 055024, p. 1-20, 2011.

10 SHACHAM, A.; BERGMAN, K.; CARLONI, L. P. Photonic networks-on-chip for future generations of chip multiprocessors. **IEEE Transactions on Computers**, v. 57, n. 9, p. 1246-1260, 2008.

11 VAHALA, K. J. Optical microcavities. **Nature**, v. 424, n. 6950, p. 839-846, 2003.

12 RIGHINI, G. C. *et al*. Whispering gallery mode microresonators: fundamentals and applications. **Rivista del Nuovo Cimento**, v. 34, n. 7, p. 435-488, 2011.

13 WARD, J.; BENSON, O. WGM microresonators: sensing, lasing and fundamental optics with microspheres. **Laser & Photonics Reviews**, v. 5, n. 4, p. 553-570, 2011.

14 IBRAHIM, T. A. *et al*. All-optical AND/NAND logic gates using semiconductor microresonators. **IEEE Photonics Technology Letters**, v. 15, n. 10, p. 1422-1424, 2003.

15 VOLLMER, F.; ARNOLD, S.; KENG, D. Single virus detection from the reactive shift of a whispering-gallery mode. **Proceedings of the National Academy of Sciences of the United States of America**, v. 105, n. 52, p. 20701-20704, 2008.

16 MATSKO, A. B.; ILCHENKO, V. S. Optical resonators with whispering-gallery modes - Part I: basics. **IEEE Journal of Selected Topics in Quantum Electronics**, v. 12, n. 1, p. 3-14, 2006.

17 RAYLEIGH, L. The problem of the whispering gallery. **Philosophical Magazine**, v. 20, n. 115-20, p. 1001-1004, 1910.

18 SORIA, S. *et al*. Optical microspherical resonators for biomedical sensing. **Sensors**, v. 11, n. 1, p. 785-805, 2011.

19 COLLOT, L. *et al*. Very high-Q whispering-gallery mode resonances observed on fused-silica microspheres. **Europhysics Letters**, v. 23, n. 5, p. 327-334, 1993.

20 BRAGINSKY, V. B.; GORODETSKY, M. L.; ILCHENKO, V. S. Quality-factor and nonlinear properties of optical whispering-gallery modes. **Physics Letters A**, v. 137, n. 7-8, p. 393-397, 1989.

21 ARMANI, D. K. *et al*. Ultra-high-Q toroid microcavity on a chip. **Nature**, v. 421, n. 6926, p. 925-928, 2003.

22 SAVCHENKOV, A. A. *et al*. Kilohertz optical resonances in dielectric crystal cavities. **Physical Review A**, v. 70, n. 051804, p. 1-4, 2004.

23 GRUDININ, I. S. *et al*. Ultra high Q crystalline microcavities. **Optics Communications**, v. 265, n. 1, p. 33-38, 2006.

24 ILCHENKO, V. S. *et al*. Nonlinear optics and crystalline whispering gallery mode cavities. **Physical Review Letters**, v. 92, n.4, p. 043903, 2004.

25 GORODETSKY, M. L.; SAVCHENKOV, A. A.; ILCHENKO, V. S. Ultimate Q of optical microsphere resonators. **Optics Letters**, v. 21, n. 7, p. 453-455, 1996.

26 VERNOOY, D. W. *et al*. High-Q measurements of fused-silica microspheres in the near infrared. **Optics Letters**, v. 23, n. 4, p. 247-249, 1998.

27 FENG, S. Q. *et al*. Silicon photonics: from a microresonator perspective. **Laser & Photonics Reviews**, v. 6, n. 2, p. 145-177, 2012.

28 HE, L. N.; OZDEMIR, S. K.; YANG, L. Whispering gallery microcavity lasers. **Laser & Photonics Reviews**, v. 7, n. 1, p. 60-82, 2013.

29 SHAINLINE, J. M. *et al*. Broad tuning of whispering-gallery modes in silicon microdisks. **Optics Express**, v. 18, n. 14, p. 14345-14352, 2010.

30 TAMBOLI, A. C. *et al*. Room-temperature continuous-wave lasing in GaN/InGaN microdisks. **Nature Photonics**, v. 1, n. 1, p. 61-64, 2007.

31 SHITIKOV, A. E. *et al*. Billion Q-factor in silicon WGM resonators. **Optica**, v. 5, n. 12, p. 1525-1528, 2018.

32 RABIEI, P. *et al*. Polymer micro-ring filters and modulators. **Journal of Lightwave Technology**, v. 20, n. 11, p. 1968-1975, 2002.

33 GROSSMANN, T. *et al*. High-Q conical polymeric microcavities. **Applied Physics Letters**, v. 96, n. 1, p. 013303, 2010.

34 CHAO, C. Y.; GUO, L. J. Polymer microring resonators fabricated by nanoimprint technique. **Journal of Vacuum Science & Technology B**, v. 20, n. 6, p. 2862-2866, 2002.

35 MARTIN, A. L. *et al*. Replica-molded high-Q polymer microresonators. **Optics Letters**, v. 29, n. 6, p. 533-535, 2004.

36 DONG, C. H. *et al*. Fabrication of high-Q polydimethylsiloxane optical microspheres for thermal sensing. **Applied Physics Letters**, v. 94, n. 23, p. 231119, 2009.

37 ZHANG, C. *et al*. Organic printed photonics: from microring lasers to integrated circuits. **Science Advances**, v. 1, n. e1500257, p. 1-7, 2015.

38 LI, L. *et al*. High-performance microring resonators fabricated with multiphoton absorption polymerization. **Advanced Materials**, v. 20, n. 19, p. 3668-3671, 2008.

39 TOMAZIO, N. B. *et al*. Femtosecond laser fabrication of high-Q whispering gallery mode microresonators via two-photon polymerization. **Journal of Polymer Science Part B:** polymer physics, v. 55, n. 7, p. 569-574, 2017.

40 KAWATA, S. *et al*. Finer features for functional microdevices: micromachines can be created with higher resolution using two-photon absorption. **Nature**, v. 412, n. 6848, p. 697-698, 2001.

41 OTUKA, A. J. G. *et al*. Emission features of microstructures fabricated by two-photon polymerization containing three organic dyes. **Optical Materials Express**, v. 2, n. 12, p. 1803-1808, 2012.

42 TRIBUZI, V. *et al*. Indirect doping of microstructures fabricated by two-photon polymerization with gold nanoparticles. **Optics Express**, v. 20, n. 19, p. 21107-21113, 2012.

43 TRIBUZI, V. *et al*. Birefringent microstructures fabricated by two-photon polymerization containing an azopolymer. **Optical Materials Express**, v. 3, n. 1, p. 21-26, 2013.

44 XU, Q. F. *et al*. Micrometre-scale silicon electro-optic modulator. **Nature,** v. 435, n. 7040, p. 325-327, 2005.

45 LACEY, S. *et al*. Versatile opto-fluidic ring resonator lasers with ultra-low threshold. **Optics Express**, v. 15, n. 23, p. 15523-15530, 2007.

46 MA, R. *et al*. Radiation-pressure-driven vibrational modes in ultrahigh-Q silica microspheres. **Optics Letters**, v. 32, n. 15, p. 2200-2202, 2007.

47 TOMAZIO, N. B.; DE BONI, L.; MENDONCA, C. R. Low threshold Rhodamine-doped whispering gallery mode microlasers fabricated by direct laser writing. **Scientific Reports**, v. 7, n. 8559, p. 1-5, 2017.

48 TOMAZIO, N. B. *et al*. Saturable absorption in graphene oxide-doped acrylate polymer used for direct laser writing. *In*: INTERNATIONAL OPTICS AND PHOTONICS CONFERENCE, SBFOTON IOPC, 2019, São Paulo. **Proceedings […]**. São Paulo: IEEE Xplore, 2019, p. 1-4.

49 ORAEVSKY, A. N. Whispering-gallery waves. **Quantum Electronics**, v. 32, n. 5, p. 377-400, 2002.

50 DEBYE, P. The heliograph of spheres of any material. **Annalen der Physik**, v. 30, n. 11, p. 57-136, 1909.

51 ZAMORA, V. *et al*. Cylindrical optical microcavities: Basic properties and sensor applications. **Photonics and Nanostructures:** fundamentals and applications, v. 9, n. 2, p. 149-158, 2011.

52 POELLINGER, M. *et al*. Ultrahigh-Q tunable whispering-gallery-mode microresonator. **Physical Review Letters**, v. 103, n. 5, p. 053901, 2009.

53 TOMAZIO, N. B. **Fabricação de micro-ressonadores ópticos via fotopolimerização por absorção de dois fótons**. 2016. 102p. Dissertação (Mestrado em Ciências) - Instituto de Física de São Carlos, Universidade de São Paulo, São Carlos, 2016.

54 MECHÓ, X. R. **Resonancias ópticas acimutales de microcilindros de sílice sometidos a tensión axial**. 2014. 45p. Dissertation (Máster en Física Avanzada) - Facultat de Física, Universitat de València, València, 2014.

55 SUMETSKY, M. Mode localization and the Q-factor of a cylindrical microresonator. **Optics Letters**, v. 35, n. 14, p. 2385-2387, 2010.

56 ZAMORA, V. *et al*. Refractometric sensor based on whispering-gallery modes of thin capillaries. **Optics Express**, v. 15, n. 19, p. 12011-12016, 2007.

57 ABRAMOWITZ, M.; STEGUN, A. **Handbook of mathematical functions**. New York: Dover Publications, 1972.

58 LAFRATTA, C. N. *et al*. Multiphoton fabrication. **Angewandte Chemie:** international edition, v. 46, n. 33, p. 6238-6258, 2007.

59 KELLEY, P. L. Self-focusing of optical beams. **Physical Review Letters**, v. 15, n. 26, p. 1005-1007, 1965.

60 GORODETSKY, M. L.; ILCHENKO, V. S. Optical microsphere resonators: optimal coupling to high-Q whispering-gallery modes. **Journal of the Optical Society of America B:** optical physics, v. 16, n. 1, p. 147-154, 1999.

61 ILCHENKO, V. S.; YAO, X. S.; MALEKI, L. Pigtailing the high-Q microsphere cavity: a simple fiber coupler for optical whispering-gallery modes. **Optics Letters**, v. 24, n. 11, p. 723-725, 1999.

62 CAI, M.; PAINTER, O.; VAHALA, K. J. Observation of critical coupling in a fiber taper to a silica-microsphere whispering-gallery mode system. **Physical Review Letters**, v. 85, n. 1, p. 74-77, 2000.

63 BIRKS, T. A.; LI, Y. W. The shape of fiber tapers. **Journal of Lightwave Technology**, v. 10, n. 4, p. 432-438, 1992.

64 KNIGHT, J. C. *et al*. Phase-matched excitation of whispering-gallery-mode resonances by a fiber taper. **Optics Letters**, v. 22, n. 15, p. 1129-1131, 1997.

65 MANOLATOU, C. **Passive components for dense optical integration based on high index-contrast**. 2001. 185p. Ph. D. Thesis (Doctor of Philosophy) - Massachusetts Institute of Technology, Massachusetts, 2001.

66 HAUS, H. A. **Waves and fields in optoelectronics**. New Jersey: Prentice Hall, 1984.

67 DUMEIGE, Y. *et al*. Determination of coupling regime of high-Q resonators and optical gain of highly selective amplifiers. **Journal of the Optical Society of America B:** optical physics, v. 25, n. 12, p. 2073-2080, 2008.

68 KIPPENBERG, T. J. A. **Nonlinear optics in ultra-high-Q whispering-gallery optical microcavities**. 2004. 185p. PH. D**.** Thesis (Doctor in Science) - California Institute of Technology, Pasadena, 2004.

69 YANG, L. **Fabrication and characterization of microlasers by the sol-gel method**. 2005. 132p. Ph. D. Thesis (Doctor in Science) - California Institute of Technology, Pasadena, 2005.

70 GOEPPERT-MAYER, M. Elementary processes with two quantum transitions. **Annalen der Physik**, v. 18, n. 7-8, p. 466-479, 2009.

71 KAISER, W.; GARRETT, C. G. B. 2-photon excitation in CaF_2-Eu^{2+}. **Physical Review Letters,** v. 7, n. 6, p. 229-230, 1961.

72 SAMAD, R.; COURROL, L.; BALDOCHI, S.; VIEIRA, N. Ultrashort laser pulses applications. *In*: DUARTE, F. J. **Coherence and ultrashort pulse laser emission**. London: IntechOpen, 2010. v. 1, p. 1-688.

73 CORREA, D. S.; BONI, L.; OTUKA, A. J. G.; TRIBUZI, V.; MENDONCA, C. R. Two-photon polymerization fabrication of doped microstructures. *In*: GOMES, A. S. **Polymerization**. London: IntechOpen, 2012. v. 1, p. 1-426.

74 DENK, W.; SVOBODA, K. Photon upmanship: why multiphoton imaging is more than a gimmick. **Neuron**, v. 18, n. 3, p. 351-357, 1997.

75 BOYD, R. W. **Nonlinear optics**. 3rd ed. Burlington: Academic Press, 2008.

76 PAWLICKI, M. *et al*. Two-photon absorption and the design of two-photon dyes. **Angewandte Chemie:** international edition, v. 48, n. 18, p. 3244-3266, 2009.

77 KAROTKI, A. *et al*. Enhancement of two-photon absorption in tetrapyrrolic compounds. **Journal of the Optical Society of America B:** optical physics, v. 20, n. 2, p. 321-332, 2003.

78 BHAWALKAR, J. D.; HE, G. S.; PRASAD, P. N. Nonlinear multiphoton processes in organic and polymeric materials. **Reports on Progress in Physics**, v. 59, n. 9, p. 1041-1070, 1996.

79 PARTHENOPOULOS, D. A.; RENTZEPIS, P. M. 3-dimensional optical storage memory. **Science**, v. 245, n. 4920, p. 843-845, 1989.

80 KAWATA, S.; KAWATA, Y. Three-dimensional optical data storage using photochromic materials. **Chemical Reviews**, v. 100, n. 5, p. 1777-1788, 2000.

81 FISHER, A. M. R.; MURPHREE, A. L.; GOMER, C. J. Clinical and preclinical photodynamic therapy. **Lasers in Surgery and Medicine**, v. 17, n. 1, p. 2-31, 1995.

82 SO, P. T. C. *et al*. Two-photon excitation fluorescence microscopy. **Annual Review of Biomedical Engineering**, v. 2, p. 399-429, 2000.

83 GU, M. Resolution in three-photon fluorescence scanning microscopy. **Optics Letters**, v. 21, n. 13, p. 988-990, 1996.

84 MARUO, S.; NAKAMURA, O.; KAWATA, S. Three-dimensional microfabrication with two-photon-absorbed photopolymerization. **Optics Letters**, v. 22, n. 2, p. 132-134, 1997.

85 MARUO, S.; KAWATA, S. Two-photon-absorbed near-infrared photopolymerization for three-dimensional microfabrication. **Journal of Microelectromechanical Systems**, v. 7, n. 4, p. 411-415, 1998.

86 BAGHERI, A.; JIN, J. Y. Photopolymerization in 3D printing. **ACS Applied Polymer Materials**, v. 1, n. 4, p. 593-611, 2019.

87 GOMES, V. T. R. P. **Fabricação de microestruturas poliméricas opticamente ativas integradas com nanofibras de vidro**. 2013. 108p. Tese (Doutorado em Ciências) - Instituto de Física de São Carlos, Universidade de São Paulo, São Carlos, 2013.

88 JUODKAZIS, S. *et al*. Two-photon lithography of nanorods in SU-8 photoresist. **Nanotechnology**, v. 16, n. 6, p. 846-849, 2005.

89 FLORY, P. J. **Principles of polymer chemistry**. Ithaca: Cornell University Press, 1990.

90 FACTS AND FIGURES ON PHOTONIC PROFESSIONAL GT2. Nanoscribe. Available from: https://www.nanoscribe.com/en/solutions/photonic-professional-gt2#tab-385 Accessible at: 19 Feb. 2020

91 EMONS, M. *et al*. Two-photon polymerization technique with sub-50 nm resolution by sub-10 fs laser pulses. **Optical Materials Express**, v. 2, n. 7, p. 942-947, 2012.

92 HASKE, W. *et al*. 65 nm feature sizes using visible wavelength 3-D multiphoton lithography. **Optics Express**, v. 15, n. 6, p. 3426-3436, 2007.

93 TAN, D. F. *et al*. Reduction in feature size of two-photon polymerization using SCR500. **Applied Physics Letters**, v. 90, n. 7, p. 071106, 2007.

94 FARSARI, M.; CHICHKOV, B. N. Two-photon fabrication. **Nature Photonics**, v. 3, n. 8, p. 450-452, 2009.

95 GUO, R. *et al*. Micro lens fabrication by means of femtosecond two photon photopolymerization. **Optics Express**, v. 14, n. 2, p. 810-816, 2006.

96 SEET, K. K. *et al*. Three-dimensional spiral-architecture photonic crystals obtained by direct laser writing. **Advanced Materials**, v. 17, n. 5, p. 541-545, 2005.

97 MENDONCA, C. R. *et al*. Reversible birefringence in microstructures fabricated by two-photon absorption polymerization. **Journal of Applied Physics**, v. 102, n. 1, p. 013109, 2007.

98 GITTARD, S. D. *et al*. Two photon polymerization: micromolding of polyethylene glycol-gentamicin sulfate microneedles. **Advanced Engineering Materials**, v. 12, n. 4, p. B77-B82, 2010.

99 MARUO, S.; IKUTA, K.; KOROGI, H. Force-controllable, optically driven micromachines fabricated by single-step two-photon micro stereolithography. **Journal of Microelectromechanical Systems**, v. 12, n. 5, p. 533-539, 2003.

100 OSTENDORF, A.; CHICHKOV, B. N. Two-photon polymerization: a new approach to micromachining. **Photonics Spectra**, v. 40, n. 10, p. 72-78, 2006.

101 SPENCE, D. E.; KEAN, P. N.; SIBBETT, W. 60-fsec pulse generation from a self-mode-locked Ti-Sapphire laser. **Optics Letters**, v. 16, n. 1, p. 42-44, 1991.

102 SIQUEIRA, J. D. P. **Implementação da técnica de varredura-Z com luz branca supercontínua gerada em fibras fotônicas na determinação do espectro**

de não linearidades. 2008. 121 p. Dissertação (Mestrado em Ciências) - Instituto de Física de São Carlos, Universidade de São Paulo, São Carlos, 2008.

103 SARUKURA, N.; ISHIDA, Y.; NAKANO, H. Generation of 50-fsec pulses from a pulse-compressed, cw, passively mode-locked Ti-Sapphire laser. **Optics Letters**, v. 16, n. 3, p. 153-155, 1991.

104 CRUZ, C. H. B.; FRAGNITO, H. L. **Fenômenos ultrarápidos:** geração de pulsos laser ultracurtos e suas aplicações. UNICAMP: Instituto de Física, 2000.

105 ZÍLIO, S. C. **Desenho e fabricação óptica**. São Carlos: Instituto de Física de São Carlos, 2006.

106 FOWLES, G. R. **Introduction to modern optics**. New York: Dover publications, 1989.

107 ZÍLIO, S. C. **Óptica moderna**. São Carlos: Instituto de Física de São Carlos, 2009.

108 BALDACCHINI, T. *et al*. Acrylic-based resin with favorable properties for three-dimensional two-photon polymerization. **Journal of Applied Physics**, v. 95, n. 11, p. 6072-6076, 2004.

109 JOCKUSCH, S. et al. A steady-state and picosecond pump-probe investigation of the photophysics of an acyl and a bis(acyl)phosphine oxide. **Journal of the American Chemical Society**, v. 119, n. 47, p. 11495-11501, 1997.

110 MENDONCA, C. R. *et al*. Two-photon absorption spectrum of the photoinitiator Lucirin TPO-L. **Applied Physics A:** materials science & processing, v. 90, n. 4, p. 633-636, 2008.

111 SIEGMAN, A. E. **Lasers**. Sausalito: University Science Book, 1986.

112 LIU, Z.-P. *et al*. Direct laser writing of whispering gallery microcavities by two-photon polymerization. **Applied Physics Letters**, v. 97, n. 21, p. 211105, 2010.

113 TAKADA, K.; SUN, H. B.; KAWATA, S. Improved spatial resolution and surface roughness in photopolymerization-based laser nanowriting. **Applied Physics Letters**, v. 86, n. 7, p. 071122, 2005.

114 CONSOLI, P. M. *et al*. Feature size reduction in two-photon polymerization by optimizing resin composition. **Journal of Polymer Science Part B:** polymer physics, v. 56, n. 16, p. 1158-1163, 2018.

115 TONG, L. M.; LOU, J. Y.; MAZUR, E. Single-mode guiding properties of subwavelength-diameter silica and silicon wire waveguides. **Optics Express**, v. 12, n. 6, p. 1025-1035, 2004.

116 BILODEAU, F. *et al*. Low-loss highly overcoupled fused couplers: fabrication and sensitivity to external-pressure. **Journal of Lightwave Technology**, v. 6, n. 10, p. 1476-1482, 1988.

117 CARMON, T.; YANG, L.; VAHALA, K. J. Dynamical thermal behavior and thermal self-stability of microcavities. **Optics Express**, v. 12, n. 20, p. 4742-4750, 2004.

118 MIAO, Y. D. *et al*. Dynamic Fano resonance in thin fiber taper coupled cylindrical microcavity. **IEEE Photonics Journal**, v. 8, n. 6, p. 4502806, 2016.

119 ALMEIDA, V. R.; LIPSON, M. Optical bistability on a silicon chip. **Optics Letters**, v. 29, n. 20, p. 2387-2389, 2004.

120 FANO, U. Effects of configuration interaction on intensities and phase shifts. **Physical Review**, v. 124, n. 6, p. 1866-1878, 1961.

121 STANCIK, A. L.; BRAUNS, E. B. A simple asymmetric lineshape for fitting infrared absorption spectra. **Vibrational Spectroscopy**, v. 47, n. 1, p. 66-69, 2008.

122 BONACCORSO, F. *et al*. Graphene photonics and optoelectronics. **Nature Photonics**, v. 4, n. 9, p. 611-622, 2010.

123 RATTANA, T. *et al*. Preparation and characterization of graphene oxide nanosheets. **Procedia Engineering**, v. 32, p. 759-764, 2012.

124 ZHENG, X. R. *et al*. In situ third-order nonlinear responses during laser reduction of graphene oxide thin films towards on-chip nonlinear photonic devices. **Advanced Materials**, v. 26, n. 17, p. 2699-2703, 2014.

125 JIANG, X. F. *et al*. Graphene oxides as tunable broadband nonlinear optical materials for femtosecond laser pulses. **Journal of Physical Chemistry Letters**, v. 3, n. 6, p. 785-790, 2012.

126 LOH, K. P. *et al*. Graphene oxide as a chemically tunable platform for optical applications. **Nature Chemistry**, v. 2, n. 12, p. 1015-1024, 2010.

127 STANKOVICH, S. *et al*. Graphene-based composite materials. **Nature**, v. 442, n. 7100, p. 282-286, 2006.

128 BAO, Q. L. *et al*. Graphene-polymer nanofiber membrane for ultrafast photonics. **Advanced Functional Materials**, v. 20, n. 5, p. 782-791, 2010.

129 LI, X. H. *et al*. Single-wall carbon nanotubes and graphene oxide-based saturable absorbers for low phase noise mode-locked fiber lasers. **Scientific Reports**, v. 6, n. 25266, 2016. DOI: 10.1038/srep25266.

130 WU, J. Y. *et al*. Graphene oxide waveguide and micro-ring resonator polarizers. **Laser & Photonics Reviews**, v. 13, n. 1900056, p. 1-11, 2019.

131 LI, X. P. *et al*. Giant refractive-index modulation by two-photon reduction of fluorescent graphene oxides for multimode optical recording. **Scientific Reports**, v. 3, n. 2819, p. 1-4, 2013.

132 PAN, S. Y.; AKSAY, I. A. Factors controlling the size of graphene oxide sheets produced via the graphite oxide route. **ACS Nano**, v. 5, n. 5, p. 4073-4083, 2011.

133 QI, X. D. *et al*. Size-specified graphene oxide sheets: Ultrasonication assisted preparation and characterization. **Journal of Materials Science**, v. 49, n. 4, p. 1785-1793, 2014.

134 GRAPHENE OXIDE. Sigma-Aldrich. Available from: https://www.sigmaaldrich.com/catalog/product/aldrich/796034?lang=pt&region=BR, Accessible at: 27 Jan. 2020.

135 SHARMA, B. *et al*. SERS: materials, applications, and the future. **Materials Today**, v. 15, n. 1-2, p. 16-25, 2012.

136 AN, J. H. *et al*. Surface-enhanced Raman scattering of dopamine on self-assembled gold nanoparticles. **Journal of Nanoscience and Nanotechnology**, v. 11, n. 5, p. 4424-4429, 2011.

137 MOHS, A. M. *et al*. Hand-held spectroscopic device for in vivo and intraoperative tumor detection: contrast enhancement, detection sensitivity, and tissue penetration. **Analytical Chemistry**, v. 82, n. 21, p. 9058-9065, 2010.

138 ZHU, Y. W. *et al*. Graphene and graphene oxide: synthesis, properties, and applications. **Advanced Materials**, v. 22, n. 35, p. 3906-3924, 2010.

139 EDA, G.; CHHOWALLA, M. Chemically derived graphene oxide: towards large-area thin-film electronics and optoelectronics. **Advanced Materials**, v. 22, n. 22, p. 2392-2415, 2010.

140 COLTHUP, N. B.; DALY, L. H.; WIBERLEY, S. E. **Introduction to infrared and Raman spectroscopy**. 3rd ed. Cambridge: Academic Press, 1990.

141 AVILA, O. I. *et al*. Femtosecond laser writing of PPV-doped three-dimensional polymeric microstructures. **Journal of Polymer Science Part B:** polymer physics, v. 56, n. 6, p. 479-483, 2018.

142 CORREA, D. S. *et al*. Two-photon polymerization for fabricating structures containing the biopolymer chitosan. **Journal of Nanoscience and Nanotechnology**, v. 9, n. 10, p. 5845-5849, 2009.

143 JIANG, L. J. *et al*. Two-photon polymerization: investigation of chemical and mechanical properties of resins using Raman microspectroscopy. **Optics Letters**, v. 39, n. 10, p. 3034-3037, 2014.

144 BALDACCHINI, T. *et al*. Characterization of microstructures fabricated by two-photon polymerization using coherent anti-stokes Raman scattering microscopy. **Journal of Physical Chemistry B**, v. 113, n. 38, p. 12663-12668, 2009.

145 GARMIRE, E. Resonant optical nonlinearities in semiconductors. **IEEE Journal of Selected Topics in Quantum Electronics**, v. 6, n. 6, p. 1094-1110, 2000.

146 SHEIKBAHAE, M. *et al*. Sensitive measurement of optical nonlinearities using a single beam. **IEEE Journal of Quantum Electronics**, v. 26, n. 4, p. 760-769, 1990.

147 ZHANG, F. *et al*. Dependence of the saturable absorption of graphene upon excitation photon energy. **Applied Physics Letters**, v. 106, n. 9, p. 091102, 2015.

148 KUMAR, S. *et al*. Femtosecond carrier dynamics and saturable absorption in graphene suspensions. **Applied Physics Letters**, v. 95, n. 19, p. 191911, 2009.

149 ZHAO, X. *et al*. Ultrafast carrier dynamics and saturable absorption of solution-processable few-layered graphene oxide. **Applied Physics Letters**, v. 98, n. 12, p. 121905, 2011.

150 LIU, Z. B. *et al*. Ultrafast dynamics and nonlinear optical responses from sp(2)- and sp(3)-hybridized domains in graphene oxide. **Journal of Physical Chemistry Letters**, v. 2, n. 16, p. 1972-1977, 2011.

151 SCHÄFER, F. P.; SCHMIDT, W.; MARTH, K. New dye lasers covering visible spectrum. **Physics Letters A**, v. 24, n. 5, p. 280-281, 1967.

152 SOROKIN, P. P. *et al*. Laser-pumped stimulated emission from organic dyes - experimental studies and analytical comparisons. **IBM Journal of Research and Development**, v. 11, n. 2, p. 130-148, 1967.

153 SOFFER, B. H.; MCFARLAND, B. B. Continuously tunable narrow-band organic dye lasers. **Applied Physics Letters**, v. 10, n. 10, p. 266-267, 1967.

154 SCHÄFER, F. P. **Dye lasers**. New York: Springer, 1990.

155 THIEL, E.; ZANDER, C.; DREXHAGE, K. H. Continuous wave dye-laser pumped by a hene laser. **Optics Communications**, v. 60, n. 6, p. 396-398, 1986.

156 SAMUEL, I. D. W.; TURNBULL, G. A. Polymer lasers: recent advances. **Materials Today**, v. 7, n. 9, p. 28-35, 2004.

157 TESSLER, N.; DENTON, G. J.; FRIEND, R. H. Lasing from conjugated-polymer microcavities. **Nature**, v. 382, n. 6593, p. 695-697, 1996.

158 OKI, Y. *et al*. Multiwavelength distributed-feedback dye laser array and its application to spectroscopy. **Optics Letters**, v. 27, n. 14, p. 1220-1222, 2002.

159 GROSSMANN, T. *et al*. Low-threshold conical microcavity dye lasers. **Applied Physics Letters**, v. 97, n. 6, p. 063304, 2010.

160 ÖZDEMIR, S. K. *et al*. Estimation of Purcell factor from mode-splitting spectra in an optical microcavity. **Physics Review A**, v. 83, n. 3, p. 033817, 2011.

161 BULOVIC, V. *et al*. Transform-limited, narrow-linewidth lasing action in organic semiconductor microcavities. **Science**, v. 279, n. 5350, p. 553-555, 1998.

162 VASSILIEV, V. V. *et al*. Narrow-line-width diode laser with a high-Q microsphere resonator. **Optics Communications**, v. 158, n. 1-6, p. 305-312, 1998.

163 SPIEGELBERG, C. *et al*. Low-noise narrow-linewidth fiber laser at 1550 nm. **Journal of Lightwave Technology**, v. 22, n. 1, p. 57-62, 2004.

164 TULEK, A.; AKBULUT, D.; BAYINDIR, M. Ultralow threshold laser action from toroidal polymer microcavity. **Applied Physics Letters**, v. 94, n. 20, p. 203302, 2009.

165 PARSANASAB, G. M.; MOSHKANI, M.; GHARAVI, A. Femtosecond laser direct writing of single mode polymer micro ring laser with high stability and low pumping threshold. **Optics Express**, v. 23, n. 7, p. 8310-8316, 2015.

166 DAS, A. J. *et al*. Three-dimensional microlasers based on polymer fibers fabricated by electrospinning. **Applied Physics Letters**, v. 99, n. 26, p. 263303, 2011.

167 YARIV, E. *et al*. Efficiency and photostability of dye-doped solid-state lasers in different hosts. **Optical Materials**, v. 16, n. 1-2, p. 29-38, 2001.

168 GROSSMANN, T. **Whispering-gallery-mode lasing in polymeric microcavities**. 2012. 126p. Ph.D. Thesis (Doctor in Science) - Karlsruher Institut für Technologie (KIT), Karlsruhe, 2012.

169 BONDING ORBITALS IN ETHYLENE (ETHENE) SP2. ChemTube 3D.
Available from: https://www.chemtube3d.com/orbitalsethene/.
Accessible at: 18 Jan. 2020.

170 SVELTO, O. **Principles of lasers**. New York: Plenum Press, 2007.

171 MARONCELLI, M.; FLEMING, G. R. Comparison of time-resolved fluorescence stokes shift measurements to a molecular theory of solvation dynamics. **Journal of Chemical Physics**, v. 89, n. 2, p. 875-881, 1988.

172 VERDEYEN, J. T. **Laser electronics**. 3rd ed. New Jersey: Prentice-Hall, 1995.

173 MIN, B. *et al*. Ultralow threshold on-chip microcavity nanocrystal quantum dot lasers. **Applied Physics Letters**, v. 89, n. 19, p. 191124, 2006.

174 CASEY, K. G.; QUITEVIS, E. L. Effect of solvent polarity on nonradiative processes in xanthene dyes: Rhodamine-B in normal alcohols. **Journal of Physical Chemistry**, v. 92, n. 23, p. 6590-6594, 1988.

175 GROSSMANN, T. *et al*. Strongly confined, low-threshold laser modes in organic semiconductor microgoblets. **Optics Express**, v. 19, n. 10, p. 10009-10016, 2011.

176 KUBIN, R. F.; FLETCHER, A. N. Fluorescence quantum yields of some rhodamine dyes. **Journal of Luminescence**, v. 27, n. 4, p. 455-462, 1982.

177 SNARE, M. J. *et al*. The photophysics of rhodamine-B. **Journal of Photochemistry**, v. 18, n. 4, p. 335-346, 1982.

178 WIERSMA, D. S. The physics and applications of Random lasers. **Nature Physics**, v. 4, n. 5, p. 359-367, 2008.

179 SZNITKO, L.; MYSLIWIEC, J.; MINIEWICZ, A. The role of polymers in random lasing. **Journal of Polymer Science Part B:** polymer physics, v. 53, n. 14, p. 951-974, 2015.

ANNEX A – List of publications and conference presentations

Part of this thesis was published in the following papers:

1. **Nathália B. Tomazio**, Adriano J. G. Otuka, Gustavo F. B. Almeida, Xavier Roselló-Mechó, Miguel V. Andrés, Cleber R. Mendonca. Femtosecond laser fabrication of high-Q whispering gallery mode microresonators via two-photon polymerization. Journal of Polymer Science, Part B: Polymer Physics, v. 55, n. 7, p. 569-574, 2017.

2. **Nathália B. Tomazio**, Leonardo De Boni, Cleber R. Mendonca. Low threshold Rhodamine doped whispering gallery mode microlasers fabricated by direct laser writing. Scientific Reports, v. 7, n. 8559, p. 1-5, 2017.

3. **Nathália B. Tomazio**, Franciele R. Henrique, Kelly T. de Paula, Ruben D. Fonseca, Cleber R. Mendonca. Saturable absorption in graphene oxide-doped acrylate polymer used for direct laser writing. 2019 SBFoton International Optics and Photonics Conference (SBFoton IOPC), p. 1-4, 2019.

Submitted paper:

1. **Nathália B. Tomazio**, Kelly T. Paula, Franciele R. Henrique, Marcelo B. Andrade, Xavier Roselló-Mechó, Martina Delgado-Pinar, Miguel V. Andrés, Cleber R. Mendonca. Mode cleaning in graphene oxide-doped polymeric whispering gallery mode microresonators. Submitted to Journal of Materials Chemistry C.

Complementary publications related to the PhD research:

1. **Nathália B. Tomazio**, Lucas F. Sciuti, Gustavo F. B. Almeida, Leonardo De Boni, Cleber R. Mendonca. Solid-state random microlasers fabricated via femtosecond laser writing. Scientific Reports, v. 8, p. 13561, 2018.

2. Oriana I. Avila, **Nathália B. Tomazio**, Adriano J. G. Otuka, Josiani C. Stefanelo, Marcelo B. Andrade, Debora T. Balogh, Cleber R. Mendonca. Femtosecond laser writing of PPV-doped three-dimensional polymeric microstructures. Journal of Polymer Science, Part B: Polymer Physics, v. 56, p. 479-483, 2018. (This work was selected to appear on the journal's cover)

3. **Nathália B. Tomazio**, André L. S. Romero, Cleber R. Mendonca. The development of an optical shutter from a computer hard disk. Revista Brasileira de Ensino de Física, v. 40, n. 1, e1307(5), 2017.

4. Rafaela C. Sanfelice, Luiza A. Mercante, Adriana Pavinatto, **Nathália B. Tomazio**, Cleber R. Mendonca, Sidney J. L. Ribeiro, Luiz H. C. Mattoso, Daniel S. Correa. Hybrid composite material based on polythiophene derivative nanofibers modified with gold nanoparticles for optoelectronics applications. Journal of Materials Science, v. 52, n. 4, p. 1919-1929, 2017.

5. Sabrina N. C. Santos, Juliana M. P. Almeida, Kelly Tasso, **Nathália B. Tomazio**, Valmor R. Mastelaro, Cleber R. Mendonca. Characterization of the third-order optical nonlinearity spectrum of barium borate glasses. Optical Materials, v. 73, p. 16-19, 2017.

6. Franciele R. Henrique, **Nathália B. Tomazio**, Ramon G. T. Rosa, Adélcio M. Souza, Camila P. D'Almeida, Lucas F. Sciuti, Marlon R. Garcia, Leonardo De Boni. Light at first sight: A program of activities to teach Optics using colors. Revista Brasileira de Ensino de Física, v. 41, n. 3, e20180223 (7), 2019.

7. Idelma A. A. Terra, Rafaela C. Sanfelice, Vanessa P. Scagion, **Nathália B. Tomazio**, Cleber R. Mendonca, Luiz A. O. Nunes, Daniel S. Correa. Polyvinylpyrrolidone electrospun nanofibers doped with Eu 3+: fabrication, characterization, and application in gas sensors. Journal of Applied Polymer Science, v. 136, p. 47775, 2019.

8. Lucas F. Sciuti, Tássia S. Gonçalves, **Nathália B. Tomazio**, Andréa S. S. de Camargo, Cleber R. Mendonca, Leonardo de Boni. Random laser action in

dye-doped xerogel with inhomogeneous TiO2 nanoparticles distribution. Journal of Materials Science: Materials in Electronics, v. 30, p. 16747-16754, 2019.

Selected presentations at international conferences:

1. **Nathália B. Tomazio**, Kelly T. Paula, Franciele R. Henrique, Ruben D. Fonseca, Miguel V. Andrés, Cleber R. Mendonca. Mode suppression in graphene oxide-doped microcavities fabricated by two-photon polymerization. At Photonics West – Optical Components and Materials XVII, 2020, San Francisco, United States. (oral)

2. **Nathália B. Tomazio**, Franciele R. Henrique, Kelly T. Paula, Ruben D. Fonseca, Cleber R. Mendonca. Saturable absorption in graphene oxide-doped acrylate polymer used for direct laser writing. At SBFoton International Optics and Photonics Conference, 2019, *São Paulo*, Brazil. (oral)

3. **Nathália B. Tomazio**, Lucas F. Sciuti, Gustavo F. B. Almeida, Leonardo De Boni, Cleber R. Mendonca. Dye-doped random microlasers fabricated via femtosecond laser induced two-photon polymerization. At Photonics West – Organic Photonic Materials and Devices XXI, 2019, San Francisco, United States. (oral)

4. **Nathália B. Tomazio**, Leonardo De Boni, Cleber R. Mendonca. Low threshold dye whispering gallery mode microlasers fabricated by two-photon polymerization. At Photonics West - Laser Resonators, Microresonators and Beam Control XX, 2018, San Francisco, United States. (oral)

5. **Nathália B. Tomazio**, Leonardo De Boni, Cleber R. Mendonca. Low threshold Rhodamine doped microlasers fabricated by direct laser writing. At 2017 Siegman International School on Lasers, 2017, Leon, Mexico. (poster)

6. **Nathália B. Tomazio**, Leonardo De Boni, Cleber R. Mendonca. Low-threshold Rhodamine B doped microlasers fabricated via two-photon polymerization. At 2017 Frontiers in Optics/Laser Science Conference, 2017, Washington D.C., United States. (oral)

7. **Nathália B. Tomazio**, Leonardo De Boni, Cleber R. Mendonca. Low-threshold dye microlasers fabricated via femtosecond laser induced two-photon polymerization. At 10th International Conference on Nanophotonics, 2017, *Recife*, Brazil. (poster)

8. **Nathália B. Tomazio**, Xavier Roselló-Mechó, Adriano J. G. Otuka, Gustavo F. B. Almeida, Antonio Díez, Miguel V. Andrés, Cleber R. Mendonca. Femtosecond laser-induced two-photon polymerization of whispering gallery mode microresonators. At Photonics West - Laser Resonators, Microresonators and Beam Control XVIII, 2016, San Francisco, United States. (poster)

9. **Nathália B. Tomazio**, Xavier Roselló-Mechó, Adriano J. G. Otuka, Gustavo F. B. Almeida, Antonio Díez, Miguel V. Andrés, Cleber R. Mendonca. Femtosecond laser fabrication of polymeric optical resonators. At Latin American Optics & Photonics Conference (LAOP), 2016, *Medellín*, Colombia. (oral)

10. **Nathália B. Tomazio**, Cleber R. Mendonça. Femtosecond laser fabrication of whispering gallery mode microresonators. At *São Paulo* School of Advanced Science on Nanophotonics and XV Jorge Andre Swieca School on Nonlinear and Quantum Optics, 2016, *Campinas*, Brazil. (poster)

ANNEX B – Ph.D. exchange program at Columbia University, United States

2018 – 2019

(6 months) Project title: Inverse design of polymeric nanophotonic devices
Supervisor: Prof. Dr. Michal Lipson
Supported by: *Coordenação de Aperfeiçoamento de Pessoal de Nível Superior* (*CAPES*)

Summary:

Inverse design algorithms are optimization tools developed to automate the design of nanophotonic devices. They have proven to bring high-performance, robust and broadband devices into compact footprints. Although many materials are important for nanophotonics, the progress on inverse design devices has been made mostly in silicon. In this project, we aimed to investigate the use of an inverse design algorithm to automate the design of arbitrary nanophotonic devices made of polymer. The software package used in this project relies on gradient-based (adjoint) photonic optimization. It was developed at Prof. Vuckovic's Nanoscale and Quantum Photonics Lab at Stanford University.

The motivation to expand the use of inverse design to polymer devices is twofold:

(ii) To leverage 3D fabrication capabilities to produce devices able to connect photonic waveguides of different heights, which can be challenging to achieve with conventional lithography techniques. For example, the combined use of inverse design and 3D nanofabrication can enable the development of couplers that convert waveguide modes on a chip to higher-order modes in a multimode fiber, leading to an increase in the data transfer capacity of multiplexing systems.

(iii) To use the polymer structure as a cast for the fabrication of 3D devices made of other materials, e.g., Si_3N_4.

The main challenge of this project is to process the continuously varying-refractive index map resulting from optimization to meet fabrication requirements. For this purpose, our main strategy consisted of making use of effective medium theory to translate the refractive index map into a density distribution of polymer pillars over

the photonic structure. Though this is an ongoing work, our finite-difference time domain simulations of an optimized mode coupler show that a small footprint device with performance (degree of mode convertion) higher than 95% could be reached by playing with the discretization of the refractive index interval. Overall, by bringing the index map into the reach of 3D nanofabrication, this project will not only benefit inverse design, but any design approach that results in an refractive index map, such as transformation optics.

ANNEX C – Ph.D. exchange program at *Universitat of València*, Spain

2018

(1 month) The goal of this project was to study (i) the influence of graphene oxide on the modal behavior of GO-doped polymeric WGM microresonators and (ii) the thermo-optic dynamics in pure and GO-doped polymeric WGM microresonators.

Supervisor: Prof. Dr. Miguel V. Andrés

Supported by: European Union/project iPhoto-Bio IRSES

Summary:

The first part of this project, which aimed at studying the influence of graphene oxide on the modal behavior of GO-doped polymeric microresonators, is described in Chapter 5 and the second part will be presented here.

For most applications of WGM microresonators, a frequency-stable operation in the presence of thermal instability is of great importance. For example, the thermal drift of WGMs caused by environmental perturbation and probe-induced noise degrades the strength of nonlinear phenomena in the microresonators considerably by inducing linewidth broadening and distortion to the resonances. In particular, polymers have relatively high thermo-optic coefficients, which combined with the high circulating optical intensities achieved in the WGMs, makes polymeric WGM microresonators prone to thermal instabilities. Therefore, to enable further advancement of the polymeric WGM microresonator presented herein for applications in nonlinear optics, we investigated the thermo-optic dynamics of its resonances upon optical pump-induced heating.

The setup assembled for studying thermo-optic responses in these microresonators used a near-infrared tunable laser operating in the coarse tuning mode as the light source. The laser tuning was controlled by a function generator combined with a DC source to adjust the scan speed, direction, wavelength range. The transmission spectrum of the microresonator coupled to a 2 μm-waist taper is measured using an InGaAs photodiode connected to an oscilloscope.

So far, we have been able to measure a few thermo-induced phenomena, such as hysteretic wavelength response and thermal linewidth broadening, for the

undoped and GO-doped microresonators, and to determine the signal of the thermo-optic coefficient of the microresonator's material (acrylate polymer) by varying the input power and both the scan speed and direction, either towards longer wavelengths (forward scan) or otherwise (backward scan). However, further characterization of the thermo-optic dynamics would be necessary to determine self-stable solutions for the pump-resonance detuning that allow the microresonator system to automatically correct for power- and wavelength-fluctuations of the pump and to remain loaded for longer.